Performance Analysis of a 3-phase Induction Machine with Inclined Static Eccentricity

by

Xiaodong Li
B.Eng., Shanghai Jiao Tong University, 1994

A Thesis Submitted in Partial Fulfillment of the Requirements for the Degree of

MASTER OF APPLIED SCIENCE

in the Department of Electrical and Computer Engineering

We accept this thesis as conforming to the required standard

Supervisor: Dr. Subhasis Nandi

ABSTRACT

Fault diagnosis is gaining more attention for electric machines running critical loads, whose sudden breakdown can result in unpredictable revenue losses. Consequently the motor drive systems with fault diagnostic and prediction features are of great concern and are becoming almost indispensable. Among all kinds of common faults, quite a few have relationship with unequal air-gap. So far, work on detection of eccentricity related faults in synchronous and induction machines have been well documented.

However, few are reported on faults resulting from axial non-uniform air-gap. This thesis investigates the performance of a three-phase induction machine with non-uniform static eccentricity along axial direction or inclined static eccentricity. A variant of Modified Winding Function Approach (MWFA) is applied to study this fault. The relationship between the number of rotor bars, poles and the existence of fault related current harmonics is discussed. It is shown that inclined eccentricity also demonstrates similar characteristics as circumferential non-uniform air-gap (Static Eccentricity or Dynamic Eccentricity). The case that demands special attention is inclined eccentricity symmetric to the mid-point of machine shaft, which cannot be detected directly from current spectrum. These results will be useful reference to the designers of online tools for machine condition monitoring. Finite Element results to verify the inductance values used in simulation are also presented. The analysis is supplemented by the stator current spectra obtained from simulated results for different load and fault conditions. Finally a four-pole, 45 rotor bar, 2 kW induction motor is used to validate the theoretical and simulation results experimentally.

Examiners:

Table of Contents

Title.....i

Abstract.....ii

Table of Contents.....iii

List of Tables.....v

List of Figures.....vi

List of Abbreviations.....x

List of Symbols.....xi

Acknowledgements.....xiii

Chapter 1 Review of Diagnosis of Eccentricity-related Faults.....1
1.1 Introduction of Fault Diagnosis of Electrical Machines.....1
1.2 Eccentricity-related Faults.....3
1.3 Detection of Eccentricity-related Faults.....5
1.4 Motivations and Thesis Outline.....8

Chapter 2 Principle of Motor Current Signature Analysis to Detect Static Eccentricity.....10
2.1 Introduction.....10
2.2 Mechanism of the Generation of Eccentricity Related Harmonics and Principal Slot Harmonic in Line Current.....10
2.2.1 Healthy Condition.....11
2.2.2 Static Eccentricity.....15
2.3 Conclusions.....19

Chapter 3 MWFA and Calculation of the Inductances in AC machines.....20
3.1 Introduction.....20
3.2 A Variant of MWFA and Inductance Calculations in 3-D Space.....20
3.3 Air gap Length in Inclined Static Eccentricity.....26
3.4 Conclusions.....28

Chapter4 Coupled Magnetic Circuit Based State Space Model of Induction Motor.....29
4.1 Introduction.....29
4.2 Induction Machine Model.....29
4.3 Conclusions.....33

Chapter 5 Simulation of a 3-phase Induction Motor with Inclined Static Eccentricity.....34
5.1 Introduction.....34
5.2 Simulation Results of Motor Inductances.....34
5.3 Simulation Results for Detection of Inclined Eccentricity.....42
5.4 Conclusions.....48

Chapter 6 Evaluation of Motor Inductances with Finite Element Method.....49
6.1 Introduction.....49
6.2 Simulation Results of Finite Element Method.....49
6.3 Conclusions.....55

Chapter 7 Experimental Results of an Induction Motor with Inclined Eccentricity.....56
7.1 Introduction.....56
7.2 Experiment Method and Results.....57
7.3 Conclusions.....66

Chapter 8 Conclusions and Future Work.....67
8.1 Conclusions.....67
8.2 Future Work.....68

Bibliography.....69

Appendix A Motor Data for Inclined Eccentricity Simulation and Experiment.....74

Appendix B Additional Simulation Results of Motor Inductances.....75

Appendix C Additional Simulation Results of Detection of Inclined Static Eccentricity.....79

Appendix D Additional Experimental Results of Detection of Inclined Static Eccentricity.....91

List of Tables

Table 5.1 Simulated, normalized amplitude of fault related harmonics under different faulty situations and load levels. (The fundamental (at 60 Hz) amplitude for all cases is 0 dB).....43

Table 6.1 Comparison of stator magnetizing inductance, mutual inductance obtained from MWFA and Finite Element.....50

Table 7.1 Experimental, normalized amplitude of eccentricity related harmonics under different faulty situations and load levels. (The fundamental (at 60 Hz) amplitude for all cases is 0 dB).....60

Table 7.2 Experimental, normalized amplitude of unbalanced supply related harmonics under different faulty situations and load levels. (The fundamental (at 60 Hz) amplitude for all cases is 0 dB).....60

List of Figures

Figure 1.1 Circumferential unequal air-gap, C1 is the center of stator, C2 is the center of rotor. 4

Figure 1.2 Axial or inclined unequal air-gap....4

Figure 2.1 Simulated, normalized line current spectra of healthy machines. From (a) to (d) R= 28, 42, 43, 44. PSH is principal slot harmonics, the amplitude of the fundamental is 0 dB....14

Figure 2.2 Simulated, normalized line current spectra of machines with uniform 25% SE. From (a) to (d) R= 28, 42, 43, 44. PSH is principal slot harmonics, the amplitude of the fundamental is 0 dB....17

Figure 3.1 The cross section of an elementary doubly cylindrical machine....21

Figure 5.1 Stator winding distribution of phase A (×: current going perpendicularly inside the plane of paper, •: current going perpendicularly outside the plane of paper). Slot numbers 1, 10, 19, 28 are shown for easy identification of slots....35

Figure 5.2 Turns functions $n(\varphi)$ and winding functions $N(\varphi)$ of (a) stator phase a and (b) rotor loop 1....36

Figure 5.3 Mutual inductance L_{sra1} (top) and its derivative (bottom) with respect to rotor position between stator phase a and rotor loop 1 without rotor eccentricity....38

Figure 5.4 Mutual inductances and their derivatives under uniform 50% SE, (a) L_{sra1}, between phase a and loop 1; (b) $dL_{sra1}/d\theta_r$; (c) L_{rr11}, between rotor loop 1 and loop 1; (d) $dL_{rr11}/d\theta_r$....38

Figure 5.5 Variation of mutual inductances and their derivatives under inclined static eccentricity (one end 50% SE, the other end –50% SE), (a) L_{sra1}, between phase a and loop 1; (b) $dL_{sra1}/d\theta_r$; (c) L_{rr11}, between rotor loop 1 and loop 1; (d) $dL_{rr11}/d\theta_r$....40

Figure 5.6 Simulation results under uniform air-gap (a) start-up characteristics, full load applied at 3 s; (b) normalized stator current spectrum with full load....44

Figure 5.7 Simulation results under uniform 25% SE (a) start-up characteristics, full load applied at 3 s; (b) normalized stator current spectrum with full load....45

Figure 5.8 Simulated, normalized stator current spectrum with uniform 50% SE under full load.....46

Figure 5.9 Simulated, normalized stator current spectrum with inclined rotor (one end 40% SE, the other end 60% SE) under full load.....46

Figure 5.10 Simulated, normalized stator current spectrum with inclined rotor (one end 0% SE, the other end 50% SE) under full load.....47

Figure 5.11 Simulated, normalized stator current spectrum with inclined rotor (one end 50% SE, the other end –50% SE) under full load.....47

Figure 6.1 Comparison of mutual inductances obtained by MWFA (left) and Finite Element (right), from top to bottom are mutual inductances between rotor loop 1 and stator phase *a*, *b*, *c* respectively, (a) healthy machine; (b) under uniform 50% SE.....51

Figure 6.2 Comparison of rotor loops self and mutual inductances obtained by MWFA (left) and Finite Element (right), from top to bottom are self-inductance of rotor loop 1, mutual inductance between rotor loop 1 and 24 under uniform 50% SE.....53

Figure 6.3 Variation of mutual inductance L_{sra1} between stator phase *a* and rotor loop 1 obtained from MWFA (left) and Finite Element method (right) for one end 50% SE, the other end –50% SE.....53

Figure 6.4 Flux distribution of the experimental motor with one stator phase excited for (a) healthy condition and (b) uniform 50% SE condition.....54

Figure 7.1 Experimental setup.....56

Figure 7.2 The experimental induction machine (a) actual motor; (b) schematic diagram of motor; (c) end bell, the eccentric sleeve and bearing 57

Figure 7.3 Simulated, normalized line current spectrum with 10% unbalance in supply voltage under uniform 50% SE.....61

Figure 7.4 Experimental, normalized spectrum of line current for healthy case under full load.....61

Figure 7.5 Experimental, normalized spectrum of line current with inclined rotor (one end 50% SE, the other end -50% SE) under full load.....62

Figure 7.6 Experimental, normalized spectrum of line current with inclined rotor (one end 22.89% SE, the other end 32.53% SE) under full load.....62

Figure 7.7 Experimental, normalized spectrum of line current with uniform 50% SE under full load.....63

Figure 7.8 Experimental, normalized spectrum of line current with inclined rotor (one end 45.78% SE, the other end 65.06% SE) under full load.....63

Figure 7.9 Variation of the amplitude of eccentricity related components under different load levels. Left: experimental results; Right: simulated results. From top to bottom, the average eccentricity ratio are around 50%, 0, 25%.....64

Figure 7.10 Variation of the amplitude of eccentricity related harmonics with the average eccentricity severity under different load levels for experiment (left) and simulation (right). The test points are healthy, 22.89% & 32.53%, uniform 50%, 45.78% & 65.06%. From top to bottom, the load levels are: no-load, 25% load, 50% load, 75% load, full-load.....65

Figure B1 Mutual inductance L_{sra24} (top) and its derivative (bottom) under uniform 50% SE between stator phase *a* and rotor loop 24.....75

Figure B2 Mutual inductance $L_{rr1\text{-}24}$ (top) and its derivative (bottom) under uniform 50% SE between rotor loop 1 and loop 24.....76

Figure B3 Variation of mutual inductance L_{sra24} (top) and its derivative (bottom) under inclined static eccentricity (one end 50% SE, the other end -50% SE) between stator phase *a* and rotor loop 24.....77

Figure B4 Variation of mutual inductance $L_{rr1\text{-}24}$ (top) and its derivative (bottom) under inclined static eccentricity (one end 50% SE, the other end -50% SE) between rotor loop 1 and loop 24.....78

Figure C1 Simulated, normalized stator current spectra with uniform air-gap under (a) no load, (b) 25% load, (c) 50% load, (d) 75% load.....79

Figure C2 Simulated, normalized stator current spectra with uniform 25% SE under (a) no load, (b) 25% load, (c) 50% load, (d) 75% load.....81

Figure C3 Simulated, normalized stator current spectra with uniform 50% SE under (a) no load, (b) 25% load, (c) 50% load, (d) 75% load.....83

Figure C4 Simulated, normalized stator current spectra with inclined rotor (one end 40% SE, the other end 60% SE) under (a) no load, (b) 25% load, (c) 50% load, (d) 75% load.....85

Figure C5 Simulated, normalized stator current spectra with inclined rotor (one end 0% SE, the other end 50% SE) under (a) no load, (b) 25% load, (c) 50% load, (d) 75% load.....87

Figure C6 Simulated, normalized stator current spectra with inclined rotor (one end 50% SE, the other end -50% SE) under (a) no load, (b) 25% load, (c) 50% load, (d) 75% load.....89

Figure D1 Experimental, normalized spectra of line current for healthy case under (a) no load, (b) 25% load, (c) 50% load, (d) 75% load.....91

Figure D2 Experimental, normalized spectra of line current with inclined rotor (one end 50% SE, the other end –50% SE) under (a) no load, (b) 25% load, (c) 50% load, (d) 75% load.....93

Figure D3 Experimental, normalized spectra of line current with inclined rotor (one end 22.89% SE, the other end 32.53% SE) under (a) no load, (b) 25% load, (c) 50% load, (d) 75% load.....95

Figure D4 Experimental, normalized spectra of line current with uniform 50% SE under (a) no load, (b) 25% load, (c) 50% load, (d) 75% load.....97

Figure D5 Experimental, normalized spectra of line current with inclined rotor (one end 45.78% SE, the other end 65.06% SE) under (a) no load, (b) 25% load, (c) 50% load, (d) 75% load.....99

List of Abbreviations

AI	Artificial Intelligence
ANN	Artificial Neural Network
DE	Dynamic Eccentricity
EMF	Electromotive Force
FFT	Fast Fourier Transform
MCC	Motor Control Center
MCSA	Motor Current Signature Analysis
MMF	Magnetomotive Force
MWFA	Modified Winding Function Approach
PSD	Power Spectral Density
PSH	Principal Slot Harmonic
RF	Radio Frequency
SE	Static Eccentricity
TIR	Total Indicated Reading
TSCFE	Time-Stepping Coupled Finite-Element
UMP	Unbalanced Magnetic Pull
WFA	Winding Function Approach

List of Symbols

a, a_o	eccentricity ratio
A	peak of fundamental
B	magnetic flux density
C	constants
D	variables
f	frequency
F	magnetomotive force
g, g_o	air-gap length
H	magnetic flux intensity
i, I	current
J	current density
J_k	mechanical inertia
k	number
l	length
L_{AB}	inductance of coil A due to current flowing in coil B
N	the number of turns in series in stator per phase
m	number
n	number
p	the number of pole pairs
P	specific permeance
q	number
r	radius

R	the number of rotor slots/bars
R_s, R_r, r_b, r_e	resistances
s	slip
S	surface
t	time
T_e, T_L	torque
V	voltage
z	axis
$\alpha, \beta, \gamma, \delta, \theta, \varphi, \phi, x$	angles
ε	number
μ	permeability
ω, ω_r	rotating angular speed
Φ	flux
λ, Λ	flux linkage

Acknowledgements

I would like to thank my supervisor Dr. Subhasis Nandi, for his kind, valuable guidance in the last two years' research work and preparation of this thesis.

I would like to thank the members of my supervisory committee for their valuable time and advice.

I would like to thank Mr. Rodney Katz, in the department of Mechanical Engineering at University of Victoria who helped me build the laboratory components.

Finally, I would like to thank my dear parents and my wife, Bin, for their generous, selfless supports and affections.

Chapter 1

Review of Diagnosis of Eccentricity-related Faults

1.1 Introduction of Fault Diagnosis of Electrical Machines

As the dominant electromechanical energy conversion devices available currently, electrical machines are widely used as critical components of many industrial processes, from power generation to mining, chemical processing, subway systems and so on. In spite of their comparative robustness and reliability, their sudden failures during the normal course of operation can result in significant plant downtime, unpredictable revenue losses, or even cause damage to other equipments and personnel. For some machines running the critical loads, it is imperative that faults are diagnosed at an incipient stage, without stopping the process. Hence, there is a considerable demand for electrical machines and drive systems with fault diagnostic and prediction features, especially for ac induction motor—the most commonly used rotating electrical machine in modern industry.

The history of fault diagnosis and protection is as archaic as the machines themselves. The manufacturers and users of electrical machines initially relied on simple protections such as over-current, over-voltage, earth-fault, etc. to ensure safe and reliable operation. However, as the tasks performed by these machines grow increasingly complex, the modern industry is becoming more interested in adopting new condition monitoring techniques, on-line or off-line, to assess or evaluate the operating conditions of electrical machines. An ideal fault diagnosis technique, therefore, should have the following characteristics:

- Predict failures at their inception accurately.
- Indicate the possible reasons of the failure.
- Function without interrupting normal operation i.e. online monitoring.

Only a system with the aforementioned features can efficiently reduce unscheduled downtime or unnecessary emergency maintenance, and minimize consequent revenue

losses.

The major abnormalities of electrical machines can broadly be classified as the following [1]:

a) Inter-turn faults resulting in the opening or shorting of one or more of a stator phase winding.
b) Broken rotor bars or cracked rotor end-rings.
c) Static and /or dynamic air-gap irregularities.
d) Bent shaft (akin to dynamic eccentricity), which can result in a rub between the rotor and stator, causing serious damage to rotor, stator core and windings.
e) Shorted rotor field winding causing over heating, which may also result in bending of the rotor.
f) Bearing and gearbox failures.

Of the above types of faults i) bearing, ii) the stator or armature faults, iii) the broken rotor bar and end ring faults for induction machines and iv) the eccentricity related faults are the most prevalent ones and thus demand special attention. These faults produce one or more of the symptoms as given below:

a) Unbalanced air-gap, voltages and line currents.
b) Increased torque pulsations.
c) Decreased average torque.
d) Increased losses and reduction in efficiency.
e) Excessive heating.

For the purpose of detecting such fault-related signals many diagnostic methods have been developed so far. These methods to identify the above faults may involve several different types of fields of science and technology. They can be described as [1-3]:

a) Electromagnetic field monitoring with search coils, coils in stator slots or wound around motor shafts (axial flux related detection).
b) Temperature measurements of bearing, stator winding.
c) Infrared recognition.
d) Radio frequency (RF) emissions monitoring.
e) Noise and vibration monitoring of core, bearing.

f) Chemical analysis, such as bearing oil analysis, carbon monoxide gas analysis due to degradation of electric insulation for closed electric circuit air-cooled motors with water-cooled heat exchangers.

g) Acoustic noise measurements.

h) Motor current signature analysis (MCSA).

i) AI (artificial intelligence) based techniques.

1.2 Eccentricity-related Faults

Of all the common faults in induction motors, the eccentricity-related faults account for a significant portion. Machine eccentricity is the condition of unequal air-gap between stator and rotor. High level of eccentricity can result in unbalanced radial force, also known as Unbalanced Magnetic Pull (UMP), which brings up mechanical stress on some parts of the shaft and the bearing. After long time operation, these factors can snowball into broken mechanical parts or even stator to rotor rub causing the major breakdown of the machine [4].

Eccentricity condition can also be further divided into two categories: circumferential unequal air-gap (Fig. 1.1) and axial or inclined unequal air-gap (Fig. 1.2).

Circumferential unequal air-gap can be subdivided into: SE (static eccentricity) and DE (dynamic eccentricity) [4]. In case of SE, the center of stator and rotor are different and the rotor rotates around its own center. The position of the minimal radial air-gap length is fixed in space. For new machines, static eccentricity may be caused by the ovality of the stator core or by the incorrect positioning of the rotor or stator at the commissioning stage. If the rotor-shaft assembly is sufficiently stiff, the level of static eccentricity does not change even after long time operation. In case of DE, the rotor center doesn't coincide with the stator and the rotor rotates around the center of the stator. The position of minimum air-gap rotates with the rotor. Thus dynamic eccentricity is a function of both rotor position and time. Dynamic eccentricity in a new machine is controlled by the Total Indicated Reading (TIR) or "run-out" of the rotor [4].

Axial unequal air-gap occurs when the rotor's geometric axis is not parallel to that of the stator. Then along the axial direction the degree of eccentricity is changing [5, 6].

Thus axial or inclined eccentricity can also be treated as a variable circumferential eccentricity.

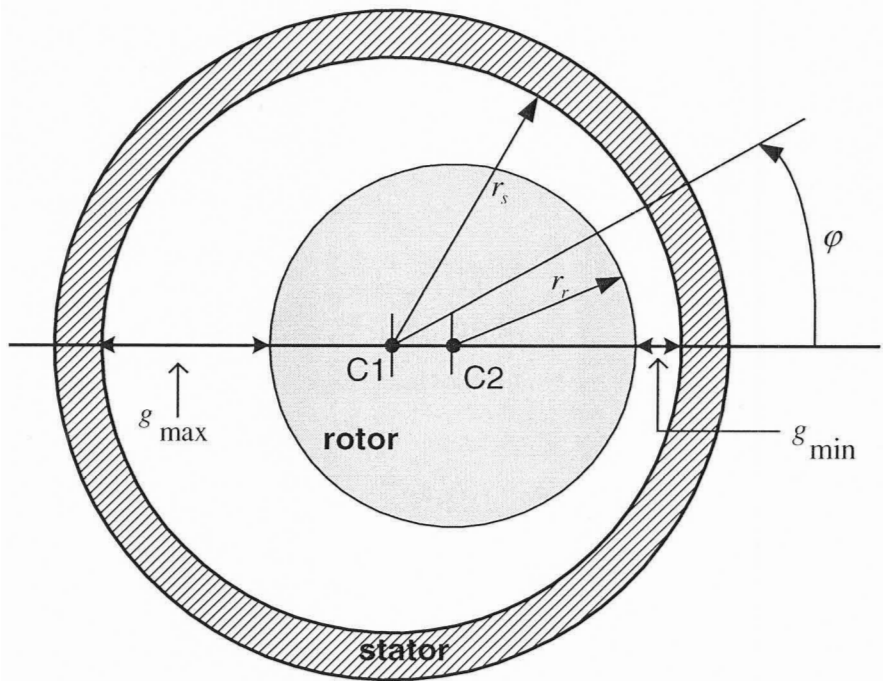

Figure 1.1 Circumferential unequal air-gap, C1 is the center of stator, C2 is the center of rotor

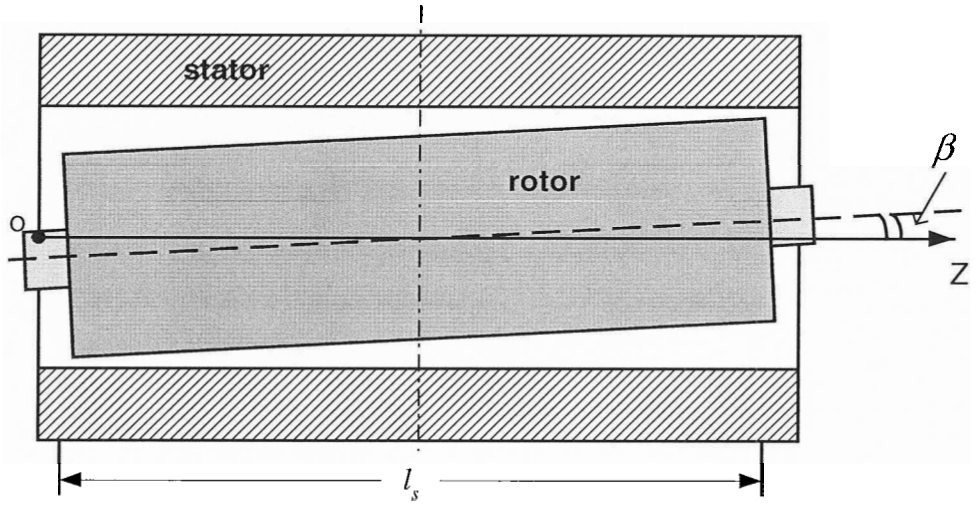

Figure 1.2 Axial or inclined unequal air-gap

In reality, both static and dynamic eccentricities tend to co-exist. An inherent level of static eccentricity exists even in newly manufactured machines due to the build-up of tolerance during manufacturing and assembly procedure, as has been reported by Dorrell [7]. This causes a steady UMP in one direction. With usage, this may lead to bent rotor

shaft, bearing wear and tear etc. This may also result in some degree of dynamic eccentricity. However, it can be kept to minimum by good design, stringent quality standard, followed by comprehensive test and high quality installation procedures. Normally a total air-gap eccentricity of up to 10% is permissible [8]. The reasons that lead to unequal air-gap after long time operation may involve many different factors. It can be caused by: (a) Unbalanced load; (b) Bearing wear; (c) Bent rotor shaft; (d) Mechanical resonance at critical load.

1.3 Detection of Eccentricity-related Faults

The research on eccentricity can be dated back to almost one century. There is an abundance of published literature on the subject. Different ways to model and monitor machines with rotor eccentricity have been developed. Most of classic papers concentrated on the calculation of all kinds of factors as the function of eccentricity and UMP. The factors that are related to air-gap eccentricity and UMP include air gap flux, the design of rotor assembly, critical speed, slot combination, winding, vibration, acoustic noise [9]. However, most of them are not suitable for online condition monitoring required by modern industry. The reasons range from lack of fault discrimination procedures to inconvenience of onsite installation and so on.

It has been shown long ago that the slot harmonics of acoustic noise spectra of motors could be used to indicate the existence of static eccentricity. However, the application of noise measurement is impractical for plants with high-level background noise or with many machines operating in close proximity [10].

The air gap flux spectrum analysis can identify the frequency components of induced EMF (electromotive force) due to eccentricity by means of search coils in the stator slots. However, it is neither practical nor economical to insert search coils in stator slots of machines that are already in service. Even for new motors the installation can be a problem, which needs the approval of design modification from the manufacturers, operators, safety legislating authority [11]. Another option is a search coil around the shaft that can sense the axial flux components resulting from eccentricity [12]. To obtain a reliable signal, there are

strict requirements on the installation position and the design of the motor and its enclosure, which are often extremely difficult to meet.

Although the amplitude of some components in bearing vibration spectrum can increase with an increase of air-gap eccentricity, these vibration components are not unique to eccentricity problem. For example, the vibration components at rotating frequency may change due to air gap eccentricity, mechanical imbalance in the rotor or because of problems in mechanical load [8].

Stator core vibration has also been recommended as the monitored parameter to detect eccentricity [8, 11]. The vibration components due to rotor slot effect will increase in magnitude in case of static eccentricity, and dynamic eccentricity will bring up other unique components in vibration spectrum. However, the severity of eccentricity is hard to predict due to the complexity of modeling electromagnetic force and the mechanical response of stator core. Also this application has the problem of installing vibration transducer, similar to that mentioned before concerning the air gap flux search coils. Hence, stator core or frame vibration analysis has not been widely used by industries [8].

Currently, MCSA (Motor Current Signature Analysis) is the most popular fault detection method in industries. The first reason is that almost all of motor abnormalities can directly or indirectly affect line current and generate some frequency components. Secondly, the line current signal is easier to obtain by means of a clip-on current transformer in remote MCC (Motor Control Center) without any disturbance to the operating motors— hence called "non-invasive detection".

By using MMF (Magnetic-Motive Force) and permeance approach, Carmeron *et al* [9] have shown that the flux density distribution can be calculated as the product of MMF and air gap permeance, which include the effects of stator and rotor slotting, saturation and eccentricity. Therefore, the flux density is expected to include some characteristic harmonics related to eccentricity. Since the flux is moving relative to the stationary stator coils, it would induce corresponding harmonics in line current.

Toliyat *et al* [13] have also proposed the detection of eccentricity through line current spectrum analysis in induction machines. A new method of modeling induction machines was proposed, which is based on the WFA (Winding Function Approach). The key point

is to calculate the magnetizing and mutual inductances accounting for the effect of all space harmonics. Furthermore, Al-Nauim and Toliyat [14] then put forward MWFA (Modified Winding Function Approach) for modeling dynamic eccentricity in synchronous machines, which is valid for all circumferential non-uniform air-gap conditions. Rotor eccentricity fault of dc motors has also been reported by Haji and Toliyat [15].

Ong *et al* [16] have shown that air-gap eccentricity can result in a net magnetic flux around the shaft. This net flux surrounds the rotor shaft and induces alternating current in the loop composed of the shaft, bearing, and the frame of the stator. However to sense the shaft current extra transducers are needed to be installed on the rotor shaft.

Dorrel *et al* [7] analyzed air-gap flux, current and vibration signal as the function of both static and dynamic eccentricity in 3-phase induction motors with the same approach as [9]. A new theoretical analysis was presented to model the interactions between static and dynamic eccentricity and proved that the existence of additional frequency components was caused by both types of eccentricity simultaneously. It was also suggested that vibration analysis should be integrated with line current signature to identify which particular type of eccentricity is dominant.

Bangura *et al* [17] went further and indicated that the frequency components reported earlier due to only mixed eccentricity could also be observed in case of either static or dynamic eccentricity using TSCFE (Time-Stepping Coupled Finite Elements State Space) technique.

As we know, the line current spectrum can be influenced by many different factors including electric supply, static and dynamic load condition, electromagnetic noise, non-linear behaviour of motor, motor geometry and fault conditions [18]. Such a complexity can easily cause some errors in the fault detection. Thus, there are specific requirements about how to extract different features from current, discriminate among various machine conditions and evaluate the severity of faults. Except the classical Fast Fourier Transform (FFT) adopted by most papers, other MCSA based or associated analysis tools include Parkers' Vector approach [19], Finite Element [8,17], Bi-spectrum (third-order spectrum)[20], Eigenanalysis-based frequency estimation (high-resolution

spectra analysis), time-frequency analysis like wavelet [21] and statistical method like Pattern Recognition [22].

With the rapid development of the computer hardware and software, more and more AI (artificial intelligence) based condition monitoring systems are introduced to modern industry. Such techniques require 'a minimum configuration intelligence', since neither detailed analysis of the fault mechanism is necessary, nor is any modeling of the system required. Thus, the fault detection and evaluation can be done without an expert's participation [23]. Generally line currents and voltages are preferred as input signals due to their non-invasive property. The essence of an expert system is to provide expert quality advice, diagnoses and recommendations given to real world problems by using knowledge-based rule. Neural networks (NNs) are a form of multiprocessor computer system to achieve nonlinear function approximation, which use appropriate network built up on artificial neurons. The exact architecture is obtained by trial-and-error procedure. Fuzzy logic (FL) is a problem-solving methodology that provides a simple way to arrive at a definite conclusion based upon vague, ambiguous, imprecise, noisy, or missing input information. In contrast to NN, FL gives a very clear physical description of how function approximation is performed [23]. Fuzzy-NNs are basically combination of FL and NNs. Genetic algorithms (GAs) are stochastic optimization techniques to solve problem to its best by an evolutionary process. Some of their applications are given in [23-26]. The findings from this thesis, for example, can be given as input to the expert system towards building up its the knowledge base.

1.4 Motivations and Thesis Outline

Literature survey suggested that very little have been reported on inclined eccentricity. Only [5, 6] mention it briefly. This provides the motivation for further research in this area. The work presented in the thesis attempts to analyze inclined static eccentricity, generate a suitable model, simulate it to study its characteristics and then validate it by experimental results. Motor Current Signature Analysis (MCSA) will be used to detect the signature of the fault, and a variant of Modified Winding Function Approach (MWFA) needs to be developed to address the change of air-gap length with inclined eccentricity in 3-D space. Slot effects have been omitted as they are not expected

to influence the results significantly [27].

Chapter 2 will present the principle of MCSA. The conditions for generating eccentricity related harmonics are discussed and validated by simulations. The derivation of the MWFA to incorporate incline static eccentricity in 3-D space will be shown in Chapter 3. In order to describe the motor in software program, the coupled magnetic circuit based induction machine model will be explained in Chapter 4. In Chapter 5, a 45-bar induction motor is simulated in MATLAB 6.53 under different faulty cases and load levels. To verify the inductance value obtained using MWFA, a Finite Element based method will be adopted to re-evaluate the motor inductances in Chapter 6. Finally, Chapter 7 gives the experimental results of the simulated machine. Comparisons between simulated and experimental results will be presented in the chapter. Finally, conclusions and future works will be discussed in last Chapter 8.

Chapter 2.

Principle of Motor Current Signature Analysis to Detect Static Eccentricity

2.1 Introduction

As a non-invasive and easily implementable tool, Motor Current Signature Analysis (MCSA) has become the most widely used fault diagnosis strategy in online monitoring systems. Combined with different data analysis techniques, MCSA can detect almost most of common machine abnormalities. This chapter will explain the mechanism of the generation of eccentricity related harmonics in line current, and their relationship with the combination of pole pairs, the number of rotor slots/bars and slip frequency. Some induction motors with different number of bars are simulated to illustrate the predicted components in line current spectrum.

2.2 Mechanism of the Generation of Eccentricity Related Harmonics and Principal Slot Harmonics in Line Current [28]

It has been clearly shown [1,9,29] that the presence of air-gap eccentricity can be detected using Motor Current Signature Approach (MCSA). The equation describing the frequency components of interest is

$$f_h = f\left[(kR \pm n_d)\frac{(1-s)}{p} \pm v\right] \tag{2.1}$$

where

$n_d = 0$	eccentricity order for static eccentricity
n_d=1,2,3...	eccentricity order for dynamic eccentricity
f	the fundamental supply frequency
R	the number of rotor slots
s	the slip

v= 1, 3, 5...	the order of the stator time harmonics that are present in the power supply driving the motor
k	any integer
p	the number of fundamental pole pairs

The principal slot harmonics (PSH) are also given by the above equation with n_d=0, v=1, k=1. In case the pole pairs number associated with these harmonics is a multiple of three, they may not exist theoretically in the line current of a balanced three-phase machine. However due to machine supply and constructional unbalance, some of these harmonics may still be visible even in a healthy machine [30].

According to [28], only those flux components which have a number of pole pairs that match those produced by a balanced three-phase stator winding are the ones that can induce voltage in the winding. Theoretically only a particular combination of machine pole pairs and rotor slot number will give rise to significant PSH or *only* static or *only* dynamic eccentricity related components. Also, even though the static eccentricity and PSH components are given by the same equation, the pole pair numbers associated with them are different. Hence, for the sake of clarity and completeness of the thesis, the relationship between the generation of harmonics of interest and pole pair number is included here. [28]

2.2.1. Healthy Condition [28]

If only the fundamental component of the supply is considered, the MMFs resulting from stator current in a polyphase induction machine can be given as

$$F_s = A\cos(p_n x \pm \omega t) \tag{2.2}$$

where

F_s	MMF in air-gap due to stator current
p_n	= np, p is the number of fundamental pole pairs
A	the peak value of MMF
n	number of space harmonics
ω	line frequency in radian/sec
x	angular position in the stator reference frame.

By neglecting the saturation and slot effects, the specific permeance of air-gap for a healthy machine with uniform air-gap is a constant, which can be expressed as

$$P \approx P_o \tag{2.3}$$

The air-gap flux density components due to the interaction of MMFs and P are given by

$$B_{gs1} = AP_o \cos(p_n x \pm \omega t) \tag{2.4}$$

The equation above is expressed in the stator frame of reference. As we know, stator frame of reference can be transformed into rotor frame of reference by adding $\omega_r t$ (ω_r is the angular rotating speed of rotor) to the rotor referenced angular position x', similarly, rotor frame of reference is transformed into stator frame of reference by subtracting $\omega_r t$ from the stator referenced angular position x [7].

$$x = x' + \omega_r t \qquad \text{stator frame to rotor frame} \tag{2.5}$$

$$x' = x - \omega_r t \qquad \text{rotor frame to stator frame} \tag{2.6}$$

Thus the air flux density in rotor frame of reference are expressed as

$$B_{gr1} = AP_o \cos(p_n(x' + \omega_r t) \pm \omega t) \tag{2.7}$$

Since these flux components are rotating in space, they will induce rotor bar currents, which can be viewed as samples of a continuous sinusoidal current signal with frequency R/p_n times its fundamental. Hence these current will produce additional $(R \pm p_n)$ pole pairs rotor MMF harmonics. Upon acting on P_o, those rotor MMF harmonics can generate new air-gap flux components like

$$B_{gr2} = A_1 P_o^2 \cos[(R \pm p_n)x' \pm p_n \omega_r t \pm \omega t - \phi_1] \tag{2.8}$$

with respect to rotor, or

$$B_{gs2} = A_1 P_o^2 \cos[(R \pm p_n)(x - \omega_r t) \pm p_n \omega_r t \pm \omega t - \phi_1]$$

$$= A_1 P_o^2 \cos[(R \pm p_n)x - R\omega_r t \pm \omega t - \phi_1] \tag{2.9}$$

with respect to stator.

Now substituting ω_r with $((1-s)/p)\omega$ in (2.9) leads to

$$B_{gs2} = A_1 P_o^2 \cos\{(R \pm p_n)x - [R\frac{(1-s)}{p} \pm 1]\omega t - \phi_1\} \tag{2.10}$$

The derivation procedure can also be applied to other time harmonics as described by v in (2.1). The sign $\pm$ before v is attributed to the forward as well as reverse rotating space harmonics. Minus sign represents forward rotating flux and positive sign implies reverse rotating flux, which can be decided from the sign of ω in (2.2).

Now according to (2.10) we can see that the strong PSH in a healthy machine is given as

$$f_{PSH} = \left(R\frac{(1-s)}{p} \pm 1 \right) f \tag{2.11}$$

But in order to generate such harmonics, at least one element of the PSH pole pairs number $(R \pm np)$ should belong to the set (np), the pole pairs number of space harmonics that can be produced by three phase stator winding.

For a balanced three phase winding the harmonics order number n is given by

$$n = 1 \text{ or } 6k \pm 1 \qquad k = 1,2,3... \tag{2.12}$$

So we have

$$R \pm p(6q \pm 1) = p(6m \pm 1) \qquad m,q = 1,2,3... \tag{2.13}$$

After simplification,

$$R = p[6(m \pm q) \pm r] \qquad m \pm q = 0,1,2,3... \quad r = 0 \text{ or } 2 \tag{2.14}$$

$$= 2p[3(m \pm q) \pm u] \qquad m \pm q = 0,1,2,3... \quad u = 0 \text{ or } 1 \tag{2.15}$$

For example, with a $R = 28$, $p = 2$ machine, (2.15) is satisfied with $m \pm q = 2$ and $u = 1$ with positive sign before v. Based on (2.11), the PSHs generated with 60Hz supply and $s = 0.0226$ are 881.3Hz and 761.3Hz respectively for pole pairs 15 and 13 with $n = 1$. Ideally only 761.3Hz component associated with non-triplen 13 pole pairs is

visible and is due to forward rotating flux with minus sign before v. Another machine with 4 poles, 44 bars generate PSH components too with $m \pm q = 4$ and $u = 1$ with negative sign before v. The harmonics are 1324.01Hz and 1204.01 Hz for 23 and 21 pole pairs respectively. Due to the same reason as 28 bars machine, only the component of 1324.01Hz can be detectable, which is attributed to forward rotating flux with positive sign before v. However, for four-pole machines with 42, 43 bars, (2.14) or (2.15) cannot be satisfied. Consequently the PSH harmonics will be invisible in their current spectra. All these simulation results using MATLAB [31] are shown in Fig. 2.1. It is noted that all of current spectra in this thesis are normalized with the base value equal to the amplitude of corresponding fundamental component in dB. All current spectra are shown in dB scale with the amplitude of fundamental component at 0 dB.

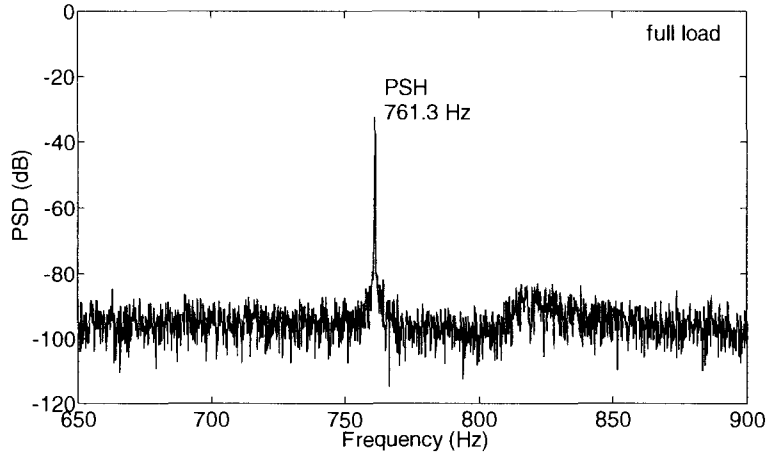

(a)

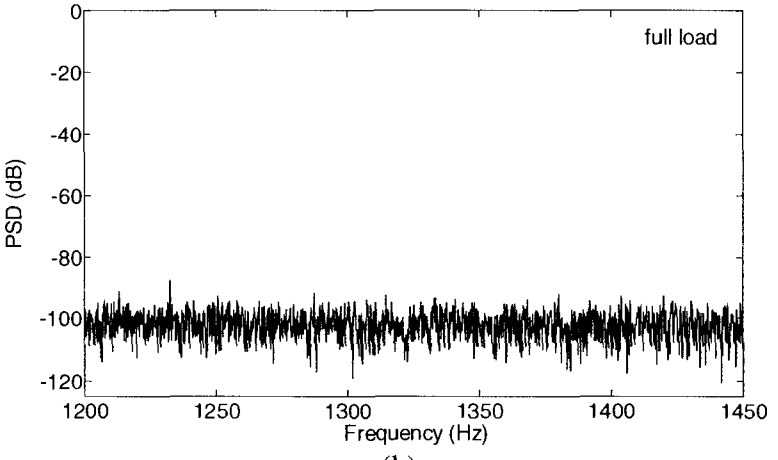

(b)

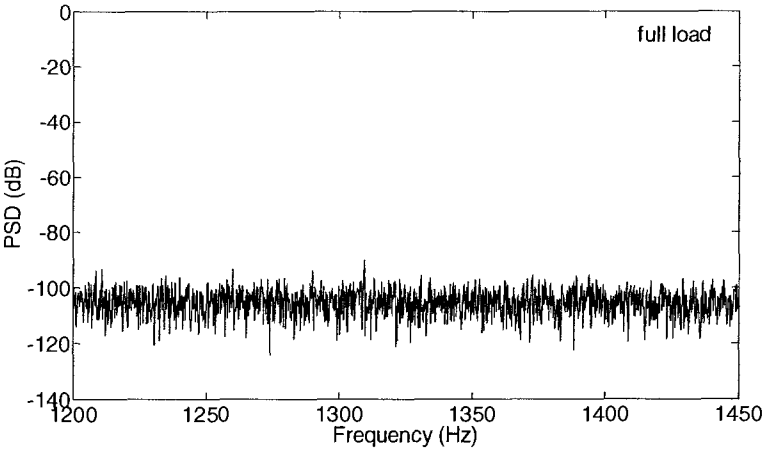

(c)

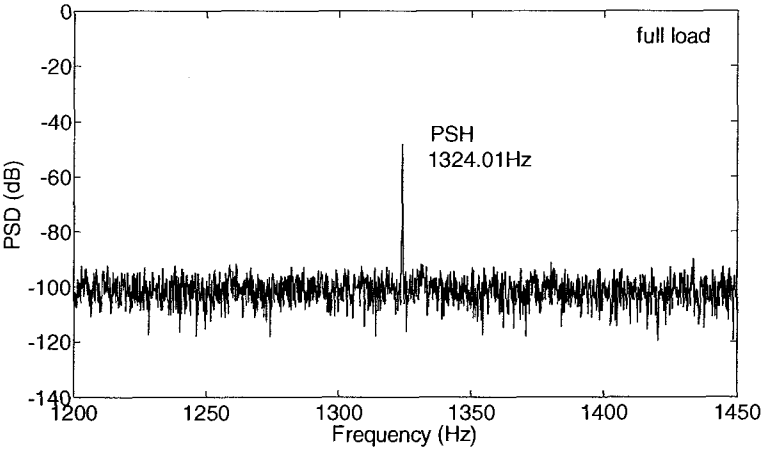

(d)

Figure 2.1 Simulated, normalized line current spectra of healthy machines. From (a) to (d) R= 28, 42, 43, 44. PSH is principal slot harmonics, the amplitude of the fundamental is 0 dB.

2.2.2 Static Eccentricity [28]

In case of static eccentricity, the specific permeance can be expressed as

$$P \approx P_o + P_1 \cos x \tag{2.16}$$

Thus the air-gap flux density components due to the interaction of MMF in (2.2) and permeance in (2.16) with respect to stator can be evaluated as

$$B_{gsse1} = AP_o \cos(p_n x \pm \omega t) + \frac{AP_1}{2}\cos[(p_n - 1)x \pm \omega t] + \frac{AP_1}{2}\cos[(p_n + 1)x \pm \omega t] \tag{2.17}$$

Or with respect to rotor

$$B_{grse1} = AP_o \cos[p_n(x' + \omega_r t) \pm \omega t] + \frac{AP_1}{2}\cos[(p_n - 1)(x' + \omega_r t) \pm \omega t]$$

$$+ \frac{AP_1}{2}\cos[(p_n + 1)(x' + \omega_r t) \pm \omega t] \tag{2.18}$$

Similar to the case of the healthy machine, rotor MMF harmonics of $(R \pm p_n), (R \pm p_n \pm 1)$ pole pairs will be produced due to the sampling effect of discrete rotor bars. Consider first only those terms containing P_o of the resulting MMF interacting with the eccentricity part of (2.16) and those terms containing P_1 interacting with the average part of (2.16), the new air-gap flux components will be produced as

$$B_{grse2} = \frac{A_{21}P_oP_1}{2}\cos[(R \pm p_n \pm 1)x' \pm p_n\omega_r t \pm \omega_r t \pm \omega t - \phi_{21}] \tag{2.19}$$

with respect to rotor, or

$$B_{gsse2} = \frac{A_{21}P_oP_1}{2}\cos[(R \pm p_n \pm 1)x - R\omega_r t \pm \omega t - \phi_{21}] \tag{2.20}$$

with respect to stator.

The other combination between the terms containing P_1 of MMF and the eccentricity part of (2.16) brings up air-gap flux components given like

$$B_{grse3} = \frac{A_{22}P_1^2}{4}\cos[(R \pm p_n \pm 2)x' \pm p_n\omega_r t \pm 2\omega_r t \pm \omega t - \phi_{22}] \tag{2.21}$$

with respect to rotor, or

$$B_{gsse3} = \frac{A_{22}P_1^2}{4}\cos[(R \pm p_n \pm 2)x - R\omega_r t \pm \omega t - \phi_{22}] \tag{2.22}$$

with respect to stator. Substituting $\omega_r = \omega(1-s)/p$ into (2.20) and (22.2), we get results similar to (2.10):

$$B_{gsse2} = \frac{A_{21}P_oP_1}{2}\cos\{(R \pm p_n \pm 1)x - [R\frac{(1-s)}{p} \pm 1]\omega t - \phi_{21}\} \tag{2.23}$$

$$B_{gsse3} = \frac{A_{22}P_1^2}{4}\cos\{(R \pm p_n \pm 2)x - [R\frac{(1-s)}{p} \pm 1]\omega t - \phi_{22}\} \quad (2.24)$$

According to the same rule described in 2.2.1 [at least one element of $(R \pm np \pm 1)$ or $(R \pm np \pm 2)$ should belong to the set (np)], the bar number R, which can make the static eccentricity related harmonics be visible, shall satisfy the following equation:

$$R = 2p[3(m \pm q) \pm u] \pm k \qquad m \pm q = 0,1,2,3... \qquad u = 0 \text{ or } 1, \quad k = 1 \text{ or } 2 \quad (2.25)$$

The meaning of (2.25) is that all machines with bars number R and pole pair number p satisfying (2.25) shall give $(R(1-s)/p \pm v)f$ components in their current spectra in case of static eccentricity. Since that normally $P_1 << P_o$, the components with $k = 2$ in (2.24) are comparably weaker than those in (2.23) and noticeable only under light load conditions. Also it should be noted that though the time varying frequency components in (2.10), (2.23), (2.24) are the same, the pole pairs associated with them are different.

Fig. 2.2 shows the simulated line current spectra of machines with 25% static eccentricity under full load for 28, 42, 43 and 44 bars, respectively. With p=2, the 42 bars machine doesn't give very strong components of interest due to low amplitude for $k = 2$, $(R \pm np \pm 2)$ pole pairs. While 28 and 44 bars machines still produce strong PSHs associated with $(R \pm np)$ pole pairs, 43 bars motor gives the static eccentricity related component at 1297.32 Hz associated with 23 pole pairs for s=0.04083.

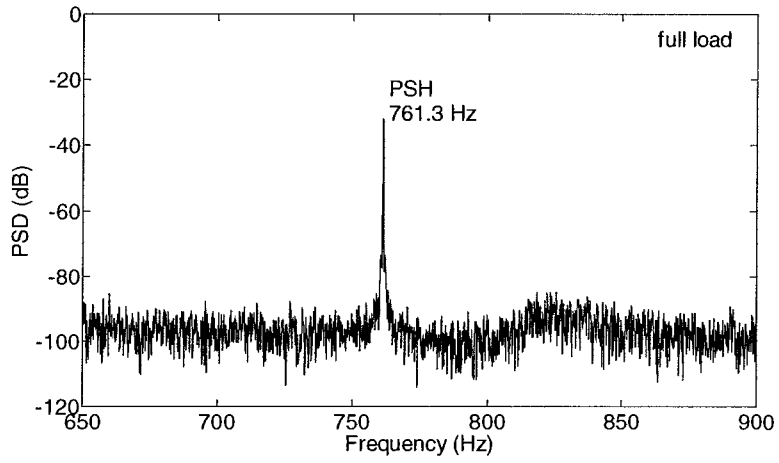

(a)

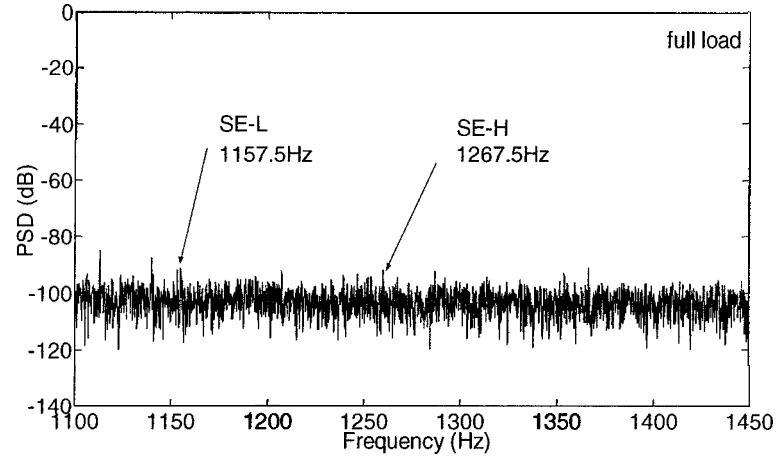

(b)

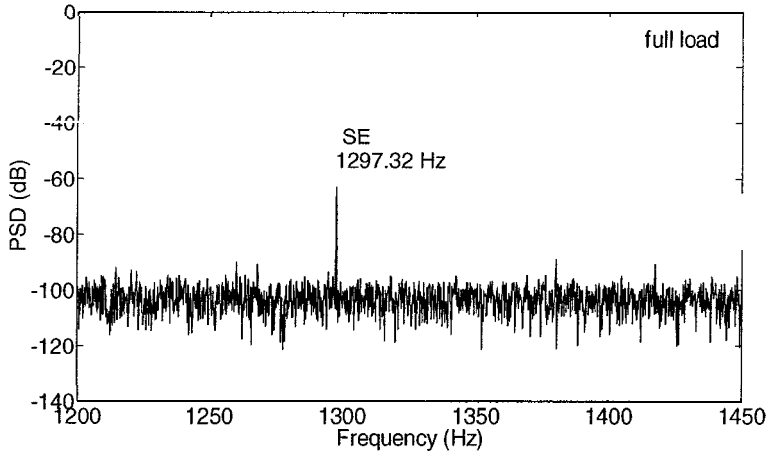

(c)

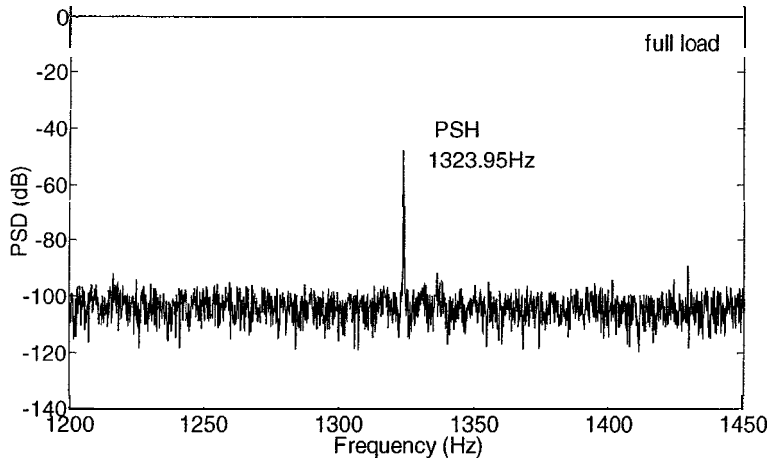

(d)

Figure 2.2 Simulated, normalized line current spectra of machines with uniform 25% SE. From (a) to (d) R= 28, 42, 43, 44. PSH is principal slot harmonics. The amplitude of the fundamental is 0 dB.

2.3 Conclusions

This chapter described the mechanism through which eccentricity related spectral lines appear in the line current spectrum. It was shown that the PSH and static eccentricity components are given by the same formula. The only way to distinguish these components is by pole pair numbers associated with them. Also not all components predicted by the mechanism are detectable. There are other restrictions for these harmonics of interest to be seen, which include the number of rotor slots and the number of pole pairs. MATLAB simulations of motors with different bar numbers were carried out to show the relationship between the components of interest and the combination of pole pairs and bars. In next chapter, MWFA will be introduced to calculate motor inductances under inclined static eccentricity condition.

Chapter 3

MWFA and Calculation of the Inductances in AC Machines

3.1 Introduction

So far research on the detection of radial unequal air-gap in induction machines and synchronous machines have been well documented [13,14,30]. However, few are reported on axial non-uniform air-gap problem. To address the problem by computer simulation, the machine inductances need to be evaluated first. WFA (Winding Function Approach) and MWFA (Modified Winding Function Approach) are frequently used in motor inductance calculation. The former is only limited to uniform air-gap case, while the latter takes the non-uniform circumferential air-gap into consideration. However, since the air-gap length changes in both axial and radial direction if the rotor is inclined, the original MWFA will not be valid to compute inductance. In this chapter, the MWFA will be extended to 3-D to calculate inductances in an induction machine with inclined rotor.

3.2 A Variant of MWFA and Inductance Calculations in 3-D Space

To simplify the equations used to describe ac motor, the following are assumed in this approach [13,32]:

a) Flux is assumed to cross the air-gap radially (axial flux is neglected).
b) Saturation is neglected.
c) Average core saturation is incorporated by using Carter's coefficient to adjust air-gap length.
d) Eddy current, friction and windage losses are neglected.
e) Cage bars are insulated.
f) The magnetic material has infinite permeance.
g) Slot effects have been neglected.

In order to develop the general equations necessary to calculate motor inductance, an elementary doubly cylindrical machine (a cylindrical rotor with a cylindrical stator shell whose axis may not be aligned) is considered, as shown in Fig. 3.1. It's assumed that the infinitesimally thin, current carrying coils are placed axially along the air-gap. The cross sectional area of the wire is assumed as negligible. These windings can be associated with either the stator winding or rotor bars and there are no restrictions on its distribution [33]. In reality, however, the stator windings are placed in slots located on the inner cylindrical wall of the stator, and rotor windings normally may be either (a) die cast aluminium bars in a die-cast rotor or (b) a winding structure similar to stator. For either type of rotor, the rotor conductors are located on the outer cylindrical surface of the rotor. Also, while the motor can exhibit either circumferential or axial non-uniform air-gap, the stator and rotor do not touch each other.

Fig. 3.1 shows the cross section diagram of the machine at some position along the z axis (assumed perpendicular to the plane of the paper), and the z-axis origin point can be chosen at any convenient point on the z-axis. Along the stator periphery an arbitrary point is selected as reference point for $\varphi = 0$.

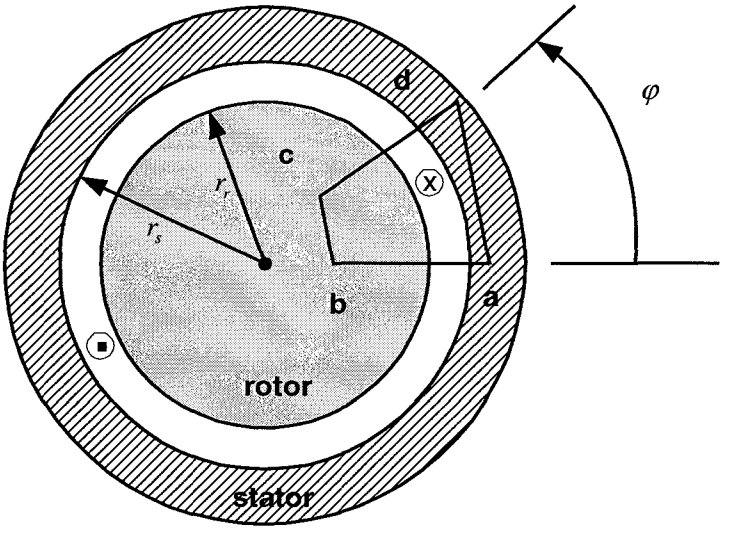

Figure 3.1 The cross section of an elementary doubly cylindrical machine

Now consider a close path shown in Fig. 3.1 where the path ab is chosen across the air-gap from stator to rotor at the reference point and the path cd returns across the

air-gap at an arbitrary angle $\varphi \in [0 \quad 2\pi]$. If Ampere's Law is applied to the close path $abcda$,

$$\oint_{abcda} \vec{H}(\varphi,\theta_r,z) \bullet d\vec{l} = \int_S \vec{J} \bullet d\vec{S} \tag{3.1}$$

where J is the current density and S is the surface enclosed by the path $abcda$, H is the magnetic field intensity, θ_r is the rotor's position with respect to a reference point on the stator. Since all wires carry the same current i, (3.1) can be rewritten as:

$$\oint_{abcda} \vec{H}(\varphi,\theta_r,z) \bullet d\vec{l} = n(\varphi,\theta_r,z)i \tag{3.2}$$

The function $n(\varphi,\theta_r,z)$ is the *turns function* of either stator or rotor representing the net number of winding turns enclosed by the close path. The left term of (3.2) can be extended to for integral intervals, each of which can be evaluated as the magnetomotive force (MMF) drop in the magnetic circuit. In terms of MMF, (3.2) results in:

$$F_{ab}(0,\theta_r,z) + F_{bc} + F_{cd}(\varphi,\theta_r,z) + F_{da} = n(\varphi,\theta_r,z)i \tag{3.3}$$

Since we have assumed infinite permeable magnetic material, the reluctance of iron portion $da \,\&\, bc$ is zero. Hence there will not be any MMF drop across paths *da* & *bc*. Equation (3.3) is then reduced to:

$$F_{ab}(0,\theta_r,z) + F_{cd}(\varphi,\theta_r,z) = n(\varphi,\theta_r,z)i \tag{3.4}$$

Dividing the both sides of (3.4) by the effective air-gap length $g(\varphi,\theta_r,z)$, and integrating with respect to the stator angle from 0 to 2π,

$$\int_0^{2\pi} \frac{F_{ab}(0,\theta_r,z)}{g(\varphi,\theta_r,z)} d\varphi + \int_0^{2\pi} \frac{F_{cd}(\varphi,\theta_r,z)}{g(\varphi,\theta_r,z)} d\varphi = \int_0^{2\pi} \frac{n(\varphi,\theta_r,z)i}{g(\varphi,\theta_r,z)} d\varphi \tag{3.5}$$

According to Gauss' Theorem that the net flux leaving any closed surface is zero, we have

$$\oint_S \vec{B} \bullet d\vec{S} = 0 \tag{3.6}$$

where B is the magnetic flux density and S is an arbitrary closed surface. The surface S is chosen to be a closed cylindrical surface of radius r, located between r_r, the outer radius of the rotor and r_s, the inner radius of stator. Thus,

$$\int_0^{2\pi}\int_{-\varepsilon}^{\varepsilon} \mu_o r H(\varphi,\theta_r,z)\,dz\,d\varphi = 0, \qquad r_r < r < r_s \tag{3.7}$$

where ε is a real positive quantity and $\varepsilon \to 0$, dz is an infinitesimal length along the z axis of the cylinder.

Here, we define

$$H(\varphi,\theta_r,z) = H(\varphi,\theta_r)\cdot\delta(z), \quad z\in[-\varepsilon \quad \varepsilon] \tag{3.8}$$

where $\delta(z)$ is the unit impulse function.

Therefore, (3.7) can be written as

$$\int_0^{2\pi}\int_{-\varepsilon}^{\varepsilon} \mu_o r H(\varphi,\theta_r)\cdot\delta(z)\,dz\,d\varphi = 0 \tag{3.9}$$

or

$$\int_0^{2\pi} H(\varphi,\theta_r)\,d\varphi \int_{-\varepsilon}^{\varepsilon} \delta(z)\,dz = 0 \tag{3.10}$$

From the definition of unit impulse function

$$\int_{-\varepsilon}^{\varepsilon} \delta(z)\,dz = 1 \tag{3.11}$$

Hence, (3.10) becomes

$$\int_0^{2\pi} H(\varphi,\theta_r)\,d\varphi = 0 \tag{3.12}$$

Multiplying both sides of (3.12) by $\delta(z)$ and using (3.8) will give

$$\int_0^{2\pi} H(\varphi,\theta_r,z)\,d\varphi = 0 \tag{3.13}$$

As we know,

$$H(\varphi,\theta_r,z)=\frac{F(\varphi,\theta_r,z)}{g(\varphi,\theta_r,z)} \tag{3.14}$$

Then,

$$\int_0^{2\pi}\frac{F(\varphi,\theta_r,z)}{g(\varphi,\theta_r,z)}d\varphi=0 \tag{3.15}$$

Thus, the second term on the left of (3.5) is zero, and yields

$$F_{ab}(0,\theta_r,z)=\frac{1}{2\pi\left\langle g^{-1}(\theta_r,z)\right\rangle}\int_0^{2\pi}n(\varphi,\theta_r,z)g^{-1}(\varphi,\theta_r,z)id\varphi \tag{3.16}$$

where

$$\left\langle g^{-1}(\theta_r,z)\right\rangle=\frac{1}{2\pi}\int_0^{2\pi}g^{-1}(\varphi,\theta_r,z)d\varphi \tag{3.17}$$

Substituting equation (3.16) into (3.4) and solving for F_{cd} gives

$$F_{cd}(\varphi,\theta_r,z)=n(\varphi,\theta_r,z)i-\frac{1}{2\pi\left\langle g^{-1}(\theta_r,z)\right\rangle}\int_0^{2\pi}n(\varphi,\theta_r,z)g^{-1}(\varphi,\theta_r,z)id\varphi \tag{3.18}$$

Dividing (3.18) by i, the modified winding function at any position along 'z' axis can be defined as,

$$M(\varphi,\theta_r,z)=\frac{F_{cd}(\varphi,\theta_r,z)}{i} \tag{3.19}$$

$$M(\varphi,\theta_r,z)=n(\varphi,\theta_r,z)-\frac{1}{2\pi\left\langle g^{-1}(\theta_r,z)\right\rangle}\int_0^{2\pi}n(\varphi,\theta_r,z)g^{-1}(\varphi,\theta_r,z)d\varphi \tag{3.20}$$

The modified winding function actually represents the MMF distribution in the air-gap due to unit current flowing in the winding. We define the second term on the right of (3.20) as the average part of modified winding function $\left\langle M(\theta_r,z)\right\rangle$,

$$\left\langle M(\theta_r,z)\right\rangle=\frac{1}{2\pi\left\langle g^{-1}(\theta_r,z)\right\rangle}\int_0^{2\pi}n(\varphi,\theta_r,z)g^{-1}(\varphi,\theta_r,z)d\varphi \tag{3.21}$$

Then the MWF equation is given as:

$$M(\varphi,\theta_r,z) = n(\varphi,\theta_r,z) - \langle M(\theta_r,z)\rangle \tag{3.22}$$

Consider now that a winding A with current i_A flowing in it produces the MMF distribution in the air-gap,

$$F_A(\varphi,\theta_r,z) = M_A(\varphi,\theta_r,z)i_A \tag{3.23}$$

The flux linkage in another winding B over an infinitesimal length along 'z' axis due to current in A can be evaluated using the turns function of winding B $n_B(\varphi,\theta_r,z)$ located between φ_1 and φ_2. Since $n_B(\varphi,\theta_r,z)$ is equal to zero except in the integrating region $[\varphi_1 \quad \varphi_2]$, the integrating region can be extended to whole surface

$$d\lambda_{BA}(\theta_r,z) = \mu_o r dz \int_0^{2\pi} n_B(\varphi,\theta_r,z) M_A(\varphi,\theta_r,z) g^{-1}(\varphi,\theta_r,z) i_A d\varphi \tag{3.24}$$

Hence, the mutual inductance dL_{BA} is defined as the flux linkage per unit current:

$$dL_{BA}(\theta_r,z) = \frac{d\lambda_{BA}(\theta_r,z)}{i_A}$$

$$= \mu_o r dz \int_0^{2\pi} n_B(\varphi,\theta_r,z) M_A(\varphi,\theta_r,z) g^{-1}(\varphi,\theta_r,z) d\varphi \tag{3.25}$$

Substituting (3.22) into (3.25) will produce

$$dL_{BA}(\theta_r,z) = \mu_o r dz \left[\int_0^{2\pi} n_A(\varphi,\theta_r,z) n_B(\varphi,\theta_r,z) g^{-1}(\varphi,\theta_r,z) d\varphi \right.$$

$$\left. - \langle M_A(\theta_r,z)\rangle \int_0^{2\pi} n_B(\varphi,\theta_r,z) g^{-1}(\varphi,\theta_r,z) d\varphi \right] \tag{3.26}$$

And the integral part of the second term can be simplified again using (3.21), so (3.26) can be written as

$$dL_{BA}(\theta_r,z) = \mu_o r dz \left[\int_0^{2\pi} n_A(\varphi,\theta_r,z) n_B(\varphi,\theta_r,z) g^{-1}(\varphi,\theta_r,z) d\varphi \right.$$

$$\left. - 2\pi \langle M_A(\theta_r,z)\rangle \langle M_B(\theta_r,z)\rangle \langle g^{-1}(\theta_r,z)\rangle \right] \tag{3.27}$$

Now the mutual inductance between coil B and coil A can be written as:

$$L_{BA}(\theta_r) = \int_0^{ls} dL_{AB}(\theta_r, z) \tag{3.28}$$

where l_s is the stack length.

Combined (3.27) and (3.28), $L_{BA}(\theta_r)$ can be computed as:

$$L_{BA}(\theta_r) = \mu_o r [\int_0^{ls}\int_0^{2\pi} n_A(\varphi,\theta_r,z) n_B(\varphi,\theta_r,z) g^{-1}(\varphi,\theta_r,z) d\varphi dz$$

$$- 2\pi \int_0^{ls} \langle M_A(\theta_r,z)\rangle \langle M_B(\theta_r,z)\rangle \langle g^{-1}(\theta_r,z)\rangle dz] \tag{3.29}$$

As long as the magnetic field is linear, it can be easily proved following [34], that

$$L_{BA} = L_{AB} \tag{3.30}$$

3.3 Air-gap length of Inclined Static Eccentricity

In case of pure static eccentricity as illustrated in Fig. 1.1, the position of radial minimal air-gap length is fixed in space. The air-gap length at any angular position φ can be expressed as:

$$g(\varphi) = g_o(1 - a\cos\varphi) \tag{3.31}$$

where g_o is the average air-gap length in a symmetric machine, a is the static eccentricity ratio that is given by:

$$a = \frac{g_{\max} - g_{\min}}{2g_o} \tag{3.32}$$

$$g_o = \frac{g_{\max} + g_{\min}}{2} \tag{3.33}$$

where $g_{\max}$ and $g_{\min}$ are the maximum and minimum air-gap around the stator respectively.

If the rotor is axially inclined, it also causes static eccentricity shown in Fig. 1.2. However, a will not be a constant, but the function of the position along the axial

direction. Here it is assumed that the axis of the rotor and the axis of the stack are still in the same geometric plane.

Through geometric analysis on Fig. 1.2, it's easy to show that the eccentricity ratio at any point along the shaft is:

$$a = C_1 + C_2 z \tag{3.34}$$

where

$$C_1 = \frac{1}{2}(2a_o - \frac{l_s}{g_o}\sin\beta) \tag{3.35}$$

$$C_2 = \frac{\tan\beta}{g_o} \tag{3.36}$$

And a_o is the pure static eccentricity ratio at the midpoint of the rotor, β is the angle of inclination of the rotor.

Thus the air-gap at any point z & φ is given as:

$$g(\varphi, z) = g_o[1 - a(z)\cos\varphi] \tag{3.37}$$

By using Fourier series analysis, the inverse air-gap length is given approximately as [13]:

$$g^{-1}(\varphi, z) = \sum_{i=1}^{\infty} D_i Cos(i-1)\varphi \approx D_1 + D_2\cos\varphi \tag{3.38}$$

where

$$D_1 = \frac{1}{g_o\sqrt{1-a(z)^2}} \tag{3.39}$$

$$D_2 = \frac{2}{g_o\sqrt{1-a(z)^2}}(\frac{1-\sqrt{1-a(z)^2}}{a(z)}) \tag{3.40}$$

3.4 Conclusions

To deal with the axial non-uniform air-gap problem, a variant of MWFA is derived based on an elementary cylindrical machine. This version of modified winding function does not have any assumptions about the air-gap and winding distribution, so that any winding distribution and non-uniform air-gap in any direction can be incorporated. It can therefore be applied to many complex uneven air-gap problems, such as bent shaft or core ovality. The evaluation of air-gap length for inclined static eccentricity is also given in this chapter. Once the inductances values are obtained, they can be incorporated in the circuital equations for dynamic simulation of the induction motor. The equations describing the mathematical model of induction motor will be discussed in the next chapter.

Chapter 4

Coupled Magnetic Circuit Based State Space Model of Induction Motor

4.1 Introduction

With inductance values obtained from MWFA, it is time to choose an appropriate mathematical model to simulate the whole machine. Based on the coupled magnetic approach, a general model of single phase or multi-phase ac motor has been derived in [13, 32]. The machine is regarded as a system of coupled magnetic circuits with coupling impedances used to define the interaction between various circuits. The effects of non-sinusoidal air-gap MMF produced by both the stator and the rotor currents have been incorporated into the model. With many assumptions to neglect saturation and slot effects, this model reduces the complexity of coding and computations dramatically.

4.2 Induction Motor Model

The voltage equations for stator windings can be written as:

$$V_s = R_s I_s + \frac{d\Lambda_s}{dt} + V_g \tag{4.1}$$

where the stator flux linkage Λ_s is given by

$$\Lambda_s = L_{ss} I_s + L_{sr} I_r \tag{4.2}$$

$$V_s = \begin{bmatrix} v_{s1} & v_{s2} & v_{s3} \end{bmatrix}^t \tag{4.3}$$

$$I_s = \begin{bmatrix} i_{s1} & i_{s2} & i_{s3} \end{bmatrix}^t \tag{4.4}$$

$$I_r = \begin{bmatrix} i_{r1} & i_{r2} & \cdots & i_m & i_e \end{bmatrix} \tag{4.5}$$

$$V_g = \begin{bmatrix} v_g & v_g & v_g \end{bmatrix} \tag{4.6}$$

V_s is the supply voltage vector and V_g is the neutral voltage vector. I_s and I_r are stator current vector, rotor bar and end-ring current vector respectively. R_s is a 3×3 diagonal matrix whose diagonal elements are the resistances of each stator phase. L_{ss} is a 3×3 symmetric matrix of stator inductances. n is the number of rotor bars. L_{sr} is a 3 by (n+1) matrix consisting of the mutual inductances between each stator phase and rotor bars, end-ring.

$$R_s = \begin{bmatrix} r_s & 0 & 0 \\ 0 & r_s & 0 \\ 0 & 0 & r_s \end{bmatrix} \tag{4.7}$$

$$L_{ss} = \begin{bmatrix} L_{ss11} + L_{ls} & L_{ss12} & L_{ss13} \\ L_{ss21} & L_{ss22} + L_{ls} & L_{ss23} \\ L_{ss31} & L_{ss32} & L_{ss33} + L_{ls} \end{bmatrix} \tag{4.8}$$

$$L_{sr} = \begin{bmatrix} L_{sr11} & L_{sr12} & \cdots & L_{sr1n} & L_{sr1e} \\ L_{sr21} & L_{sr22} & \cdots & L_{sr2n} & L_{sr2e} \\ L_{sr31} & L_{sr32} & \cdots & L_{sr3n} & L_{sr3e} \end{bmatrix} \tag{4.9}$$

L_{ls} is the leakage inductance of a stator phase. L_{ssij} is the mutual inductance between two stator phases "*i*" and "*j*". L_{srij} is the mutual inductance between stator phase "*i*" and rotor loop "*j*".

Equation (4.1) can be rewritten as by substituting (4.2) into it as:

$$V_s = R_s I_s + L_{ss}\frac{dI_s}{dt} + \omega_r \frac{dL_{sr}}{d\theta_r} I_r + L_{sr}\frac{dI_r}{dt} + V_g \tag{4.10}$$

where θ_r is the spatial position of the rotor, and the rotor mechanical speed ω_r is

$$\omega_r = \frac{d\theta_r}{dt} \tag{4.11}$$

As we know, the following equation is always valid for a star connected machine without neutral line:

$$i_{s1} + i_{s2} + i_{s3} = 0 \tag{4.12}$$

or $$i_{s3} = -i_{s1} - i_{s2} \tag{4.13}$$

Equation (4.10) actually includes a set of three equations representing three stator phase voltages in forms of:

$$v_{si} = f(I_s, I_r, \omega_r) \qquad i=1,2,3 \tag{4.14}$$

With the help of (4.13), (4.10) can be reduced to only a set of two line-line voltage equations by subtracting equation phase 2 from phase 1, phase 3 from phase 2:

$$V_{su} = R_{su} I_{su} + L_{ssu} \frac{dI_{su}}{dt} + \omega_r \frac{dL_{sru}}{d\theta_r} I_r + L_{sru} \frac{dI_r}{dt} \tag{4.15}$$

where

$$V_{su} = [v_{s1} - v_{s2} \quad v_{s2} - v_{s3}]^t \tag{4.16}$$

$$I_{su} = [i_{s1} \quad i_{s2}]^t \tag{4.17}$$

$$R_{su} = \begin{bmatrix} r_s & -r_s \\ r_s & 2r_s \end{bmatrix} \tag{4.18}$$

$$L_{ssu} = \begin{bmatrix} L_{ss11} - L_{ss21} - L_{ss13} + L_{ss23} + L_{ls} & L_{ss12} - L_{ss22} - L_{ss13} + L_{ss23} - L_{ls} \\ L_{ss21} - L_{ss31} - L_{ss23} + L_{ss33} + L_{ls} & L_{ss22} - L_{ss32} - L_{ss23} + L_{ss33} + L_{ls} \end{bmatrix} \tag{4.19}$$

$$L_{sru} = \begin{bmatrix} L_{sr11} - L_{sr21} & L_{sr12} - L_{sr22} & \cdots & L_{sr1n} - L_{sr2n} & L_{sr1e} - L_{sr2e} \\ L_{sr21} - L_{sr31} & L_{sr22} - L_{sr32} & \cdots & L_{sr2n} - L_{sr3n} & L_{sr2e} - L_{sr3e} \end{bmatrix} \tag{4.20}$$

Through such a simple transformation that has not been reported before, the number of unknowns (stator current) is reduced by 1 and the dimensions of coefficient matrices also decreased. Hence the total amount of simulation time can be saved.

The cage rotor is viewed as a set of mutually coupled loops with equations given as:

$$V_r = R_r I_r + \frac{d\Lambda_r}{dt} \tag{4.21}$$

where V_r is a null matrix of dimension 1 by n+1; the rotor flux linkage Λ_r is given by

$$\Lambda_r = L_{rr} I_r + L_{rsu} I_{su} \tag{4.22}$$

R_r is a (n+1) × (n+1) symmetric matrix of rotor bars and end-rings resistances. L_{rr} is a (n+1) × (n+1) symmetric matrix of rotor bars and end-rings inductances. L_{rsu} is a (n+1) × 2 matrix, which is the transpose of L_{sru} following (3.30).

$$R_r = \begin{bmatrix} 2(r_b+r_e) & -r_b & 0 & \cdots & 0 & -r_b & -r_e \\ -r_b & 2(r_b+r_e) & -r_b & \cdots & 0 & 0 & -r_e \\ \vdots & \vdots & \vdots & \cdots & \vdots & \vdots & \vdots \\ \vdots & \vdots & \vdots & \cdots & \vdots & \vdots & \vdots \\ 0 & 0 & 0 & \cdots & 2(r_b+r_e) & -r_b & -r_e \\ -r_b & 0 & 0 & \cdots & -r_b & 2(r_b+r_e) & -r_e \\ -r_e & -r_e & -r_e & \ldots & -r_e & -r_e & nr_e \end{bmatrix} \tag{4.23}$$

$L_{rr} =$

$$\begin{bmatrix} 2(L_b+L_e)+L_{mr} & L_{rr12}-L_b & L_{rr13} & \cdots & L_{rr1,n-1} & L_{rr1n}-L_b & -L_e \\ L_{rr21}-L_b & 2(L_b+L_e)+L_{mr} & L_{rr23}-L_b & \cdots & L_{rr2,n-1} & L_{rr2n} & -L_e \\ \vdots & \vdots & \vdots & \cdots & \vdots & \vdots & \vdots \\ \vdots & \vdots & \vdots & \cdots & \vdots & \vdots & \vdots \\ L_{rrn-1,1} & L_{rrn-1,2} & L_{rrn-1,3} & \cdots & 2(L_b+L_e)+L_{mr} & L_{rrn-1,n}-L_b & -L_e \\ L_{rrn1}-L_b & L_{rrn2} & L_{rrn3} & \cdots & L_{rrn,n-1}-r_b & 2(L_b+L_e)+L_{mr} & -L_e \\ -L_e & -L_e & -L_e & \ldots & -L_e & -L_e & nL_e \end{bmatrix} \tag{4.24}$$

where L_{mr} is the magnetizing inductance of each rotor loop, L_b is the rotor bar leakage inductance, L_e is the rotor end ring leakage inductance, and L_{rrij} is the mutual inductance between two rotor loops 'i' and 'j'.

By substituting (4.11) and (4.22) into (4.21), we can get:

$$V_r = R_r I_r + L_{rr}\frac{dI_r}{dt} + \omega_r \frac{dL_{rr}}{d\theta_r} I_r + \omega_r \frac{dL_{rsu}}{d\theta_r} I_{su} + L_{rsu}\frac{dI_{su}}{dt} \tag{4.25}$$

Neglecting damping, the mechanical equation of the machine is given as:

$$T_e - T_L = J_k \frac{d^2\theta_r}{dt^2} = J_k \frac{d\omega_r}{dt} \tag{4.26}$$

where T_e is the electromagnetic torque produced by the machine, T_L is the load torque; J_k is the mechanical inertia of the machine. The electrical torque can be calculated from the following equation:

$$T_e = \left[\frac{\partial W_{co}}{\partial \theta_r}\right]_{(Is,\ Ir \text{ are assumed independent of } \theta r)} \tag{4.27}$$

In a linear magnetic system the co-energy W_{co} is equal to the stored magnetic energy in air-gap:

$$W_{co} = 0.5(I_s{}^t L_{ss} I_s + I_s{}^t L_{sr} I_r + I_r{}^t L_{rs} I_s + I_r{}^t L_{rr} I_r) \tag{4.28}$$

However, since L_{ss} is independent of θ_r even under inclined static eccentricity condition, only the other three terms in (4.28) will be used in calculation of torque. With $X = [I_{su} \quad I_r \quad \omega_r \quad \theta_r]^t$ as state variables, we can organize equations (4.11), (4.15), (4.25) and (4.26) into standard state space equations in the form of:

$$\dot{X} = AX + BU \tag{4.29}$$

4.3 Conclusions

Selection of an appropriate mathematical model of the physical system is critical to a system simulation. The induction model used in this thesis regards the motor as a system of different magnetic circuits by considering the currents in two stator phases and rotor loops are independent variables. The machine speed and rotor position are also combined with the currents variables and solved simultaneously in order to avoid computational errors. The main equations needed to simulate the performance of the machine are explained one by one. The details of all coefficient matrices are given. The simulation efficiency could be improved by simulating two line-line voltage equations rather than three phase voltage equations, because the number of variables is reduced by one. Once the inductances have been obtained using MWFA and the suitable mathematical model of the machine has been formed, it is ready to be simulated in the form of (4.29) using MATLAB [31].

Chapter 5

Simulation of a 3-phase Induction Motor with Inclined Static Eccentricity

5.1 Introduction

Based on the results from last two chapters, a 3-phase induction motor is simulated to detect different eccentricity conditions. The normalized spectrum of steady state line current can be used to detect the signature of specific faults. At first, the simulated inductance values are presented for different faulty cases in 5.2. The simulation results of the whole system are then discussed in 5.3. The results of different cases shall be compared to find the features of this type of fault. Conclusions made based on the data are presented in 5.4.

5.2 Simulation Results of Motor Inductances

The specific machine being studied in this thesis is a 3-phase, four-pole, 2 kW, 208 V star connected induction motor. It has a stator of 36 slots, and a cage rotor of 45 bars. The rotor bars are skewed by 11 degrees. The stator winding is short-pitched (6 slots) double-layer winding. The detailed specification can be found in the Appendix A.

The winding distribution of one stator phase is illustrated in Fig. 5.1. The connection of 3-phase windings is shown as follows (superscript ′: bottom layer conductor):

A: 36′-30-35′-29-34′-28-1-7′-2-8′-3-9′-18′-12-17′-11-16′-10-19-25′-20-26′-21-27′

B: 3′-33-2′-32-1′-31-22-28′-23-29′-24-30′-21′-15-20′-14-19′-13-4-10′-5-11′-6-12′

C: 33′-27-32′-26-31′-25-16-22′-17-23′-18-24′-15′-9-14′-8-13′-7-34-4′-35-5′-34-6′

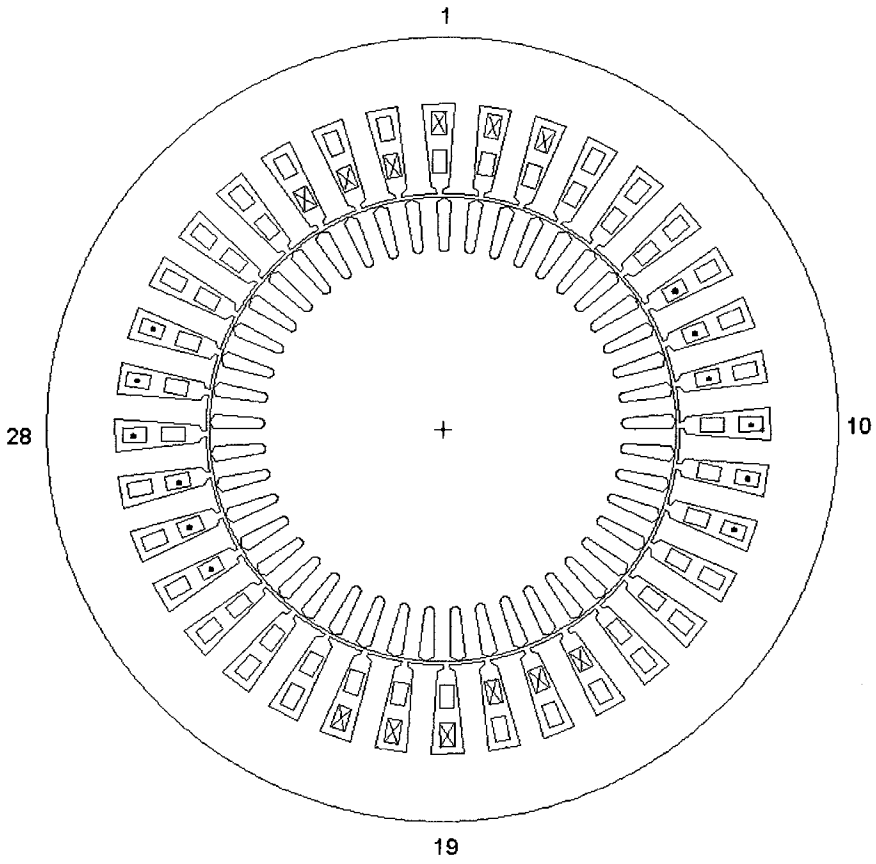

Figure 5.1 Stator winding distribution of phase A (×: current going perpendicularly inside the plane of paper, •: current going perpendicularly outside the plane of paper). Slot numbers 1,10,19,28 are shown for easy identification of slots.

Once the layout of the windings is known, the turns functions for the i_{th} phase and the j_{th} rotor loop could be derived by using Fourier series:

$$n_{si}(\varphi)=\frac{3N}{2}+\sum_{h=1,3,5\ldots}^{\infty}\frac{2N}{\pi h}\sin\frac{h\pi}{3}(1+2\cos\frac{h\pi}{9})\cos(2h(\varphi-(i-1)\frac{\pi}{3})) \tag{5.1}$$

and

$$n_{rj}(\varphi,\theta_r)=\frac{\alpha}{2\pi}+\sum_{h=1,2,3\ldots}^{\infty}\frac{4}{\pi h^2\beta}\sin\frac{h\alpha}{2}\sin\frac{h\gamma}{2}\cos[h(\varphi-(j-1)\alpha-\theta_r)] \tag{5.2}$$

where i=1, 2 or 3; j=1, 2, 3... R; $\alpha=2\pi/R$, R is the number of rotor bars, N is the stator turns in series. γ is the skewing angle. Fig. 5.2 illustrates the turns functions and the winding functions of stator phase a and rotor loop 1.

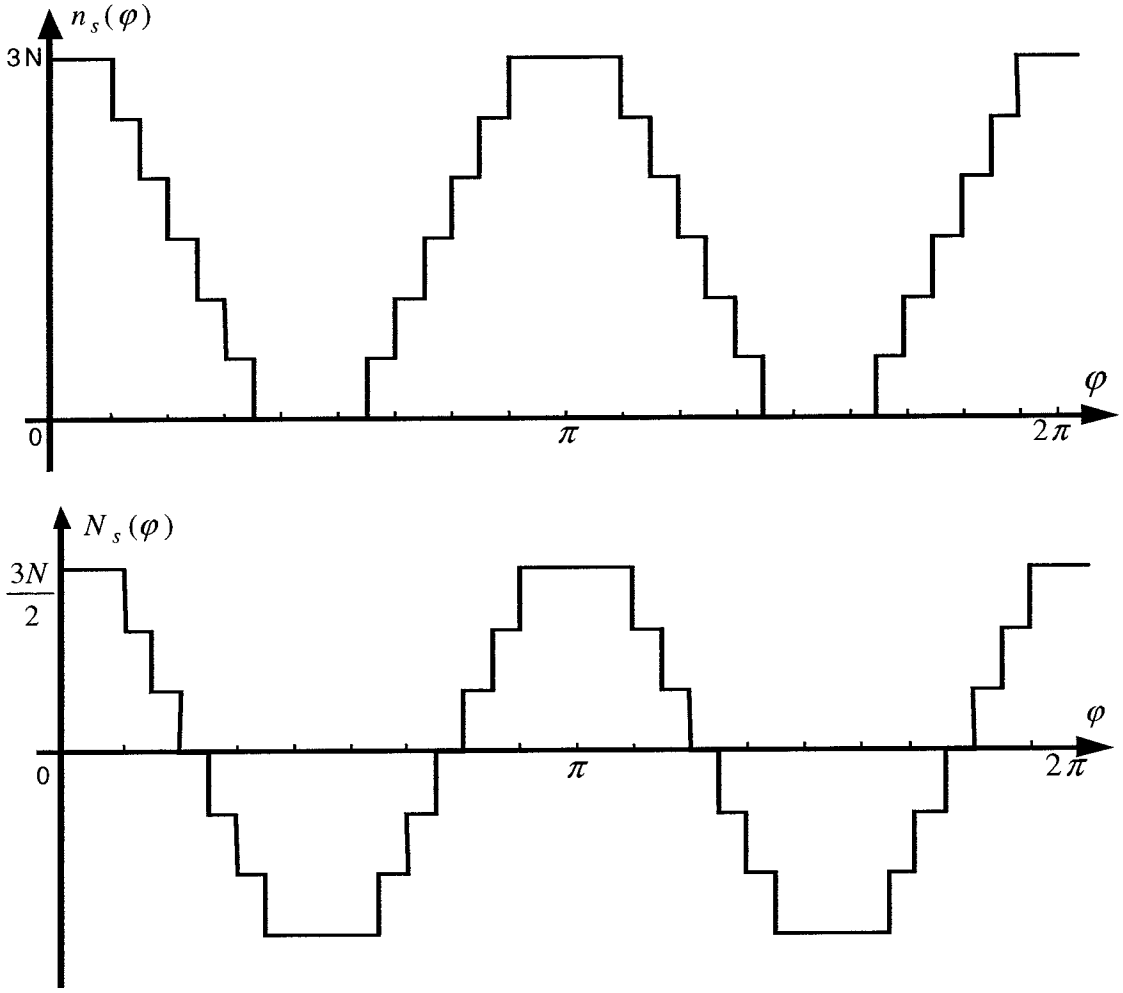
$n_s(\varphi)$
3N
0
π
2π
φ
$N_s(\varphi)$
$\frac{3N}{2}$
0
π
2π
φ

(a)

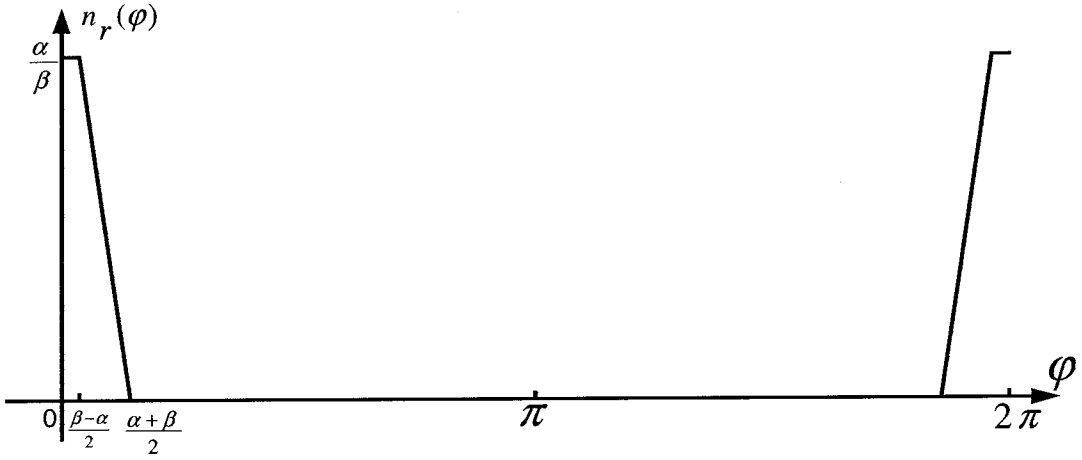
$n_r(\varphi)$
$\frac{\alpha}{\beta}$
0
$\frac{\beta-\alpha}{2}$
$\frac{\alpha+\beta}{2}$
π
2π
φ

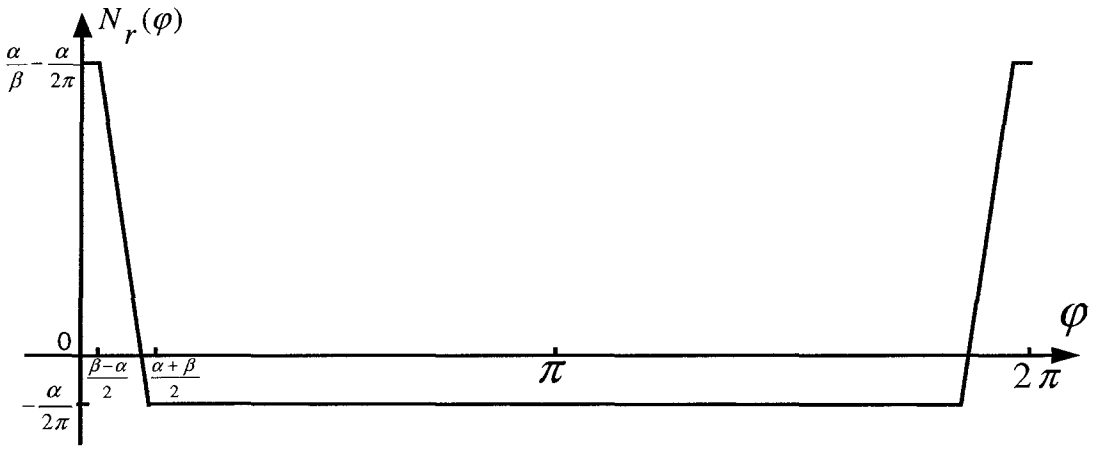

(b)

Figure 5.2 Turns functions n(φ) and winding functions N(φ) of (a) stator phase *a* and (b) rotor loop 1

Using the variant of MWFA discussed in Chapter 3, all motor inductances could be evaluated for healthy or faulty cases. The variation of mutual inductance L_{sra1} (between stator phase *a* and rotor loop 1) and its derivative with respect to rotor position under the healthy condition are shown in Fig. 5.3. The mutual inductances between phases *b* or *c* and rotor loop 1 can be obtained by shifting those curves to the right by 6δ or 12δ where δ is the mechanical angle between two stator slots. The mutual inductance between phase *a* and the *n*th rotor loop is same as given in Fig. 5.3, but shifted to the left by $(n-1)\alpha$ where α is the mechanical angle between two rotor bars.

With static eccentricity, the magnetizing and mutual inductances between rotor loops would be the function of rotor position rather than constant for healthy condition. Fig. 5.4 gives plots of some mutual inductances and their derivatives under 50% static eccentricity, which are L_{sra1} (between phase *a* and loop 1), L_{rr11} (between rotor loop 1 and loop 1).

When the rotor is inclined, all the mutual inductances become the function of not only the rotor position but also the position along the shaft. Fig. 5.5 shows the same cases as given in Fig. 5.4 for inclined static eccentricity with static eccentricity equal 50% at one end and –50% at the other end. It can be observed that the inductances change along both θ_r axis (rotor position) and z axis (shaft direction). It is noted that the stator magnetizing inductance and mutual inductance between different phases are always

constants under above cases. There are more plots of inductances for non-uniform air-gap shown in Appendix B.

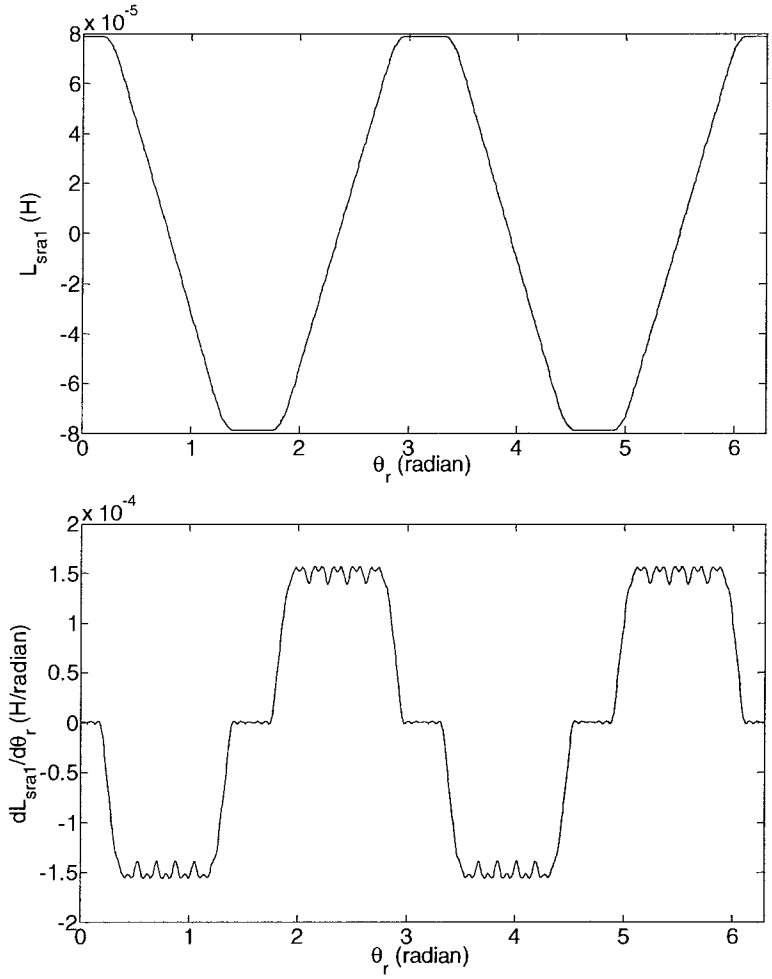

Figure 5.3 Mutual inductance L_{sra1} (top) and its derivative (bottom) with respect to rotor position between phase *a* and rotor loop 1 without rotor eccentricity

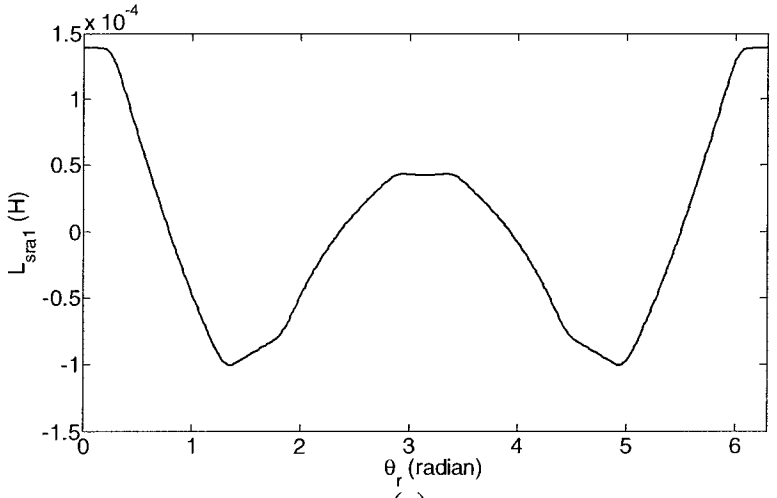

(a)

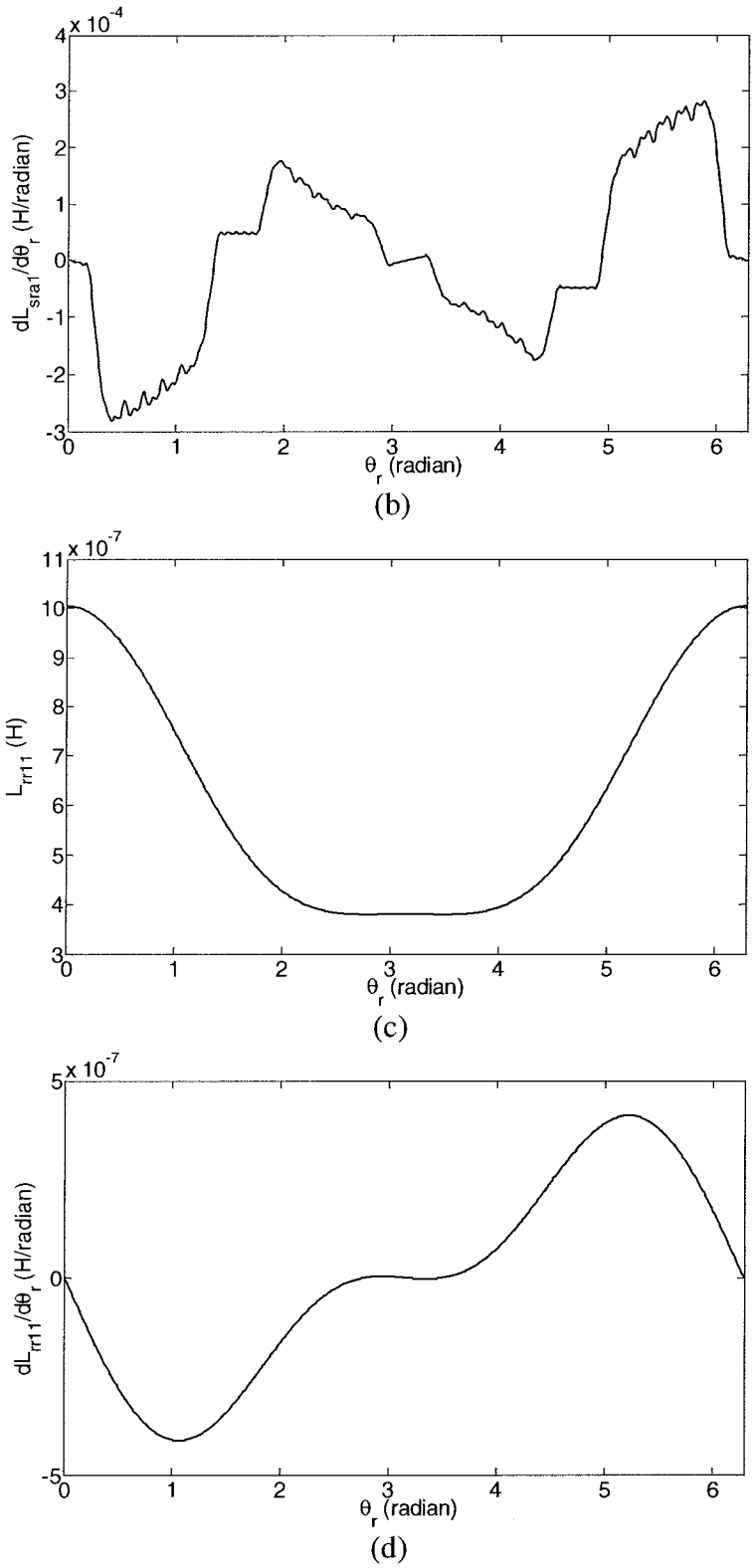

Figure 5.4 Mutual inductances and their derivatives under uniform 50% SE, (a) L_{sra1}, between stator phase a and rotor loop 1; (b) $dL_{sra1}/d\theta_r$; (c) L_{rr11}, between rotor loop 1 and loop 1; (d) $dL_{rr11}/d\theta_r$.

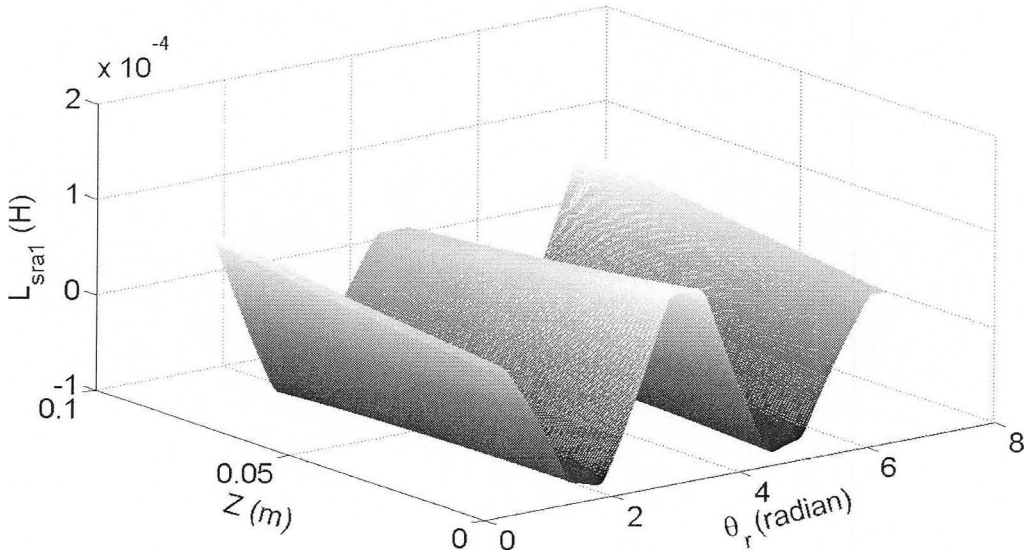
x 10^-4
2
1
0
-1
L_sra1 (H)
0.1
0.05
Z (m)
0
0
2
4
6
8
θ_r (radian)

(a)

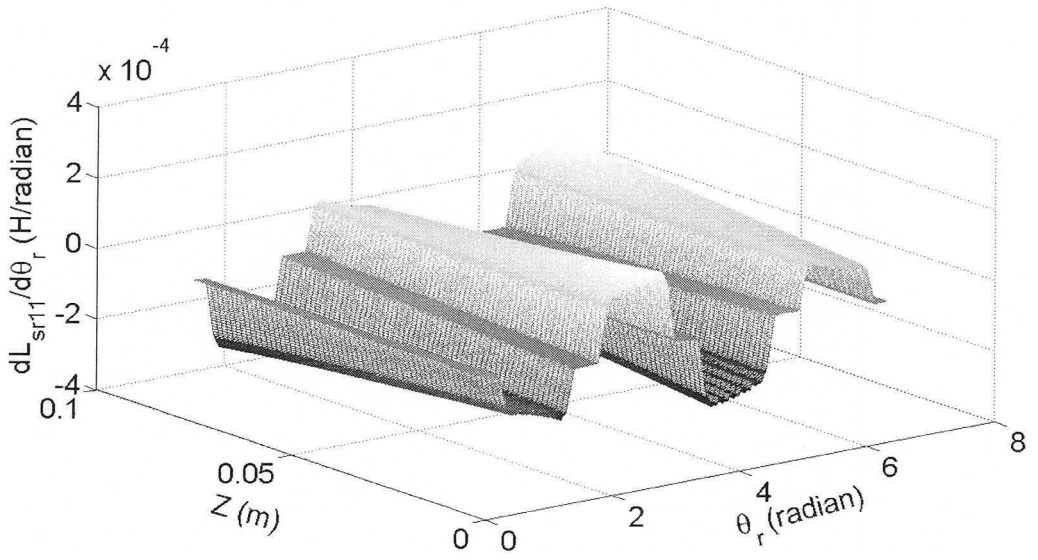
x 10^-4
4
2
0
-2
-4
dL_sr11/dθ_r (H/radian)
0.1
0.05
Z (m)
0
0
2
4
6
8
θ_r (radian)

(b)

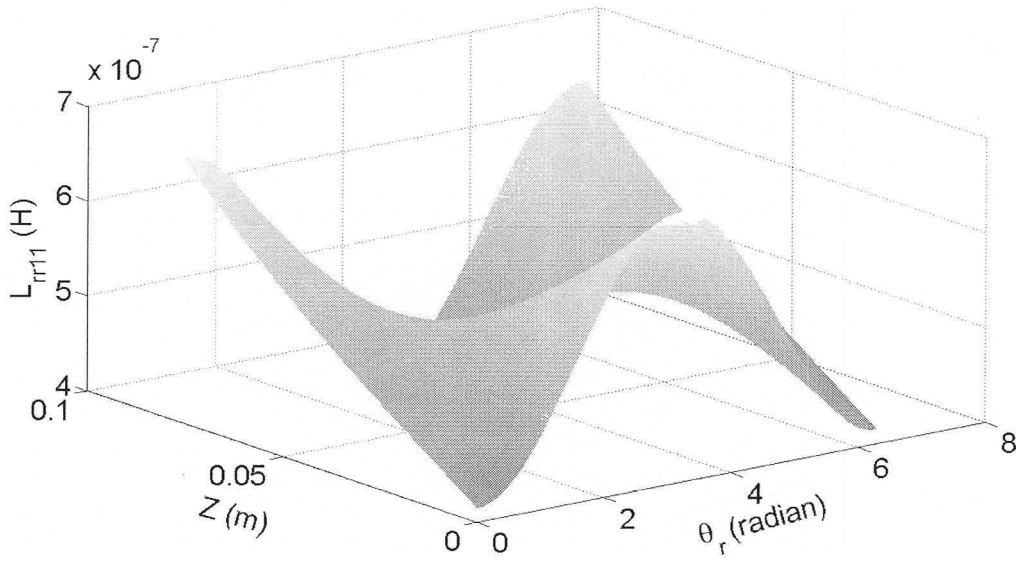

(c)

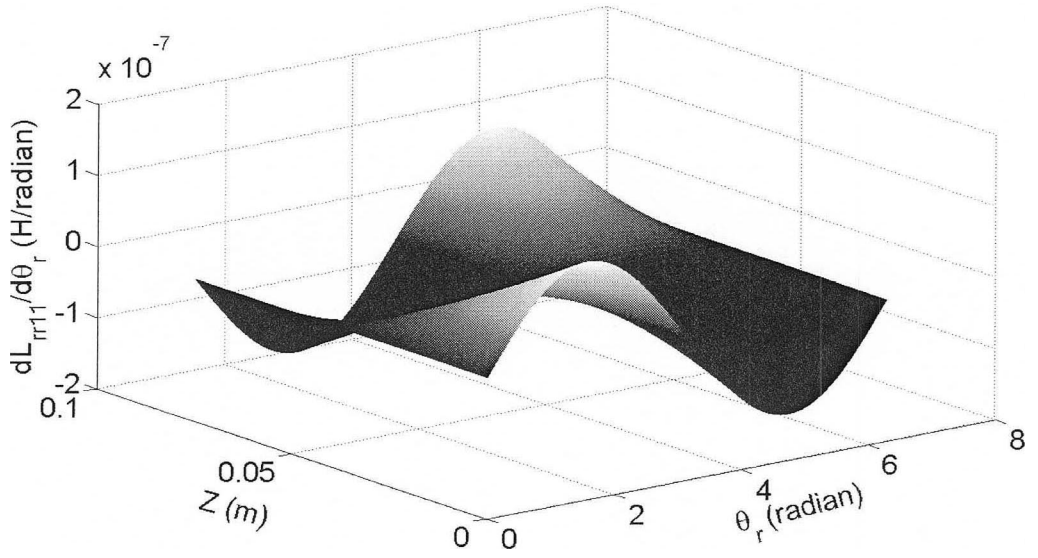

(d)

Figure 5.5 Variation of mutual inductances and their derivatives under inclined static eccentricity (one end 50% SE, the other end –50% SE), (a) L_{sra1}, between stator phase a and rotor loop 1; (b) $dL_{sra1}/d\theta_r$; (c) L_{rr11}, between rotor loop 1 and loop 1; (d) $dL_{rr11}/d\theta_r$.

5.3 Simulation Results for Detection of Inclined Static Eccentricity

Digital simulations of the 45-bar motor under different faulty conditions and load conditions have been done in MATLAB. From Fig. 5.6 to Fig. 5.11, stator current spectra are given respectively for the following 5 different conditions: (1) uniform 25% SE; (2) inclined static eccentricity with one end 0% SE, the other end 50% SE; (3) uniform 50% SE; (4) inclined static eccentricity with one end 40% SE, the other end 60% SE;(5) uniform air-gap; (6) inclined static eccentricity with one end –50% SE, the other end 50% SE. For each different condition, simulations were repeated at different load levels: (1) no load; (2) 25% load; (3) 50% load; (4) 75% load; (5) full load. Only results of full load case are given here. More plots for other load levels can be referred in Appendix C.

Compared with no-load operation, all background noise harmonics levels increased by almost 20dB under load condition, which definitely will make it difficult for detection of low degree eccentricity. For real application, this task can be more difficult due to the unbalanced load effect and environmental electric-magnetic noise [35].

According to the start-up performance of healthy and pure static eccentricity conditions (Fig. 5.6 (a) and Fig. 5.7 (a)), the acceleration time to attain steady speed apparently become longer for faulty condition. This delay can be attributed to the generation of reverse MMF due to eccentricity. The line current spectra show clearly eccentricity related harmonics predicted by (2.1) under faulty conditions. With 25% and 50% static eccentricity, the components of interest increase from –110dB (healthy) to –62.02 dB and –54.71 dB under no-load, respectively. However in case of inclined rotor, the diagnosis of fault related components is dependent on the inclination. From the calculation of inductance using MWFA, it could be seen that the inductance for inclined case actually is the average value of inductances along the shaft axis. For example, a motor with inclined rotor (one end 40% SE, the other end 60% SE) shall demonstrate characteristics of a motor with pure 50% static eccentricity. And the case of 25% pure SE should have similar harmonic with that of one end 0% SE, the other end 50% SE. Theoretically the fault related harmonics would be undetectable for the case in Fig. 5.11 (one end 50% SE, the other end –50% SE), since its average inductances are the same as

those of healthy case. Such a condition, therefore, cannot be detected by traditional MCSA. Hence this kind of situation needs special attention from the designers of online-monitoring systems. Different estimation techniques may be needed to extract fault signature. Other signals may have to be used for diagnosis, such as noise, bearing vibration and temperature, additional stress on bearing etc [5,6]. Table 5.1 shows the magnitude of fault related harmonics for all detectable cases. Obviously the magnitude of harmonics of interest increase with the severity of eccentricity. Also case 1 & 2, 3 & 4, 5 & 6 generated the harmonics of almost same amplitude under same load condition, which verified the analysis we mentioned before. The noise seen in the spectra is most probably due to noise generated through computations.

Table 5.1 Simulated, normalized amplitude of fault related harmonics under different faulty situations and load levels. (The fundamental (at 60 Hz) amplitude for all cases is 0 dB)

Load level	Amplitude of fault related harmonics for different SE degree (at two ends)					
	(1) 25%, 25%	(2) 0, 50%	(3) 50%, 50%	(4) 40%, 60%	(5) Healthy	(6) 50%, -50%
0%	-62.25 dB	-62.3 dB	-55.71 dB	-55.91 dB	-110 dB	-110 dB
25%	-61.4 dB	-59.27 dB	-53.39 dB	-53.88 dB	-85 dB	-90dB
50%	-59.95 dB	-58.93 dB	-52.43 dB	-52.55 dB	-85 dB	-85 dB
75%	-59.36 dB	-59.55 dB	-53.72 dB	-52.32 dB	-90 dB	-90 dB
100%	-58.73 dB	-59.17 dB	-53.41 dB	-53.09 dB	-90 dB	-87 dB

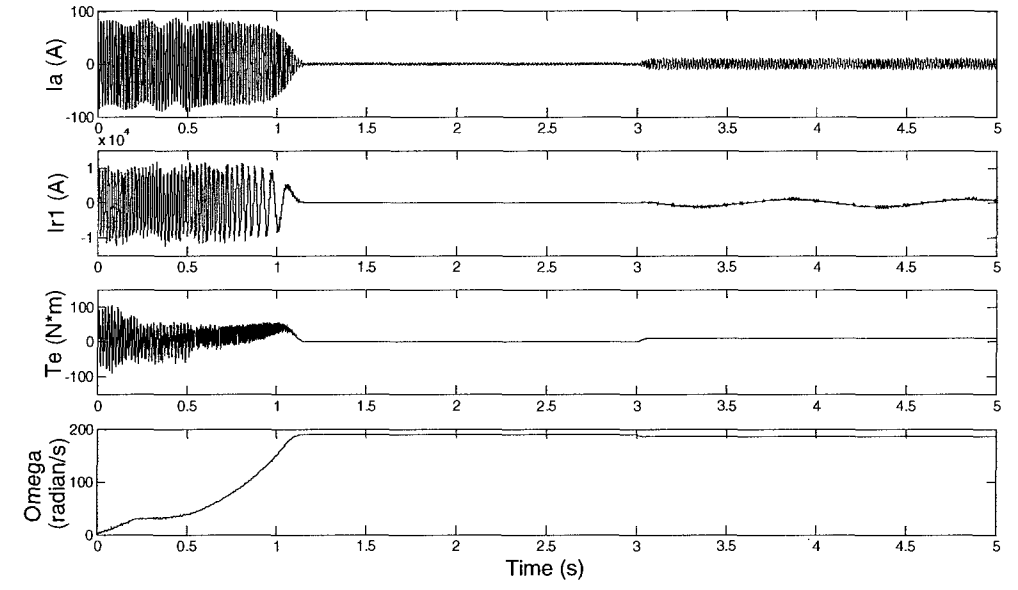

(a)

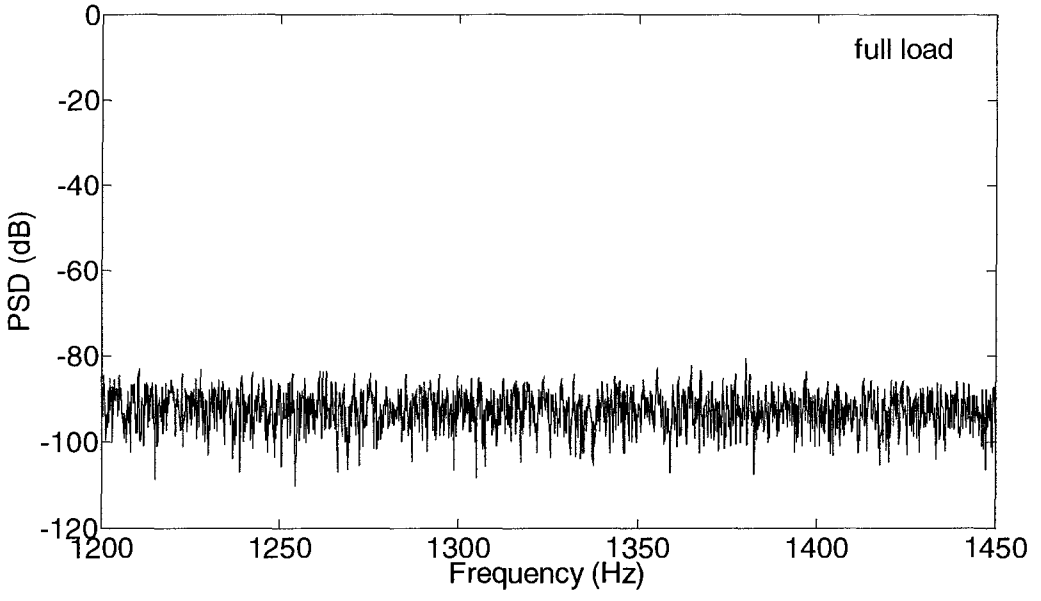

(b)

Figure 5.6 Simulation results under uniform air-gap (a) start-up characteristics, full load applied at 3 s; (b) normalized stator current spectrum with full load

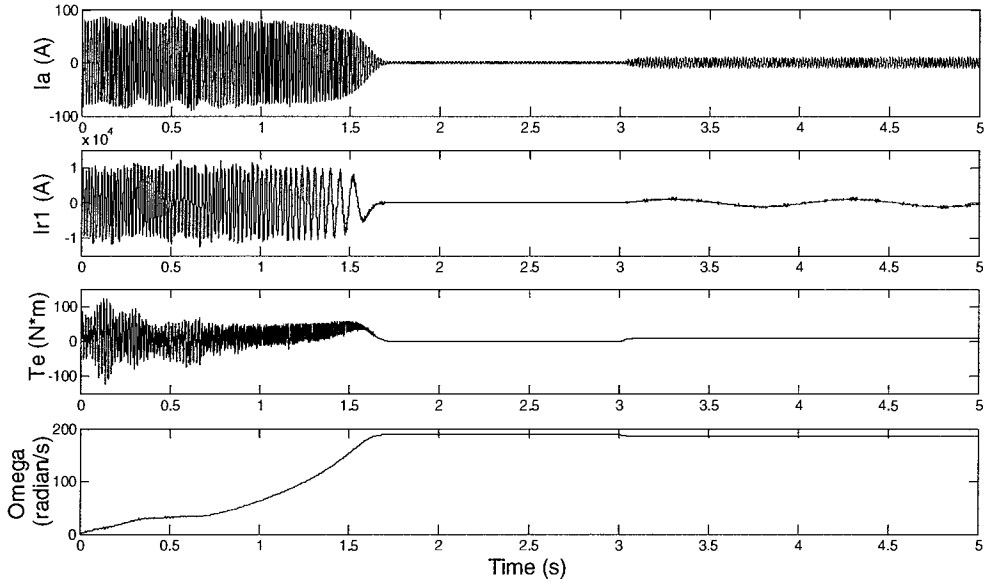

(a)

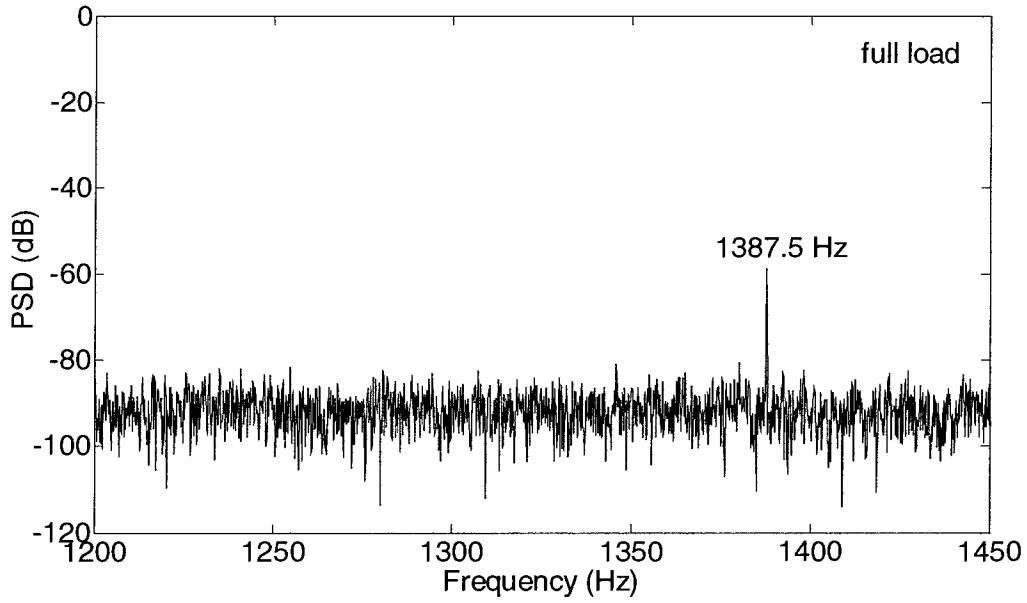

(b)

Figure 5.7 Simulated results under uniform 25% SE (a) start-up characteristics, full load applied at 3s; (b) normalized stator current spectrum with full load

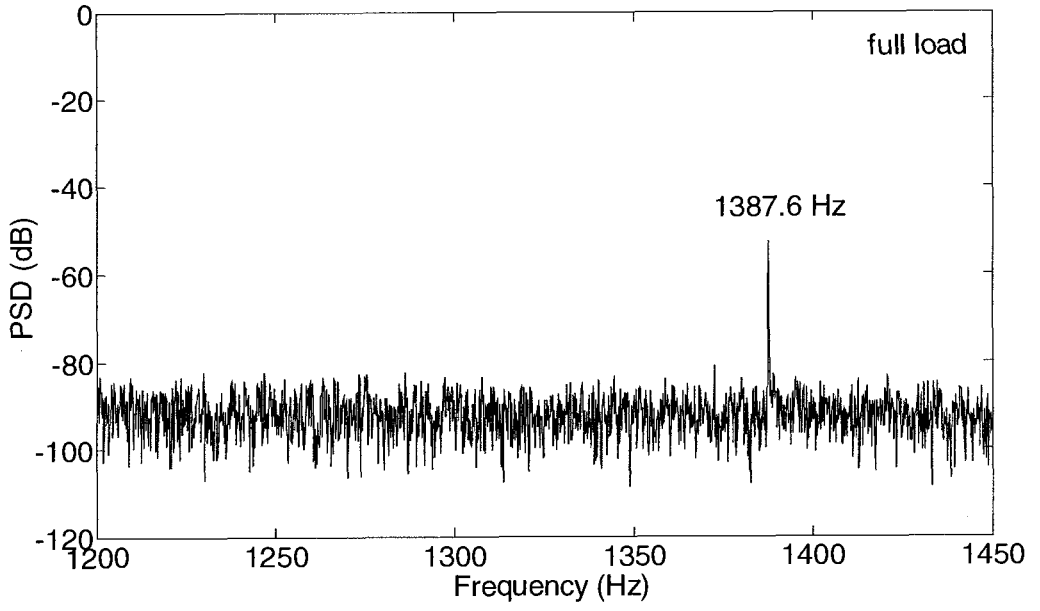

Figure 5.8 Simulated, normalized stator current spectrum with uniform 50% SE under full load

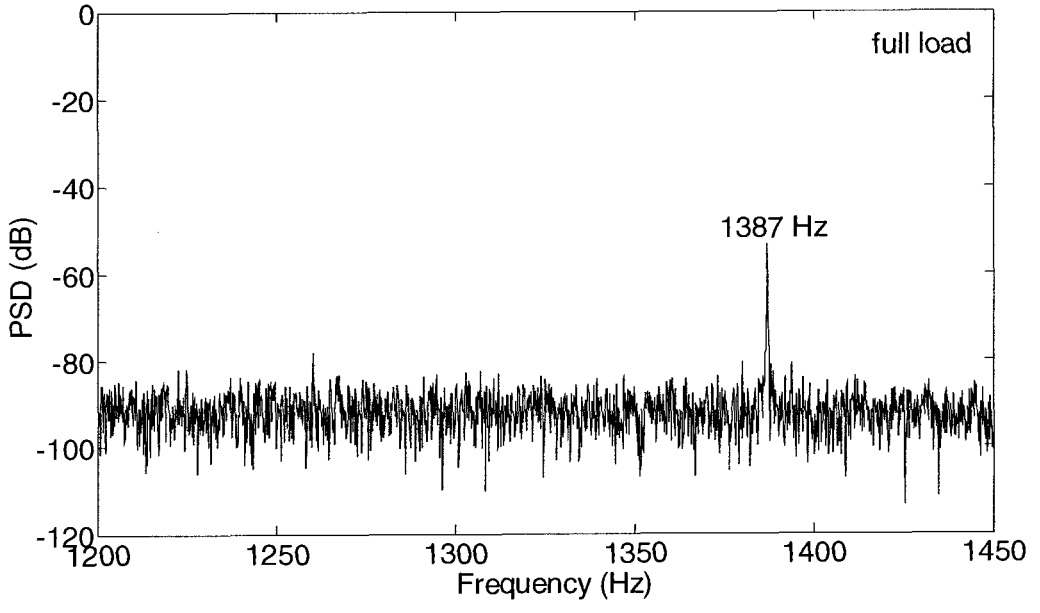

Figure 5.9 Simulated, normalized stator current spectrum with inclined rotor (one end 40% SE, the other end 60% SE) under full load

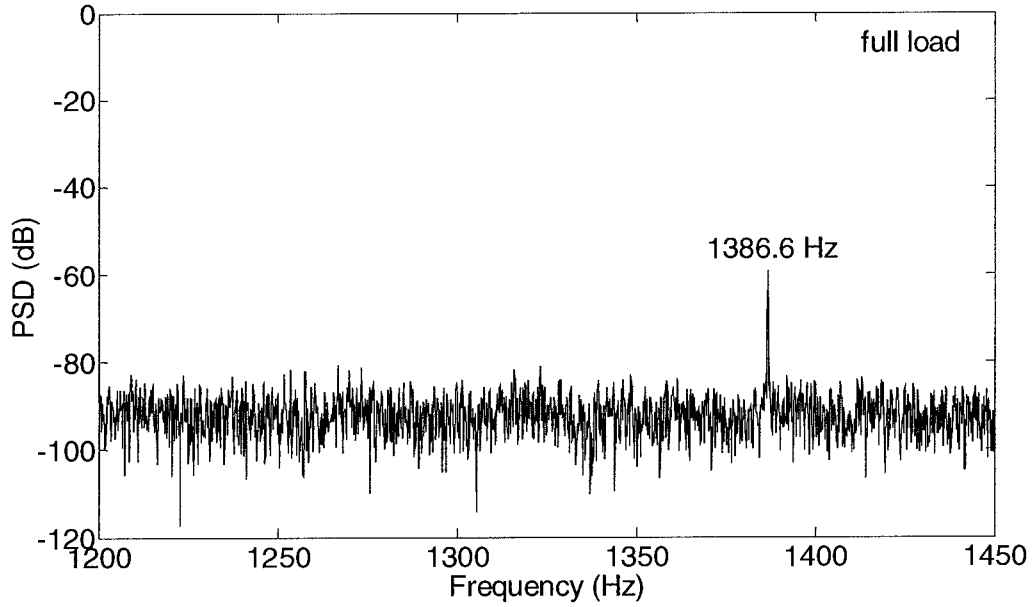

Figure 5.10 Simulated, normalized stator current spectrum with inclined rotor (one end 0% SE, the other end 50% SE) under full load

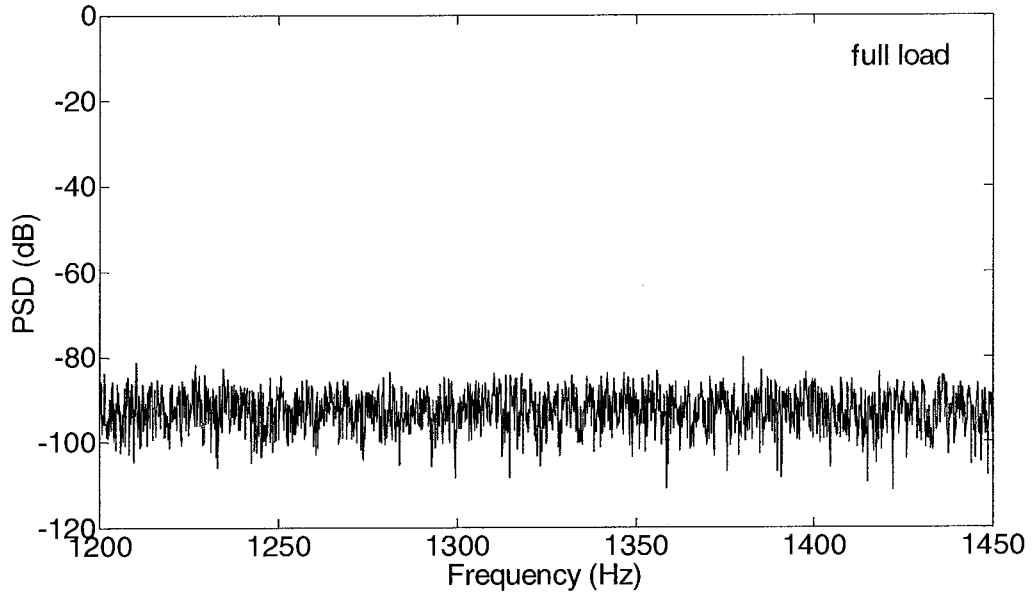

Figure 5.11 Simulated, normalized stator current spectrum with inclined rotor (one end 50% SE, the other end -50% SE) under full load

5.4 Conclusions

A four-pole, 2 kW cage induction motor with 45 rotor bars is simulated under different faulty conditions and at different load levels. The plots of inductances for different eccentric conditions are given. The motor starts up without load and then different level of loads are applied to it after steady speed is reached. The spectra of steady state line current show the existence of the fault related components. The important finding is that the inclined static eccentricity cases demonstrate similar harmonics of pure SE. The amplitude of the harmonics is proportional to the average eccentricity ratio. In the next chapter, Finite Element method to calculate motor inductances is discussed and results are compared with those obtained in this chapter using MATLAB [31].

Chapter 6
Evaluation of Motor Inductances with Finite Element Method

6.1 Introduction

As we know, the accuracy of inductance calculation is key to the validity of the simulation results. Thus, in order to verify the inductance profiles obtained by MWFA techniques, a Finite Element based software — Maxwell 2D [36] is used to evaluate inductances. Since that Finite Element method deals with the calculation by directly analyzing the magnetic field, the calculation will consider all factors of saturation, slots effects and the results shall be more accurate.

6.2 Simulation Results of Finite Element Method

It is well known that the definition of inductance for a coil is the flux linkage per ampere linked to the coil. Thus, for a coil a, the magnetizing inductance L_{aa} and mutual inductance L_{ab} can be obtained by the following equations:

$$L_{aa} = \frac{N_a \Phi_{aa}}{i_a} \tag{6.1}$$

$$L_{ab} = \frac{N_a \Phi_{ab}}{i_b} \tag{6.2}$$

where N_a is the turn's number of coil a, Φ_{aa}, Φ_{ab} are the flux linkage in coil a due to i_a and i_b respectively, i_a and i_b are currents flowing coil a & b respectively.

To use Maxwell 2D for inductance calculations, the detail of the motor's geometry including slot and bar shapes is needed to draw a precise cross-sectional diagram of the motor. This software applies Finite Element method to analyze the magnetic field generated by assigned sources, and then the desired flux linkage and inductance are evaluated. For example, the mutual inductance between stator and rotor can be obtained through the flux linkage of one rotor loop due to the current source assigned to one stator phase winding.

The stator magnetizing inductance and mutual inductance are always rotor position independent even under inclined static eccentricity, because the relative position between stator windings and maximum or minimum air-gap is fixed in space. The stator magnetizing inductances, mutual inductances obtained from two different ways are given in Table 6.1 for comparison. Here only values from phase *a* are shown since other phases' values shall be the similar to phase *a*. The relative difference between two methods is around 9-20%. This is due to the saturation (tooth, yoke etc.) and finite permeance of the magnetic material used for FE simulation. WFA & MWFA, as mentioned earlier, assume infinite permeance for magnetic material. Also slot effects are neglected in WFA and MWFA.

Table 6.1 Comparison of stator magnetizing inductance, mutual inductance obtained from MWFA and Finite-Element

	L_{aa} (healthy)	L_{ab} (healthy)	L_{aa} (25%SE)	L_{ab} (25%SE)	L_{aa} (50%SE)	L_{ab} (50%SE)
Finite Element	0.13759	0.06821	0.14076	0.069338	0.14978	0.07442
MWFA	0.1561	0.078205	0.1612	0.08077	0.1802	0.0903

Fig. 6.1 shows the plots of mutual inductance between rotor loop 1 and stator phase *a, b, c* using MWFA (left) and Finite Element (right) individually. It is shown that they match each other very well except the magnitudes for both healthy and eccentric situation. The rotor bars' self- and mutual inductances are illustrated in Fig. 6.2. Possibly the rotor loop leakage flux makes the rotor loop magnetizing inductance results in Maxwell higher than that of MWFA. This could be due to the fact that other rotor bars are not energized and hence flux coming out of one bar can easily escape from the side of the loop and not linking the second bar. And the existence of ripples on the curves reflects the effect of slot opening/tooth saturation on flux linkage, while the curves got from MWFA are smooth since those neglect slot effects. The changing trend of mutual inductance L_{sr} with respect to axial length, for inclined rotor condition, is given in Fig. 6.3. With Maxwell 2D the flux distribution can also be observed (Fig. 6.4). The increased flux density (hence increased saturation) around the position of the maximum air-gap and the decreased flux density around the minimum air-gap can be clearly identified.

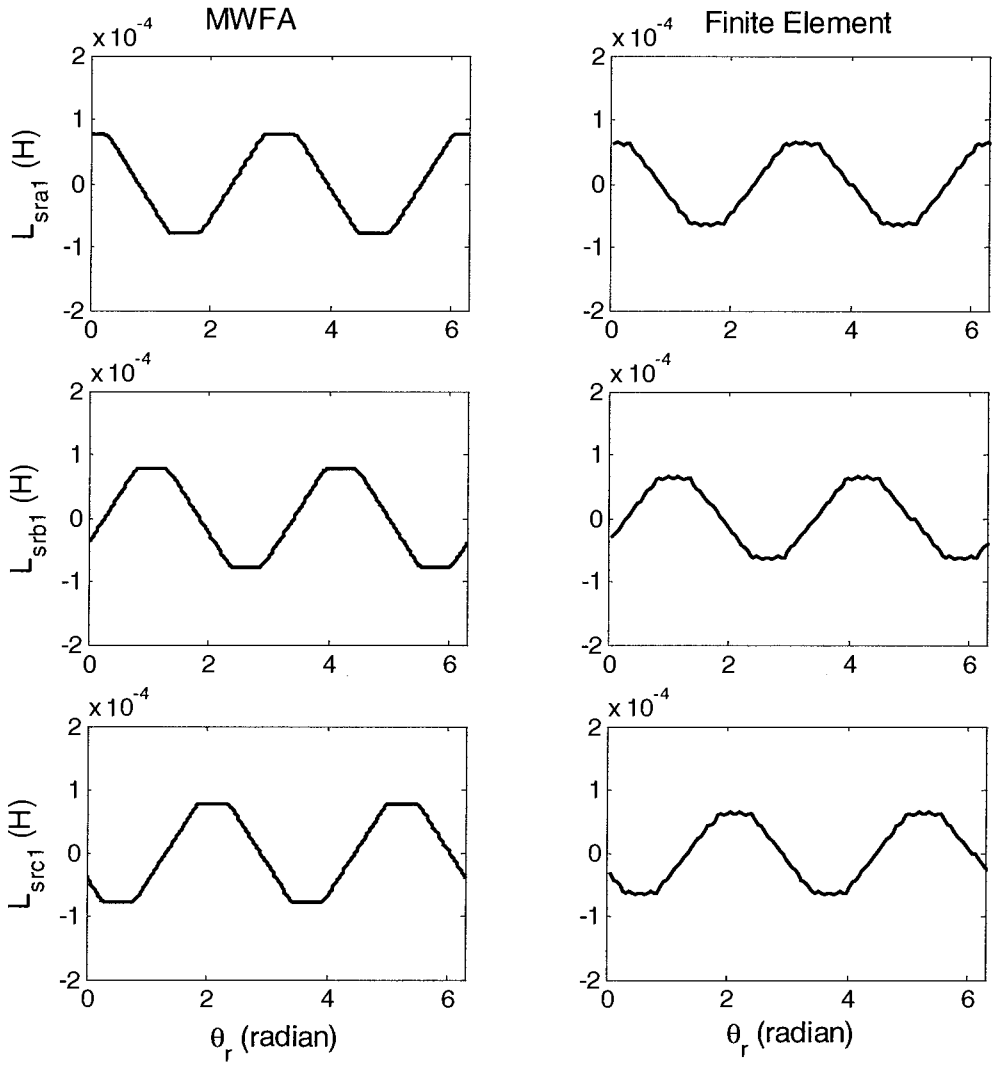
MWFA
Finite Element
x 10^-4
L_sra1 (H)
L_srb1 (H)
L_src1 (H)
θ_r (radian)
θ_r (radian)

(a)

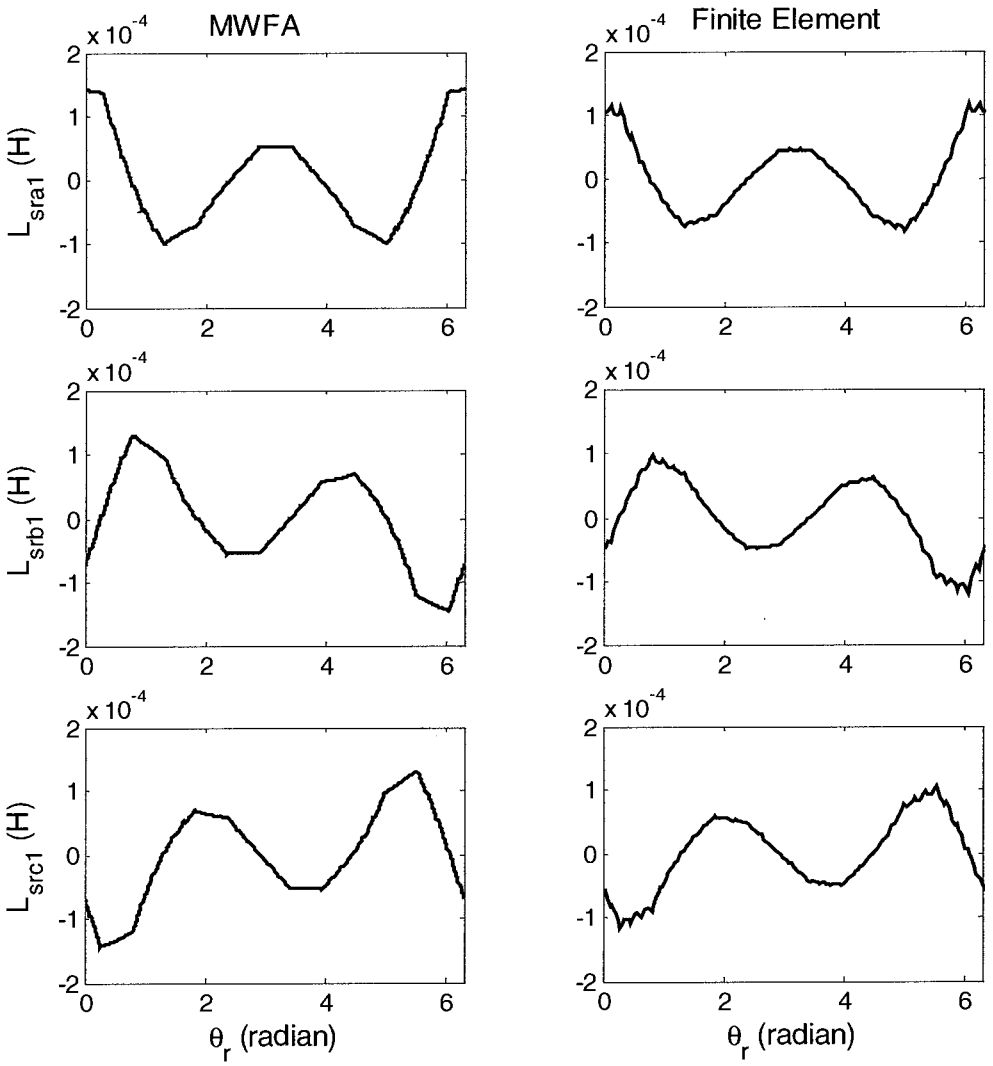

(b)

Figure 6.1 Comparison of mutual inductances obtained by MWFA (left) and Finite-Element (right), from top to bottom are mutual inductance between rotor loop 1 and stator phase *a*, *b*, *c* respectively;(a) healthy machine, (b) under uniform 50% SE.

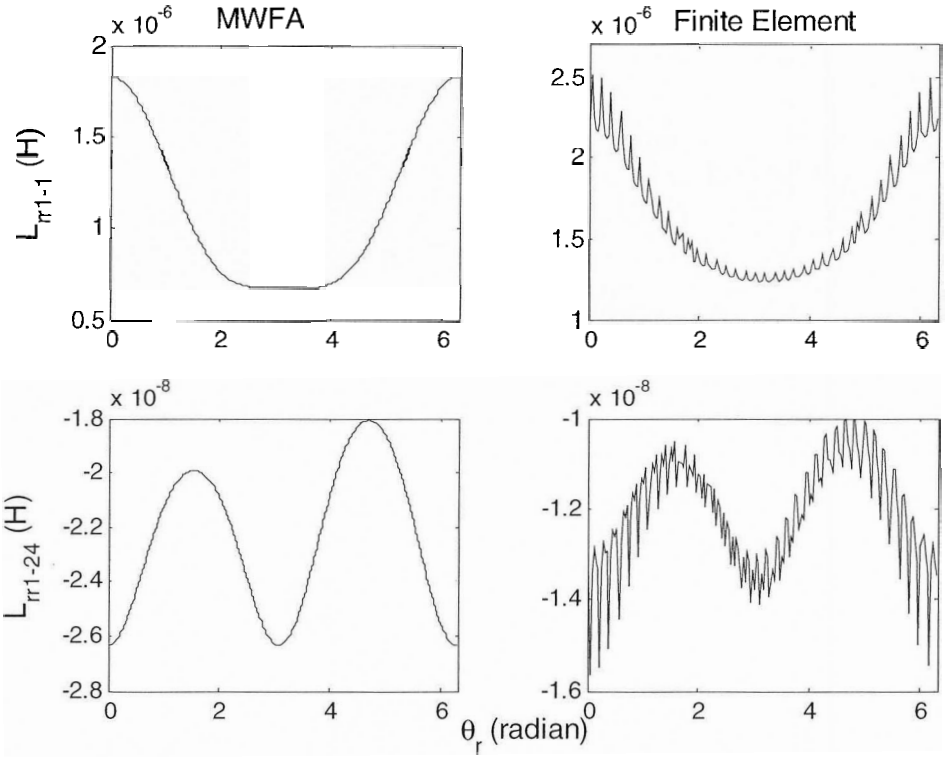

Figure 6.2 Comparison of rotor loops self and mutual inductances obtained by MWFA (left) and Finite-Element (right), from top to bottom are self-inductance of rotor loop 1, mutual inductance between rotor loop 1 and 24 under uniform 50% SE

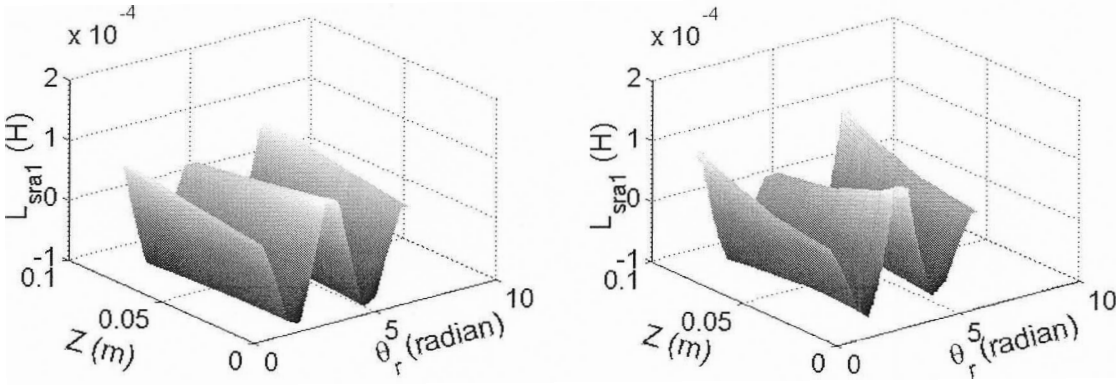

Figure 6.3 Variation of mutual inductance L_{sra1} between stator phase *a* and rotor loop 1 obtained from MWFA (left) and Finite Element method (right) for one end 50%SE, the other end –50%SE.

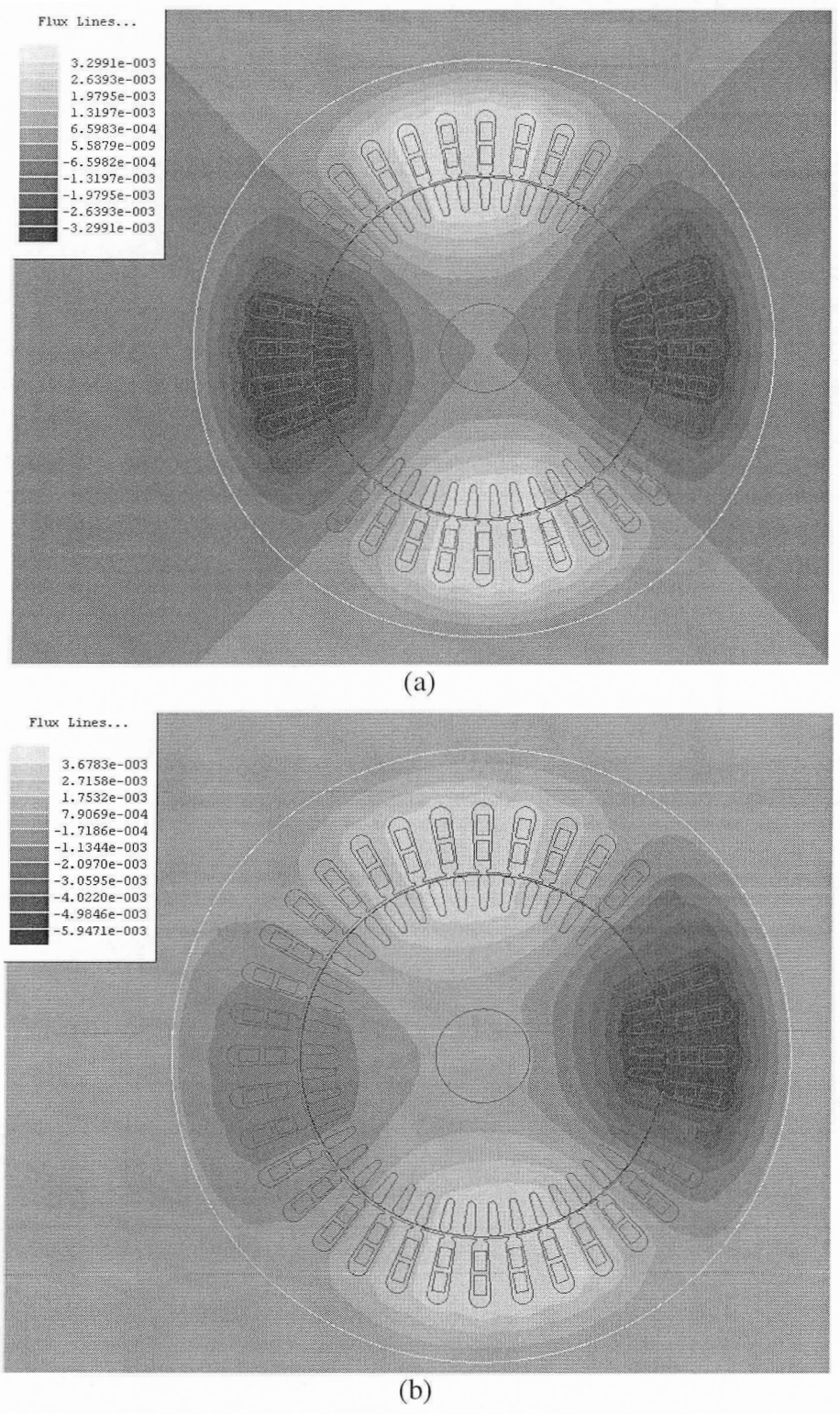

Figure 6.4 Flux distribution of the experimental motor with one stator phase excited for (a) healthy condition and (b) uniform 50% SE condition.

6.3 Conclusions

Using Finite-Element based software Maxwell 2D, the motor inductances are evaluated. Compared with the results obtained by WFA & MWFA, most of the values show satisfactory matches except rotor bar loops self and mutual inductances. The main advantage of using FE is its high accuracy due to inclusion of slot effects. However the influence of slot effects may not be important according to [27]. Core saturation can be incorporated in WFA & MWFA also by using Carter's coefficient. But MWFA can take rotor bar skewing into consideration, which has large impact on eccentricity harmonics. Maxwell 2D cannot include skewing since the simulation is limited to 2-D. Also it is easy to isolate different factors such as slot effects, saturation in MWFA to evaluate the effect of each of them, which cannot be realized in FE. Additionally the time for FE simulation is extremely large compared with MWFA. For example, FE takes almost 8 hours to calculate the mutual inductance between stator phase and rotor loop at the resolution of 2°(from 0° to 360°, 181 points) on a Pentium IV based PC working at 2.4 GHz, with 512 MB RAM, while MFWA written in MATLAB codes running on the same platform only needs approximately 30 minutes to simulate 10 seconds of run time of the complete machine connected to a standard 60 Hz AC source. Finally, since modeling is only a theoretical tool to simulate a real machine, it can never replace a real machine in scientific research. Thus, although the accuracy of MWFA is not as good as Finite-Element, it is still chosen as an appropriate method due to its advantages with computation time and flexibilities without losing too much accuracy to detect fault related harmonics in steady state. In the following chapter, several experiments are performed to substantiate simulation results.

Chapter 7

Experimental Results of an Induction Motor with Inclined Eccentricity

7.1 Introduction

In order to validate the simulation results and theoretical analysis we have made before, a series of experiments were carried out on the same 45 bar induction motor simulated in Chapter 5, whose specification can be found in the Appendix A. The experimental scheme is shown in Fig. 7.1.

For sake of reasonable comparison, the experiments are repeated under different faulty conditions and load levels similar to MATLAB simulations. The steady state line current signals are sensed by a current probe and then fed into a signal analyzer. The resulting plots are then compared with simulated current spectrum for validation.

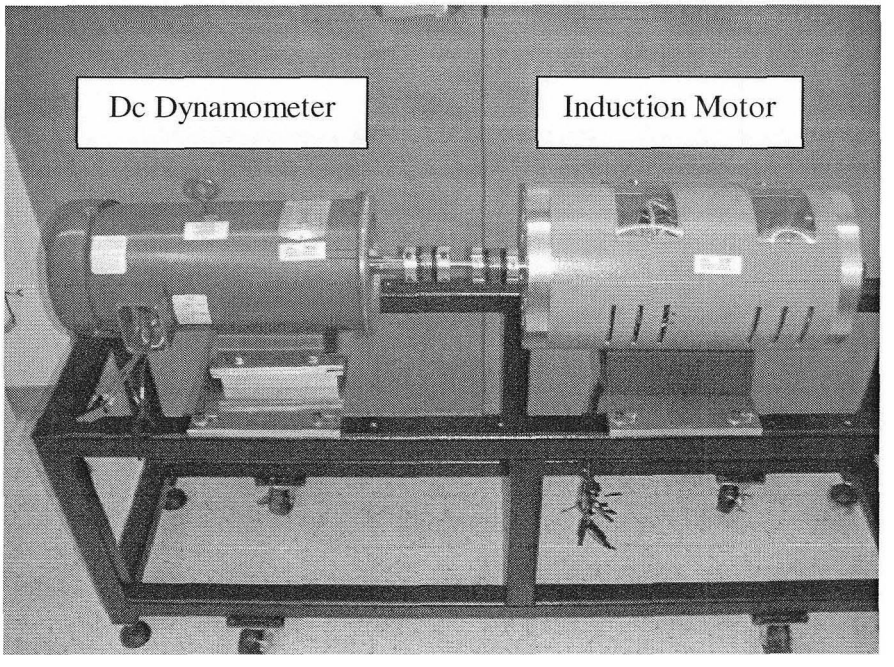

Figure 7.1 Experimental Setup

7.2 Experiment Method and Results

In Fig. 7.1, it can be seen that the induction motor on the right is coupled with a separately exited dc generator. A group of resistances are connected to the armature winding of the dc generator as load (dynamometer). The output voltage of generator is kept at 120V by adjusting its field winding, thus different output load level can be achieved through changing the load resistances. The corresponding resistance values to different load level are 7.5Ω (full-load), 10 Ω (75% load), 15 Ω (half-load), 30 Ω (25% load) respectively.

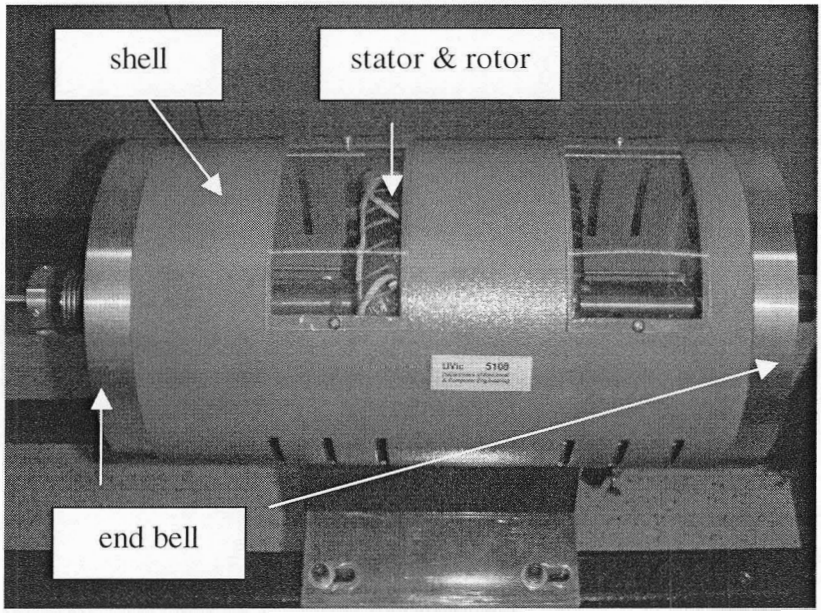

(a)

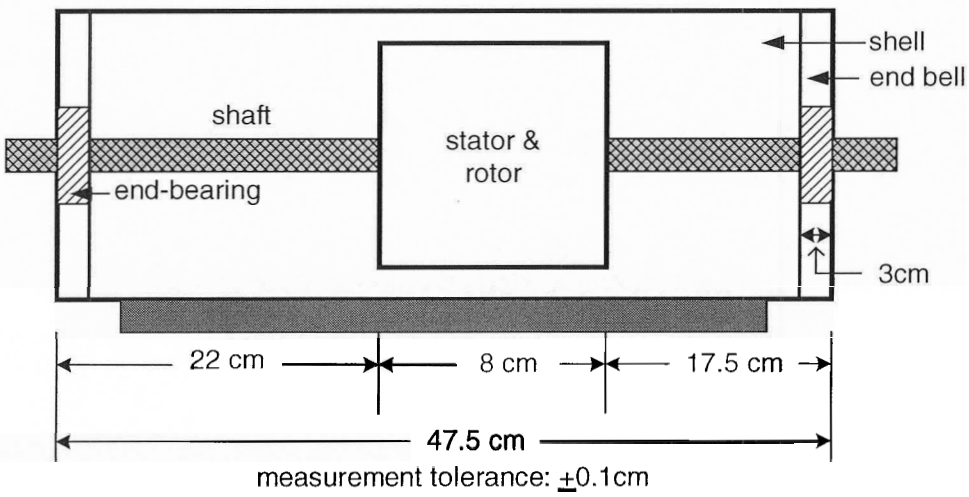

(b)

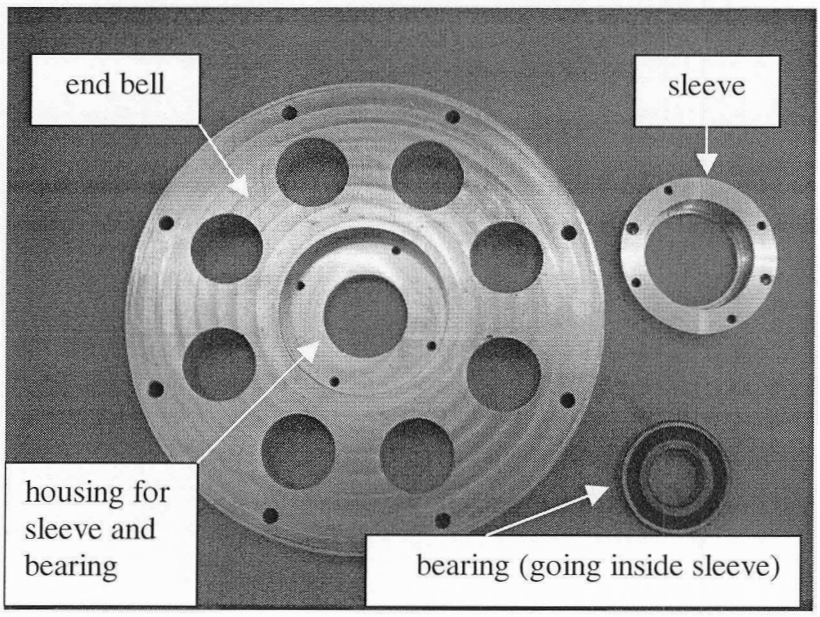

(c)

Figure 7.2 The experimental induction machine (a) actual motor; (b) schematic diagram of motor; (c) end bell, the eccentric sleeve and bearing

The two end-bells of motor are custom made to add two sleeves with the bearings (Fig. 7.2(c)). The sleeves are fabricated eccentric so that different shaft incline levels can be generated. One of the original bearings is replaced with a self-aligning bearing, to accommodate the change in axial length due to inclined eccentricity. Although accurate eccentricity ratio at two end-bearings could be obtained by strict control of fabrication tolerance, exact eccentricity ratios at the ends of stator winding are difficult to achieve. However, the available average eccentricity degrees we have in experiment are comparable to the simulation cases. The actual eccentricity was measured using a filler gauge. For example, the average eccentricity ratio of 22.89% & 32.53% case is 27.71%, which is close to 25% for 0 & 50% case in simulation. Similarly, 45.78% & 65.06% case is close to 40 & 60% case in simulation. Totally 5 different healthy or unhealthy cases were tested, and each case was repeated under different load levels.

By examining the current spectra obtain through a signal analyzer, one could identify the expected harmonics. Due to unavoidable inherent static eccentricity, the healthy case spectra also generate the components of interest. According to the analysis in Chapter 2, this 45-bar machine should only generate strong harmonic of interest associated with 23 pole-pairs under faulty conditions. However, it is noted that the lower harmonics

attributed to 21 pole pairs, a multiple of three, shows significant amplitude too in Figs. 7.4-7.8. This phenomenon actually results from the unbalance of power supply and manufacturing asymmetry. The unbalance results in a reverse rotating field, which interacts with the distorted permeance of the machine to generate the component. This can be proved by simulation of this motor under static eccentricity and one phase voltage source with 10% unbalance, as shown in Fig. 7.3. The theoretical proof can be obtained based on [37].

The experimental results of amplitude of interested harmonics are given in Table 7.1 & 7.2, respectively, for higher and lower harmonics. In healthy case, the eccentricity related harmonics is also noticeable, which is attributed to unavoidable inherent static eccentricity. Compared with healthy condition, the amplitude of eccentricity-related harmonics increased considerably under faulty cases; while the change of amplitude for the other one is limited. It appears that there can be some other cause for production of that harmonic. In fact, the amplitude of the harmonics due to unbalance even decreased in the 22.89% & 32.53% faulty case. Thus the asymmetry based eccentricity component should not be used for detection of eccentricity fault. It is noted that different inclined conditions with similar average eccentricity do generate almost same amplitude of harmonics of interest in the experiment. Especially, as predicted, the current spectrum of symmetric incline case (50% & -50%) looks almost same as the healthy case. The variation of the amplitude of eccentricity related harmonics under different load level is presented in Fig. 7.9, which is also compared with simulated results. Although there is no clear relationship between load level and the amplitude of the featured harmonic, it is observed that cases with similar average eccentricity ratio demonstrate similar changing trend with different load levels in both experiments and simulations. The differences of magnitude between experimental curves and simulation curves could be attributed to non-ideal factors in experiments, such as, supply unbalance, time harmonics, saturation, the alignment of the coupling between two machines, assembly tolerance of the end-bells, the vibration of the test bed and so on. Especially for the case of average eccentricity ratio near zero, the difference is relatively large, which probably resulted from the unavoidable SE and slot effects in experimental machine. Fig. 7.10 illustrates the variation of the eccentricity related harmonics with the average eccentricity severity under different load

levels for experimental and simulated results. The similarity in trend between the experimental and simulation results are quite apparent.

Table 7.1 Experimental, normalized amplitude of eccentricity related harmonics under different faulty situations and load levels. (The fundamental (at 60 Hz) amplitude for all cases is 0 dB)

Load level	Amplitude of eccentricity related harmonics for inclined condition				
	22.89%, 32.53%	50%, 50%	45.78%, 65.06%	Healthy	50%, -50%
0%	-55.43 dB	-49.26 dB	-50.74 dB	-61.01 dB	-62.7 dB
25%	-52.65 dB	-48.97 dB	-49.55 dB	-64.6 dB	-61.08dB
50%	-53.5 dB	-47.22 dB	-48.27 dB	-63.8 dB	-61.24 dB
75%	-53.2 dB	-46.9 dB	-47.38 dB	-62.42 dB	-61.7 dB
100%	-53.6 dB	-46.88 dB	-47.28 dB	-62.04 dB	-61.9 dB

Table 7.2 Experimental, normalized amplitude of unbalanced supply related harmonics under different faulty situations and load levels. (The fundamental (at 60 Hz) amplitude for all cases is 0 dB)

Load level	Amplitude of asymmetry related harmonics for different inclined condition				
	22.89%, 32.53%	50%, 50%	45.78%, 65.06%	Healthy	50%, -50%
0%	-58.03 dB	-51.3 dB	-52.2 dB	-55.94 dB	-57.45 dB
25%	-61.1 dB	-53.7 dB	-55.4 dB	-56.54 dB	-56.6 dB
50%	-61.2 dB	-55.2 dB	-58.9 dB	-59.4 dB	-58.55 dB
75%	-59.8 dB	-55.9 dB	-57.38 dB	-59.6 dB	-59.2 dB
100%	-60.1 dB	-55.8 dB	-57.28 dB	-60.2 dB	-59.25 dB

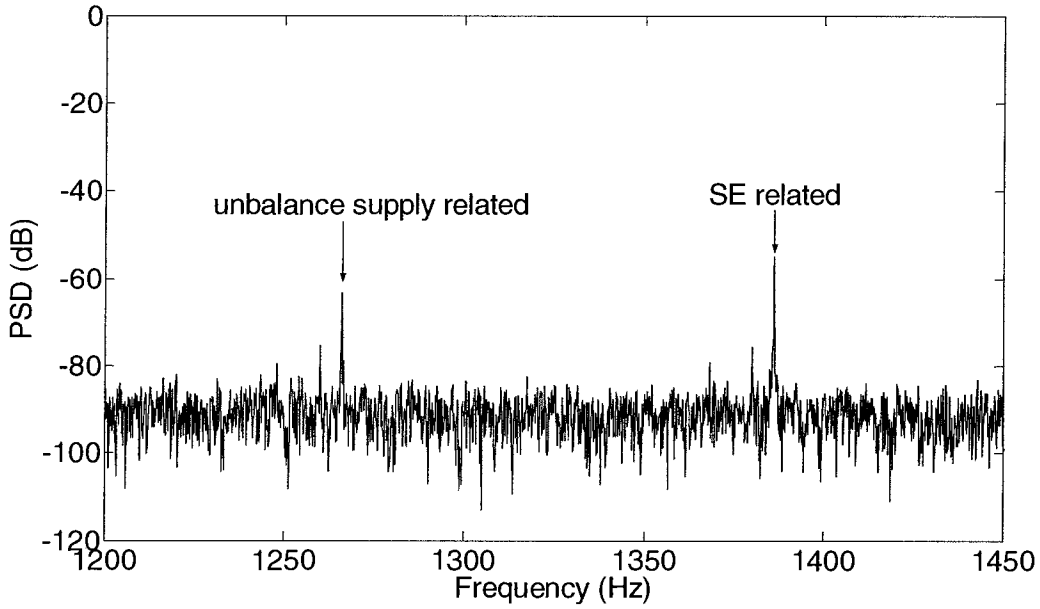

Figure 7.3 Simulated, normalized line current spectrum with 10% unbalance in supply voltage under uniform 50% SE

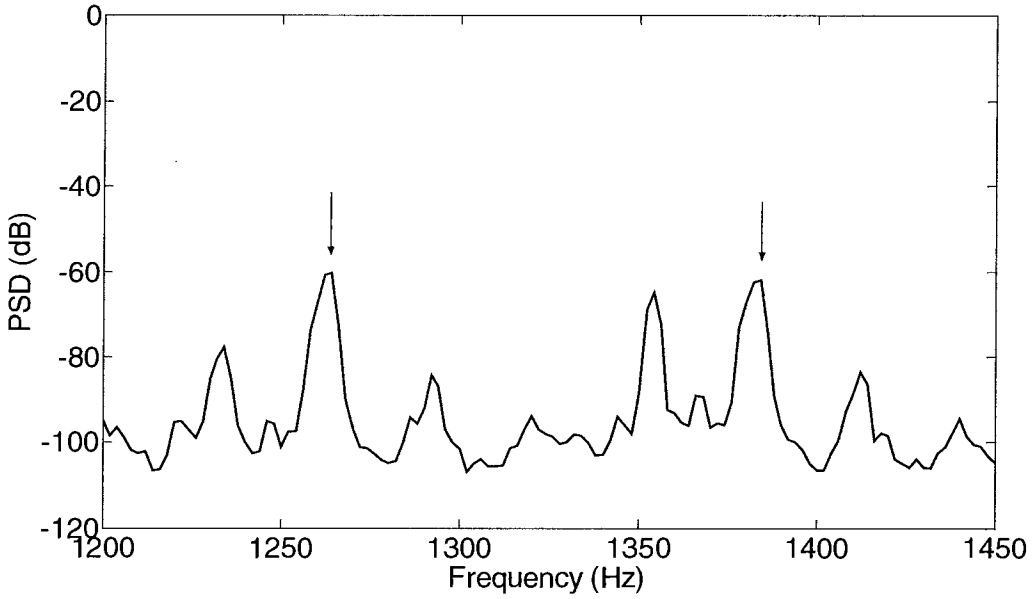

Figure 7.4 Experimental, normalized spectrum of line current for healthy case under full load

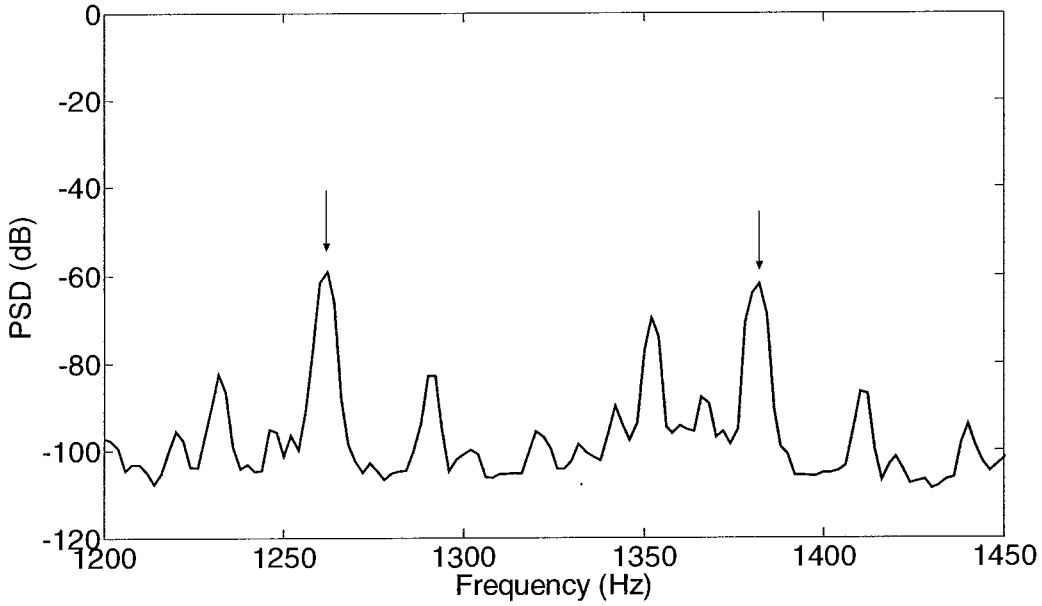

Figure 7.5 Experimental, normalized spectrum of line current with inclined rotor (one end 50% SE, the other end -50% SE) under full load

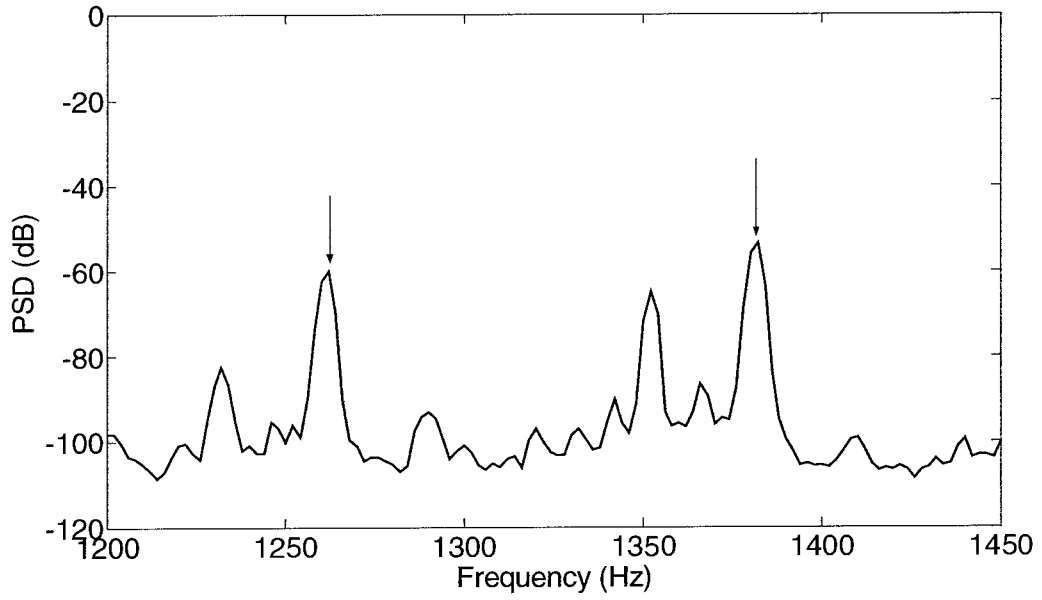

Figure 7.6 Experimental, normalized spectrum of line current with inclined rotor (one end 22.89% SE, the other end 32.53% SE) under full load

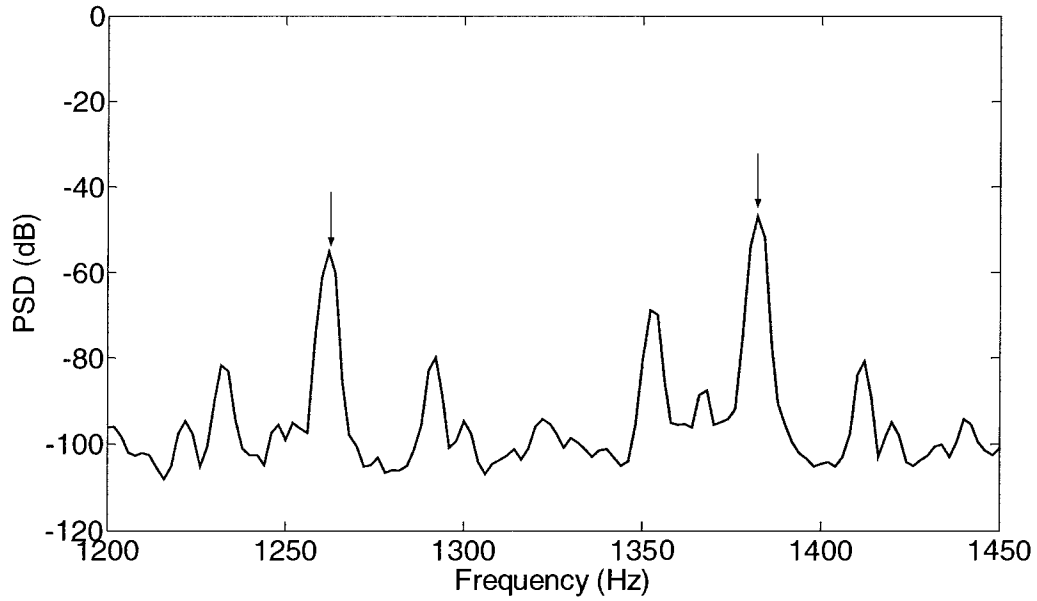

Figure 7.7 Experimental, normalized spectrum of line current with uniform 50% SE under full load

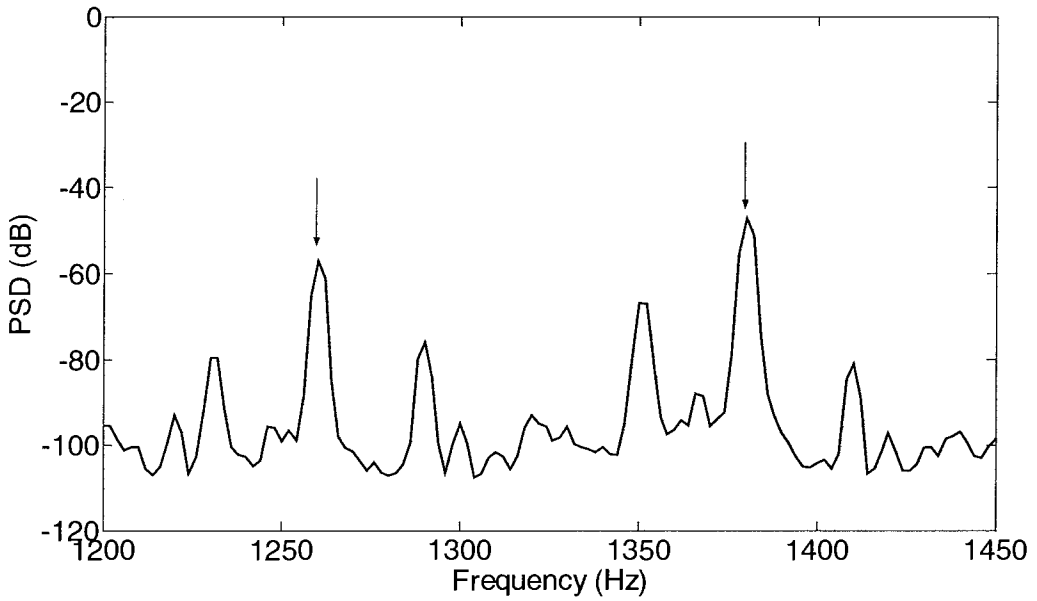

(e)

Figure 7.8 Experimental, normalized spectrum of line current with inclined rotor (one end 45.78% SE, the other end 65.06% SE) under full load

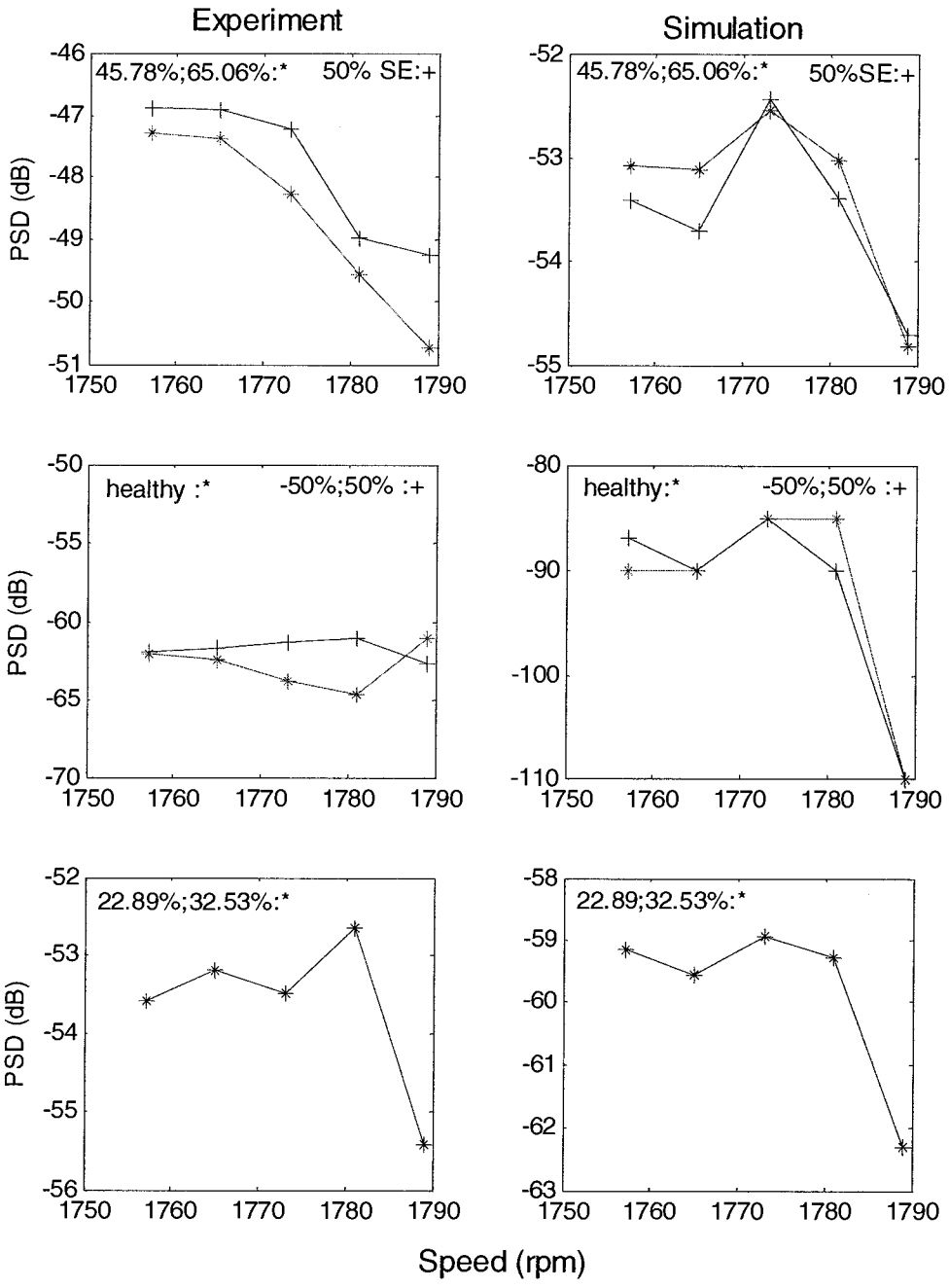

Figure 7.9 Variation of the amplitude of eccentricity related components under different load levels. Left: experimental results; Right: simulated results. From top to bottom, the average eccentricity are around 50%, 0, 25%.

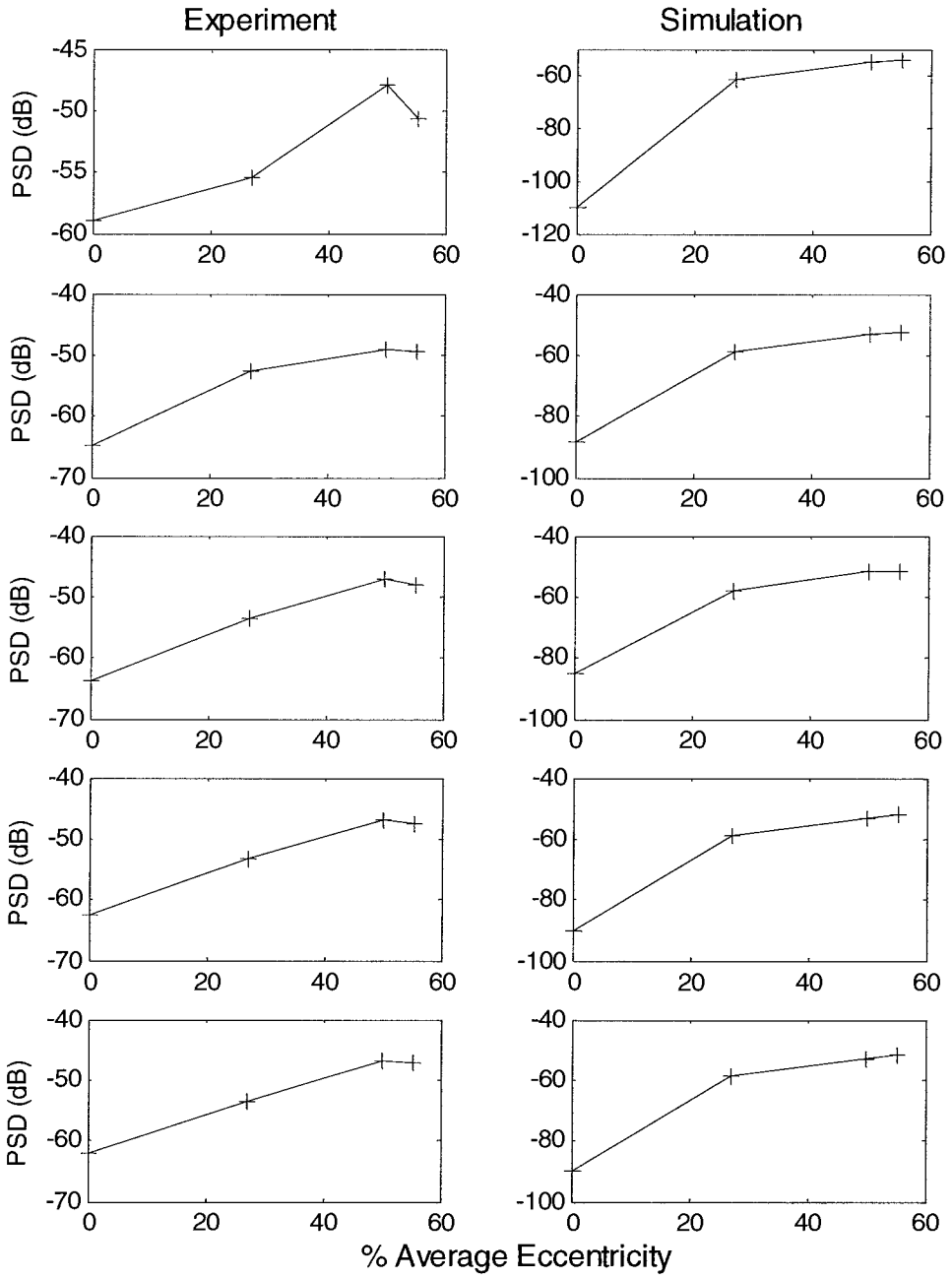

Figure 7.10 Variation of the amplitude of eccentricity related harmonics with the average eccentricity severity under different load levels for experiment (left) and simulation (right). The test points are healthy, 22.89% & 32.53%, uniform 50%, 45.78% & 65.06%. From top to bottom, the load levels are: no-load, 25% load, 50% load, 75% load, full-load.

7.3 Conclusions

A series of experiments have been conducted on a machine similar to the simulated 45 bar motor to validate the theoretical analysis. Compared with simulated current spectra, more spectral lines showed up. This is expected because of time harmonics, supply unbalance, local and non-uniform saturation and other non-idealities arising out of the machine construction. Changes in the amplitude of two particular harmonics are monitored while load and eccentricity levels are changed. Due to unavoidable inherent static eccentricity, they are detectable even under healthy condition. One of these harmonics is due to the combination of inherent SE, machine asymmetry and supply unbalance. Experimental results show that this harmonic is a less reliable indicator of the degree of eccentricity than the other one. Loading doesn't seem to have much effect on either of them. However, the eccentricity related components could still be detected successfully and distinguished from other components. Through comparisons of cases with different fault severity, it was shown that inclined static eccentricity cases demonstrate similar harmonics of pure SE and the amplitude of the harmonics is dependent on the average eccentricity ratio located at the middle point of the rotor shaft. This might lead to failure in detection of eccentricity as was demonstrated by the –50% & 50% case. The experimental results thus matched the conclusions drawn from the simulation results.

Chapter 8

Conclusions and Future Work

8.1 Conclusions

Detection of inclined static eccentricity fault due to axially unequal air-gap is discussed in this thesis. The signature of the inclined static eccentricity is predicted and then substantiated by computer simulation and experiment. The generation of eccentricity related current harmonics is shown to be affected by several factors, such as the number of pole pairs, the number of rotor bars, the severity of eccentricity, the rotor inclined angle and so on.

The model of the motor is constructed based on coupled magnetic circuit approach and improvement of simulation efficiency is achieved by reducing the variables by one. Modified Winding Function Approach (MWFA) is used to calculate the machine inductances. Since the air-gap changes along both axial and radial direction, the original MWFA is extended to 3-D space. The new version of MWFA is capable of incorporating different kinds of winding distribution and non-uniform air-gap. Finite Element method is introduced to verify the inductance values obtained by using MWFA.

Different healthy and unhealthy cases are tested in simulation using MATLAB and experiments. Comparisons are made among the results. It is revealed that the inclined motor with a certain amount of average eccentricity shows similar amplitude of harmonics as the one with same degree of pure static eccentricity.

To summarize, the contributions arising out of the work presented in this thesis are:

- Computation of inductances under inclined static eccentricity conditions.
- Simulations of machine with inclined static eccentricity.
- Experiments of machine with inclined static eccentricity.
- Shown (using both simulation and experiments) a condition where eccentricity may not be detectable.

8.2 Future Works

Based on the results, a motor with appreciable rotor inclination may not show eccentricity related harmonics in line current spectrum if the average eccentricity is really small. However, without early detection such a fault will definitely cause strong stress and friction on end bearings, which may finally result in broken part and breakdown of the machine. The investigation of bearing vibration, temperature might be a good alternative to detect this specific case.

So far only static eccentricity is considered in this motor with inclined rotor. However, as we know, severe static eccentricity would bring up some degree of dynamic eccentricity. Thus, the variant of MFWA proposed in this thesis can be extended to more complicated inclined rotor case. For example, if the inclined rotor rotates around the axis of the stator, it will generate the combination of inclined static eccentricity and dynamic eccentricity.

The two cases described above deserve further research endeavors and the results should be useful for the designers of online monitoring systems.

Bibliography

[1] P. Vas, "*Parameter Estimation, Condition Monitoring and Diagnosis of Electrical Machines*," Clarendron Press, Oxford, 1993.

[2] G. B. Kliman and J. Stein, "Induction motor fault detection via passive current monitoring", *International Conference in Electrical Machines*, Cambridge, MA, pp.13-17, August 1990.

[3] S. Nandi, H. A. Toliyat, "Condition monitoring and fault diagnosis of electrical machines-a review", *IEEE Conference Record of the 34th IAS Annual Meeting*, Vol. 1, pp. 197-204, Phoenix, Arizona, 1999

[4] A. Barbour and W. T. Thomson, "Finite element study of rotor slot designs with respect to current monitoring for detecting static air-gap eccentricity in squirrel-cage induction motor," *IEEE-IAS annual meeting conference recordings*, pp. 112-119, New Orleans, Louisiana, 1997

[5] Y. Akiyama, "Unbalance-heating phenomena of induction motor with eccentric rotor", *Conference record of IEEE IAS Annual Meeting Recordings*, pp.107-114, 1992

[6] Y. Akiyama, O. Sugiura, "A study of 2sf beat phenomena in induction motor", *Conference record of IEEE IAS Annual Meeting*, Vol. 1, pp. 100 – 106, Oct. 1992

[7] D. G. Dorrell, W. T. Thomson and S. Roach, "Analysis of air-gap flux, current, vibration signals as a function of the combination of static and dynamic air-gap eccentricity in 3-phase induction motors", *IEEE Trans. Industry Applications*, Vol. 33, No. 1, pp. 24-34, 1997.

[8] W. T. Thomson, and A. Barbour, "On-line current monitoring and application of a finite element method to predict the level of static air-gap eccentricity in three-phase induction motors," *IEEE Trans. Energy Conversion,* Vol. 13, No. 4, pp. 347-357, Dec. 1998.

[9] J. R. Cameron, W. T. Thomson, and A. B. Dow, "Vibration and current monitoring for detecting air-gap eccentricity in large induction motors," *IEE Proceedings,* Vol. 133, pt. B, No. 3, pp. 155-163, May 1986.

[10] Gaylard, A.; Meyer, A.; Landy, C.; "Acoustic evaluation of faults in electrical machines", *Seventh International Conference on Electrical Machines and Drives*, (Conf. Publ. No. 412), Pages: 147 – 150, 11-13 Sep. 1995.

[11] W. T. Thomson, D. Rankin, and D.G. Dorrell, "On-line current monitoring to diagnose air-gap eccentricity in large three-phase induction motors-industrial case histories verify the predictions," *IEEE Trans. Energy Conversion,* Vol. 14, No. 4, pp. 1372-1378, Dec. 1999.

[12] J. Penman, M. N. Dey, A. J. Tait, W. E. Bryan, " Condition monitoring of electrical drives", *IEE Proceedings*, Vol. 133, pt. B, No.3, pp. 142-148, May 1986.

[13] H. A. Toliyat, M. S. Arefeen, A. G. Parlos, "A method for dynamic simulation of air-gap eccentricity in induction machines," *IEEE Trans. Industry Applications*, Vol. 32, No. 4, pp. 910-918, July/Aug., 1996.

[14] N. A. Al-Nuaim, H. A. Toliyat, "A novel method for modeling dynamic air-gap eccentricity in synchronous machines based on modified winding function theory," *IEEE Trans. Energy Conversion*, Vol. 13, No. 2, pp. 156-162, June 1998.

[15] M. Haji, H. A. Toliyat, "Rotor eccentricity fault detection of a DC motor", *Proceedings of the Industrial Electronics Society Conference (IECON)*, Denver, CO,

pp. 591-596, Nov.29-Dec.2, 2001.

[16] R. Ong, J. H. Dymond, R. D. Findlay and B. Szabados, "Shaft current in ac induction machine-an online monitoring system and prediction rules", *IEEE Trans. on Industry Applications*, Vol. 37, No. 4, pp. 1189-1196, July/August 2001.

[17] J. F. Bangura, N. A. O. Demerdash, "Comparison between characterization and diagnosis of broken bars/endring connectors and air-gap eccentricities of induction motors in ASD's using a coupled Finite Element-State Space method", *IEEE Trans. Energy Conversion*, Vol. 15, No. 1, pp. 48-56, March 2000.

[18] M. E. H. Benbouzid, G. B. Kliman, "What stator current processing-based technique to use for induction motor rotor faults diagnosis?", *IEEE Trans. Energy Conversion*, Vol. 18, No. 2, pp. 238-244, June 2003.

[19] A. J. M. Cardoso, E. S. Saraiva, " Computer-aided detection of airgap eccentricity in operating three-phase induction motors by Park's vector approach", *IEEE Trans. Industry Applications*, Vol. 29, No. 5, pp. 897-901, Sept./ Oct. 1993.

[20] N. Arthur, J. Penman, "Induction machine condition monitoring with higher order spectra", *IEEE Trans. Industrial Electronics*, Vol. 47, No. 5, pp.1031-1041, Oct. 2000

[21] M. E. H. Benbouzid, "A review of induction motors signature analysis as a medium for faults detection", *IEEE Trans. Industrial Electronics*, Vol. 47, No. 5, pp.984-993, Oct. 2000.

[22] M. Haji, H. A. Toliyat, "Pattern Recognition— a technique for induction machines rotor fault detection 'eccentricity and broken bar fault'", *IEEE IAS annual meeting conference recordings*, Vol. 3, pp. 1572-1578, 2001.

[23] F. Filippetti, G. Franceschini, C. Tassoni, Peter Vas, "Recent developments of induction motor drvies fault diagnosis using AI techniques", *IEEE Trans. Industrial Electronics*, Vol. 47, No. 5, pp. 994-1004, October 2000.

[24] F. Filippetti, G. Franceschini, C. Tassoni, "Neural networks aided on-line diagnostics of induction motor faults", *Proceedings of the IEEE -IAS Annual Meeting Conference*, Vol. 1, pp. 316-323, Toronto, Canada 1993.

[25] J. Penman, C. M. Yin, "Feasibility of using unsupervised learning, artificial neural networks for the condition monitoring of electrical machines", *IEE Proceedings on Electr. Power Applns.*, Vol. 141, No. 6, pp. 317-322, Nov.1994.

[26] R. R. Schoen, B. K. Lin, T. G. Habetler, J. H. Schlag, S. Farag, "An unsupervised on-line system for induction motor fault detection using stator current monitoring," *IEEE Trans. Industry Applications,* Vol. 31, No. 6, pp. 1280-86, Nov-Dec 1995.

[27] S. Nandi, "Modeling of induction machines including stator and rotor slot effects", *IEEE Trans. Industry Applications*, Vol. 40, Issue: 4, Pages: 1058-1065, July-Aug. 2004

[28] S. Nandi, S. Ahmed, H. A. Toliyat, "Detection of rotor slot and other eccentricity related harmonics in a three-phase induction motor with different rotor cages", *IEEE Trans. Energy Conversion,* Vol. 16, No. 3, pp. 253-260, Sept. 2001.

[29] A. Ferrah, P. J. Hogben-Liang, K. J. Bradley, G. M. Asher, M. S. Woolfson, "The effect of rotor design of sensorless speed estimation using rotor slot harmonics identified by adaptive digital filtering using the maximum likelihood approach," *IEEE-IAS annual meeting conference recordings*, pp. 128-135, New Orleans, Louisiana, Oct. 5-8, 1997.

[30] S. Nandi, R. M. Bharadwaj, H. A. Toliyat, "Performance analysis of a three phase

induction motor under incipient mixed eccentricity condition", *IEEE Trans. Energy Conversion,* Vol. 17, No. 3, pp.392-399, Sept. 2002

[31] "*MATLAB 6.5 Release 13*", The MathWorks Inc., Natick, MA

[32] H. A. Toliyat, T. A. Lipo, "Transient analysis of cage induction machines under stator, rotor bar and end ring faults", *IEEE Trans. Energy Conversion,* Vol. 10, No. 2, pp. 241-247, June 1995.

[33] Excerpts from class notes of ELEN689 "General theory of Electrical machines", Texas A&M Univesity, 1997

[34] S. Nandi, R. M. Bharadwaj, H. A. Toliyat, "Mixed eccentricity in three phase induction machines: analysis, simulation and experiments", *Conference record of IEEE IAS Annual Meeting*, Vol. 3, pp.1525 – 1532, Oct. 2002

[35] R. R. Schoen, T. G Habetler, "Effects of time-varying loads on rotor fault detection in induction machines", *IEEE Trans. Industry Applications,* Vol. 31, No. 4, pp. 900-906, 1995

[36] "*Maxwell 2D 10.0*", Ansoft Corporate, Pittsburgh, PA

[37] S. Nandi, H. A. Toliyat, "Novel frequency-domain-based technique to detect stator inter-turn faults in induction machines using stator-induced voltage after switch-off", *IEEE Trans. Industry Applications*, Vol. 38, No. 1, pp. 101-109, Jan/Feb. 2002.

Appendix A

Motor Data for Inclined Eccentricity Simulation and Experiment

Type: *Labvolt* M-8503

3 phase, four-pole, s, star connected, 2 kW, 60 Hz, 36 stator slots and 45 rotor bars (slots).

1) Stator resistance (per phase) r_s= 0.6 ohm.

2) Stator leakage inductances (per phase): L_{ls}=0.002918 H.

3) Rotor bar resistance r_b=58.27e-07 ohm.

4) Rotor bar leakage inductance L_b=0.343e-09 H.

5) End ring (one segment) resistance r_e=4.5314e-07 ohm.

6) End ring (one segment) leakage inductance L_e=0.175e-09 H.

7) Mean radius r=73.75*1e-03m.

8) Length l_s=76*1e-03m.

9) Air-gap g =0.5e-03m.

10) Carters coefficient =1.95.

11) Inertia J_k= 0.107 kg-m^2.

12) Rotor bar skew 11degrees.

Appendix B
Additional Simulation Results of Motor Inductances

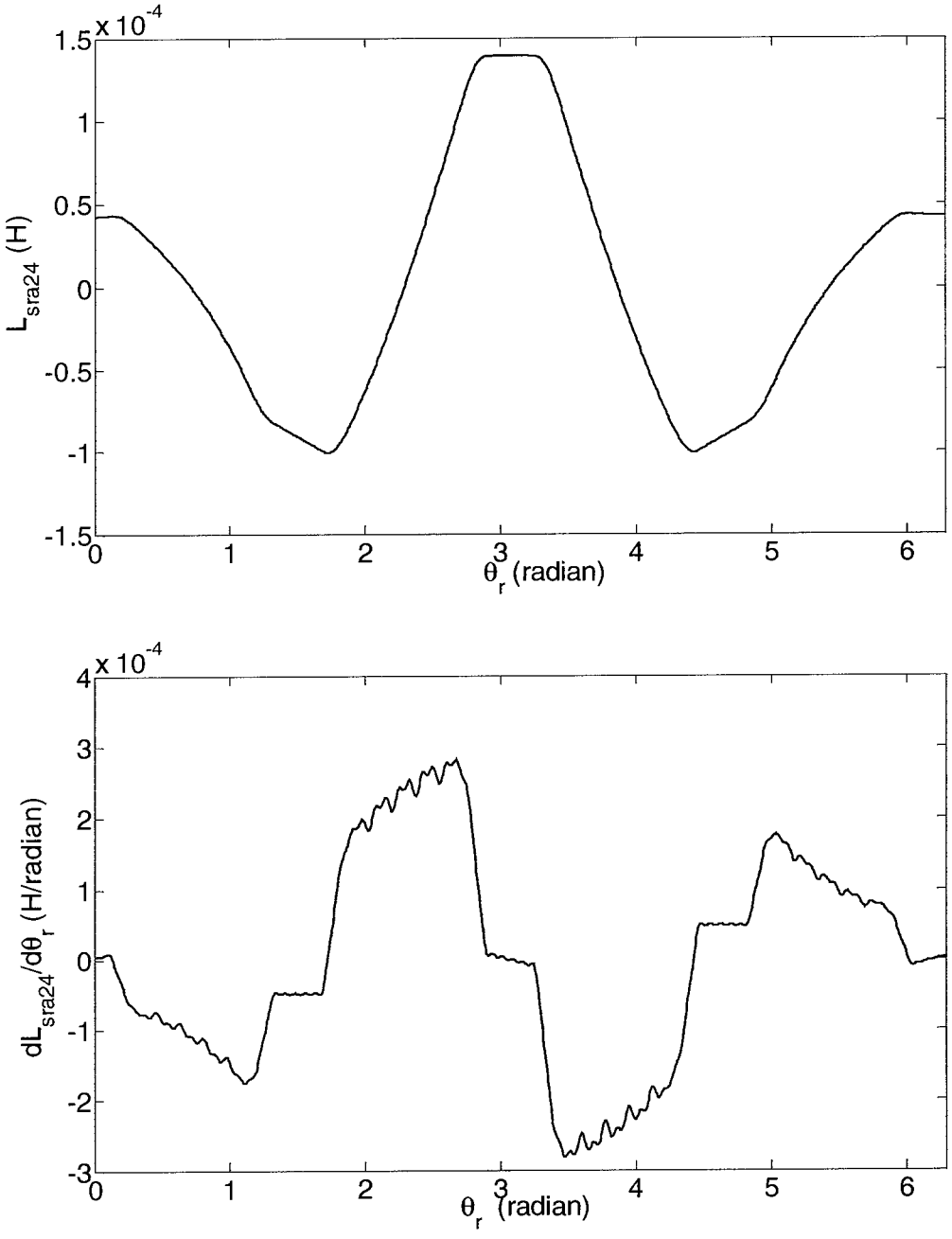

Figure B1 Mutual inductance L_{sra24} (top) and its derivative (bottom) under uniform 50% SE between stator phase *a* and rotor loop 24

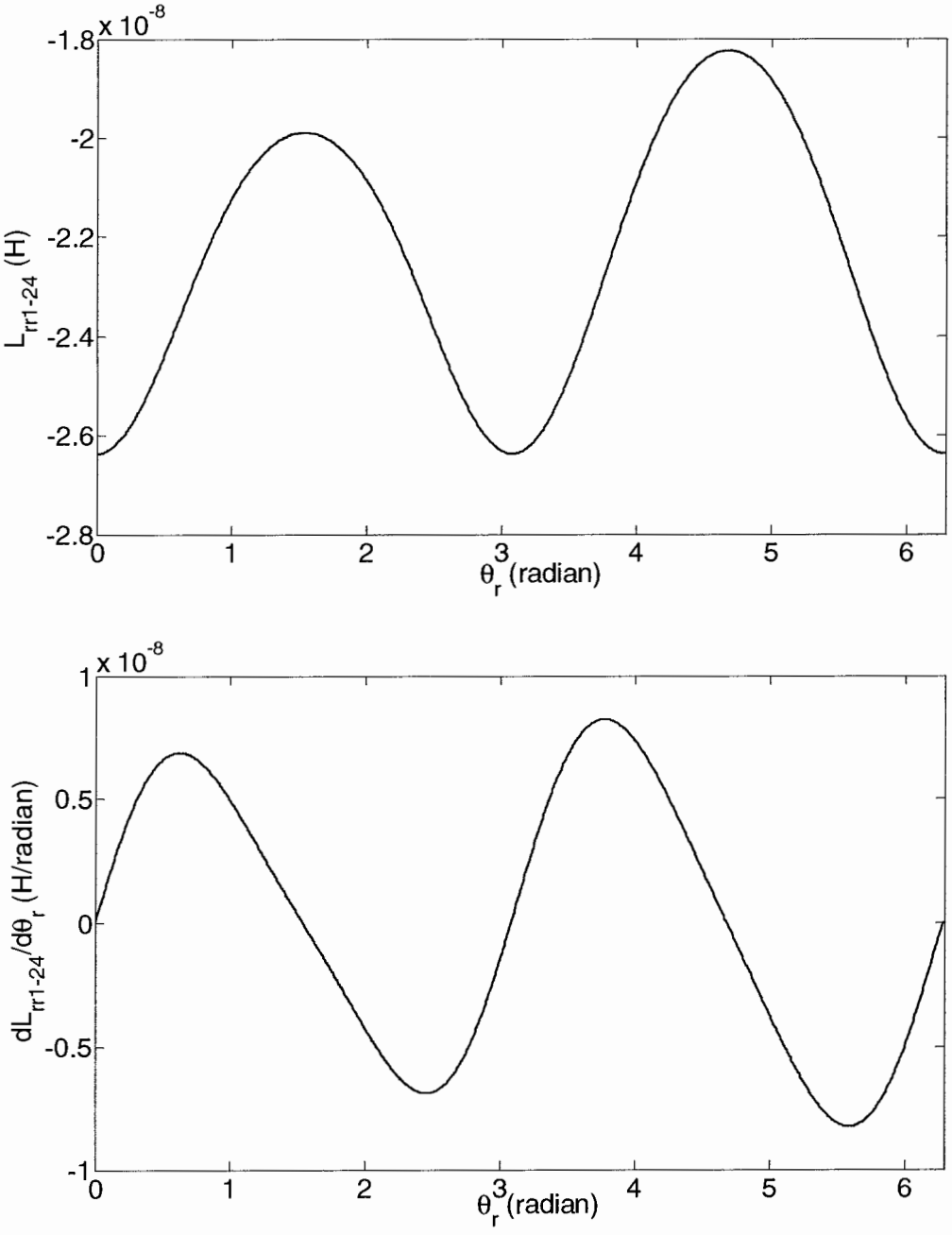

Figure B2 Mutual inductance $L_{rr1\text{-}24}$ (top) and its derivative (bottom) under uniform 50% SE between rotor loop 1 and loop 24

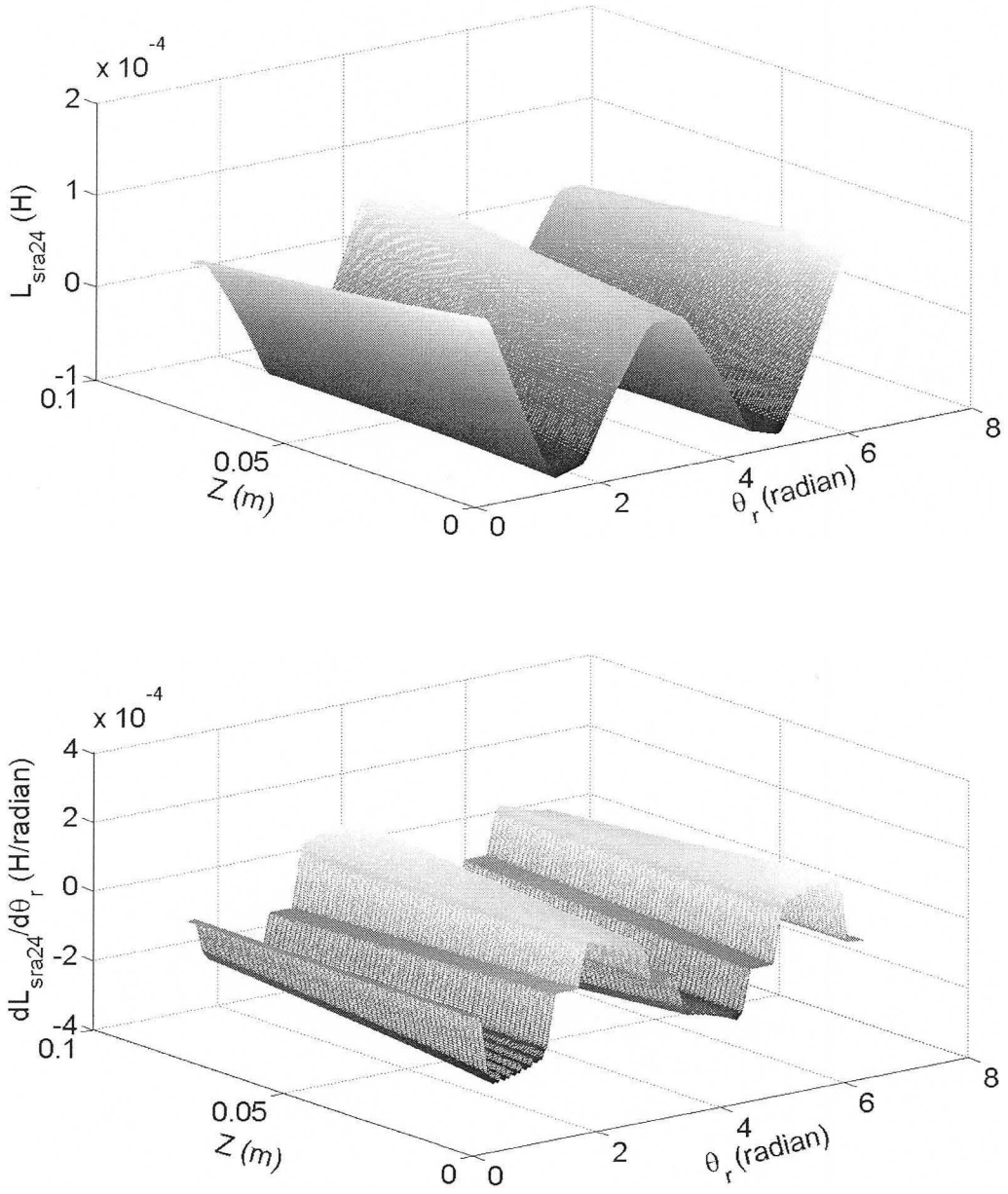

Figure B3 Variation of mutual inductance L_{sra24} (top) and its derivative (bottom) under inclined static eccentricity (one end 50% SE, the other end -50% SE) between stator phase *a* and rotor loop 24.

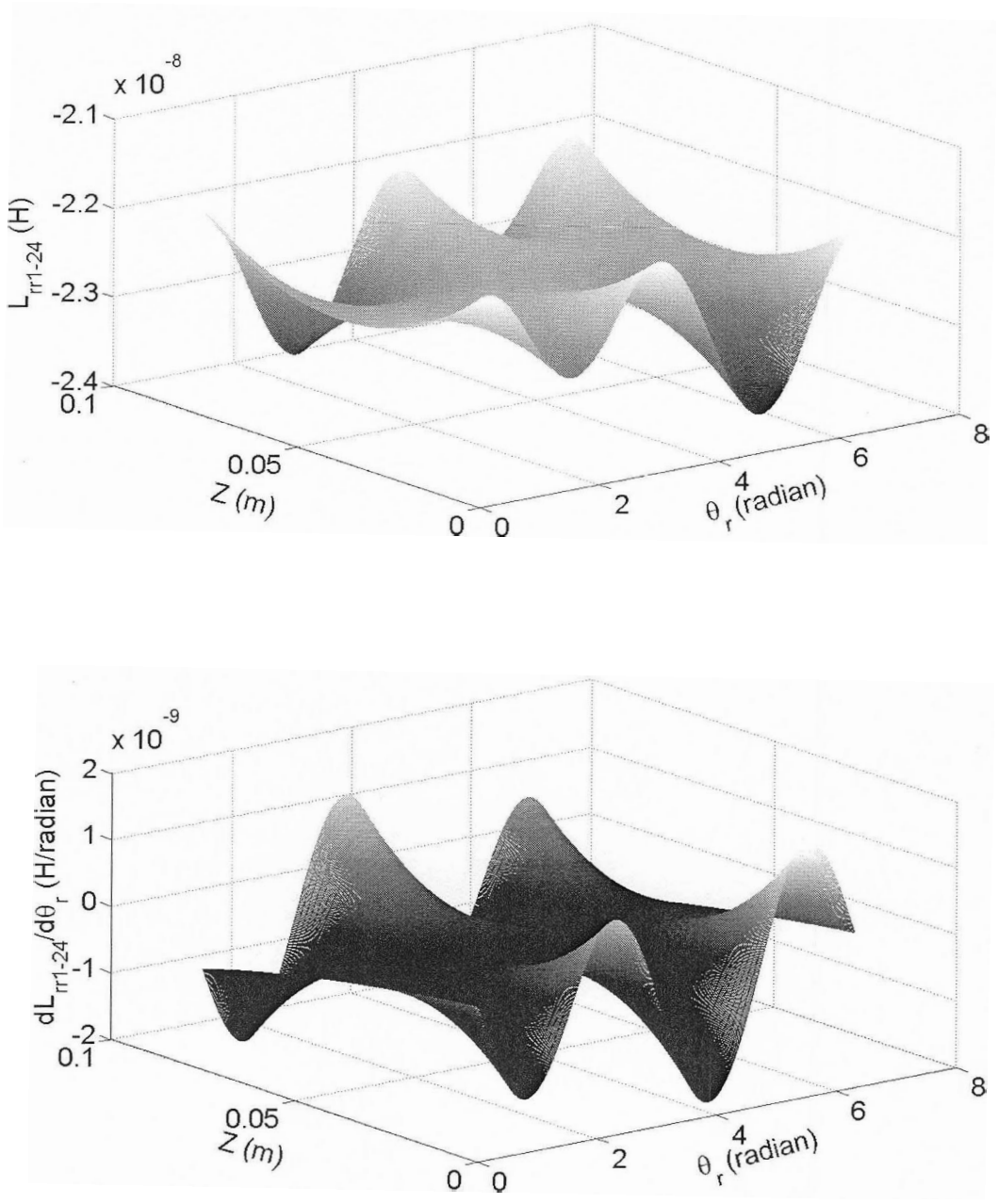

Figure B4 Variation of mutual inductance $L_{rr1\text{-}24}$ (top) and its derivative (bottom) under inclined static eccentricity (one end 50% SE, the other end -50% SE) between rotor loop 1 and loop 24

Appendix C

Additional Simulation Results of Detection of Inclined Static Eccentricity

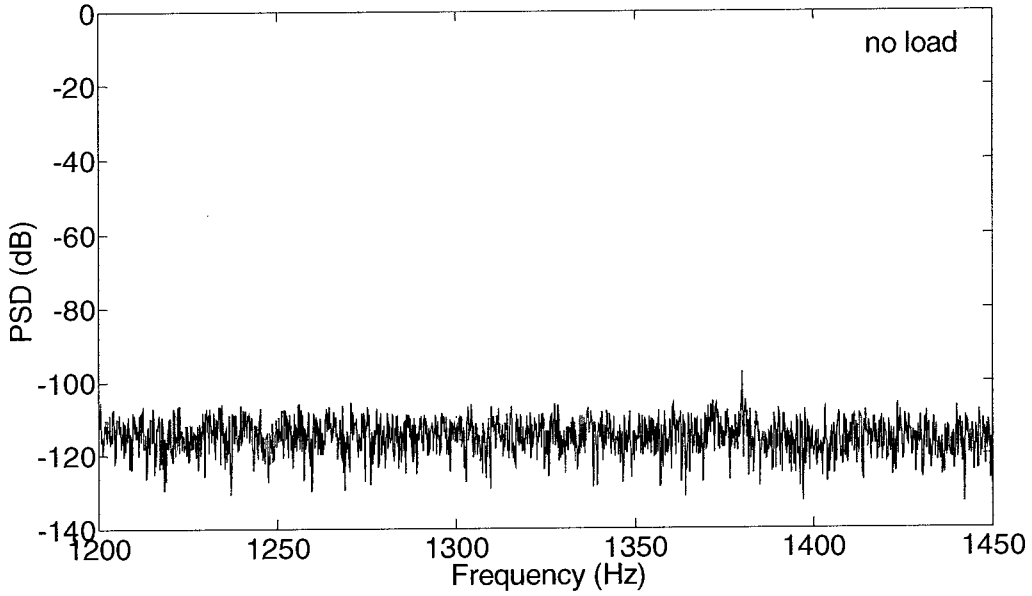

(a)

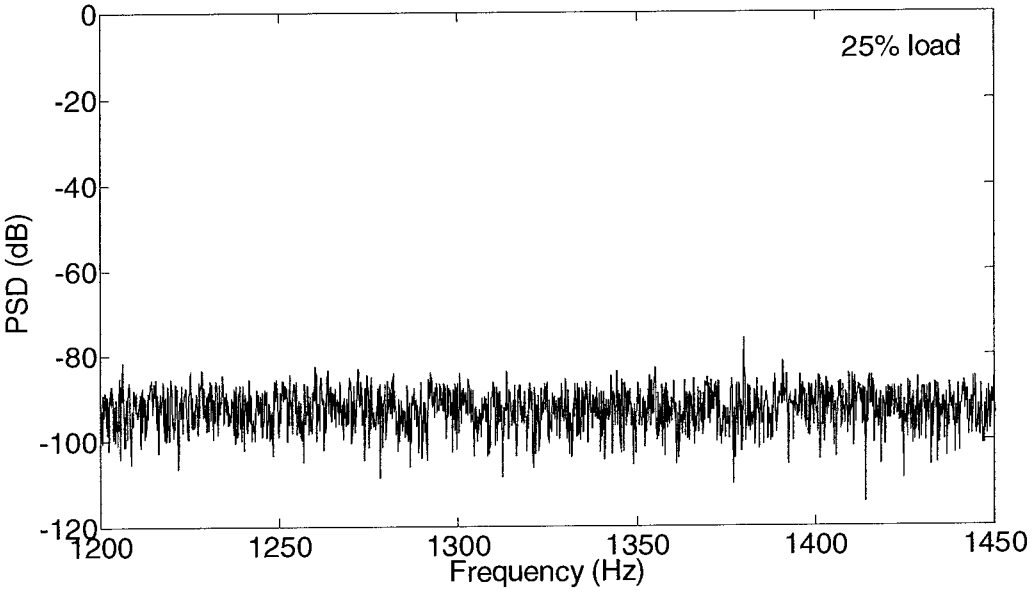

(b)

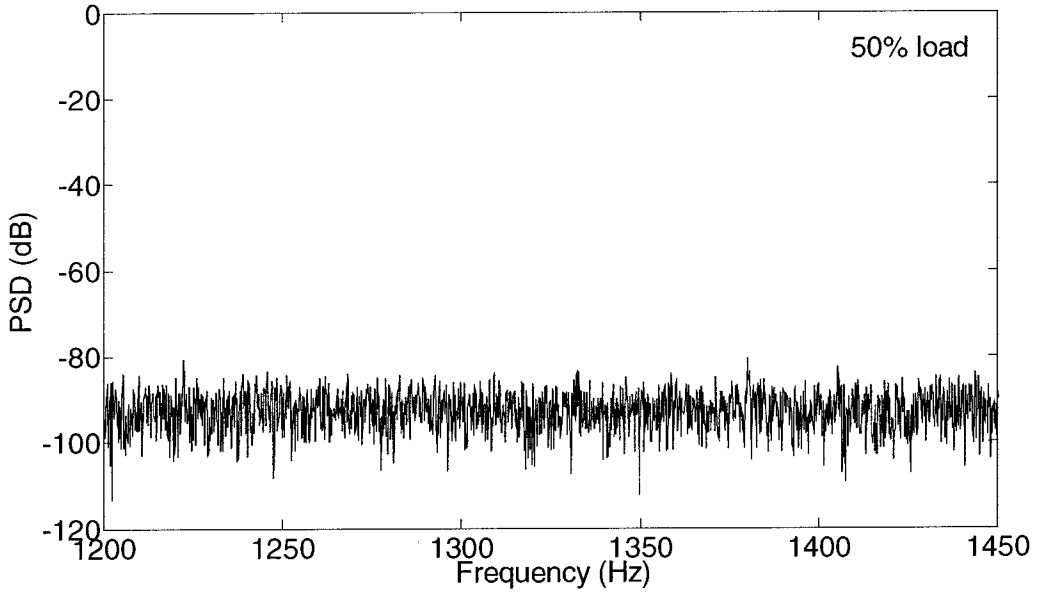

(c)

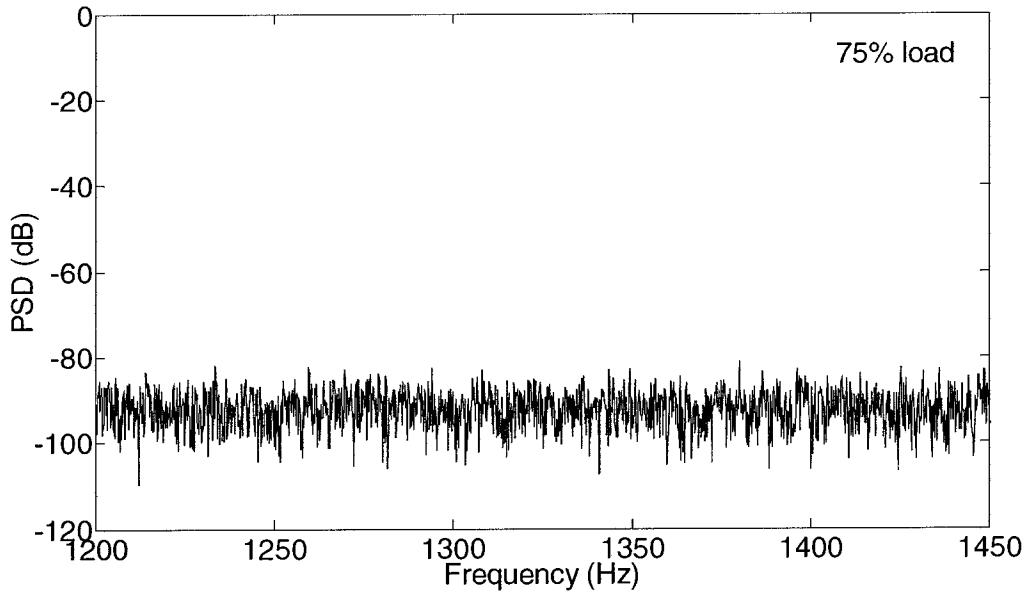

(d)

Figure C1 Simulated, normalized stator current spectra with uniform air-gap under (a) no load; (b) 25% load; (c) 50% load; (d) 75% load

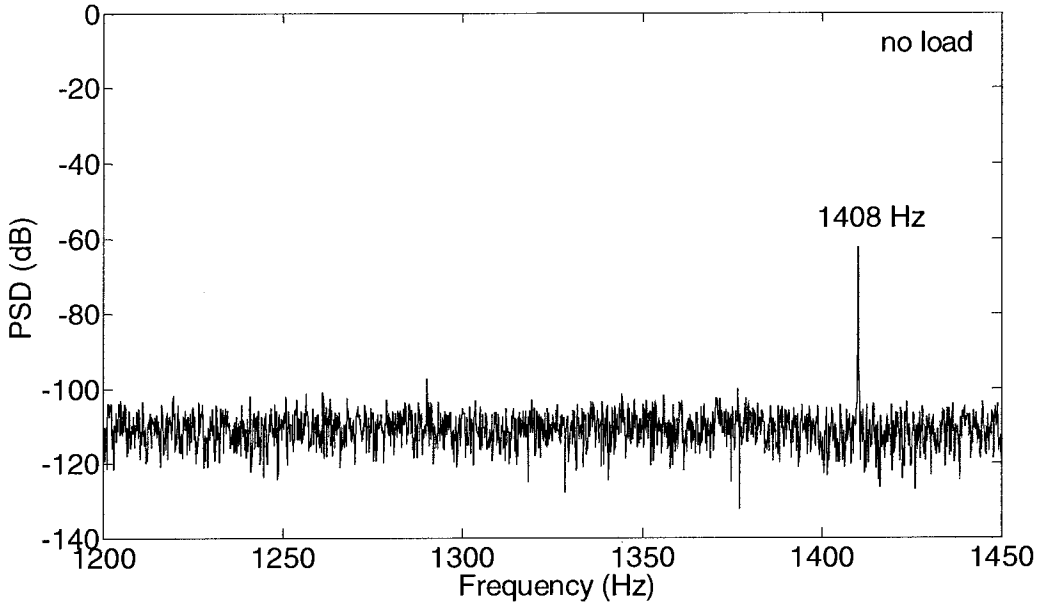
no load
1408 Hz
PSD (dB)
0
-20
-40
-60
-80
-100
-120
-140
1200
1250
1300
1350
1400
1450
Frequency (Hz)

(a)

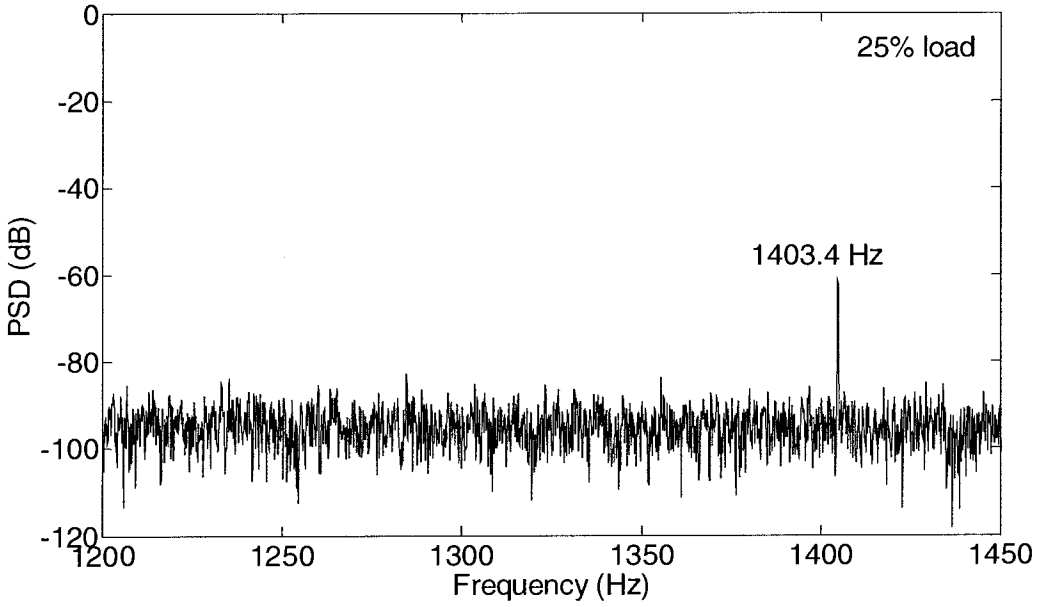
25% load
1403.4 Hz
PSD (dB)
0
-20
-40
-60
-80
-100
-120
1200
1250
1300
1350
1400
1450
Frequency (Hz)

(b)

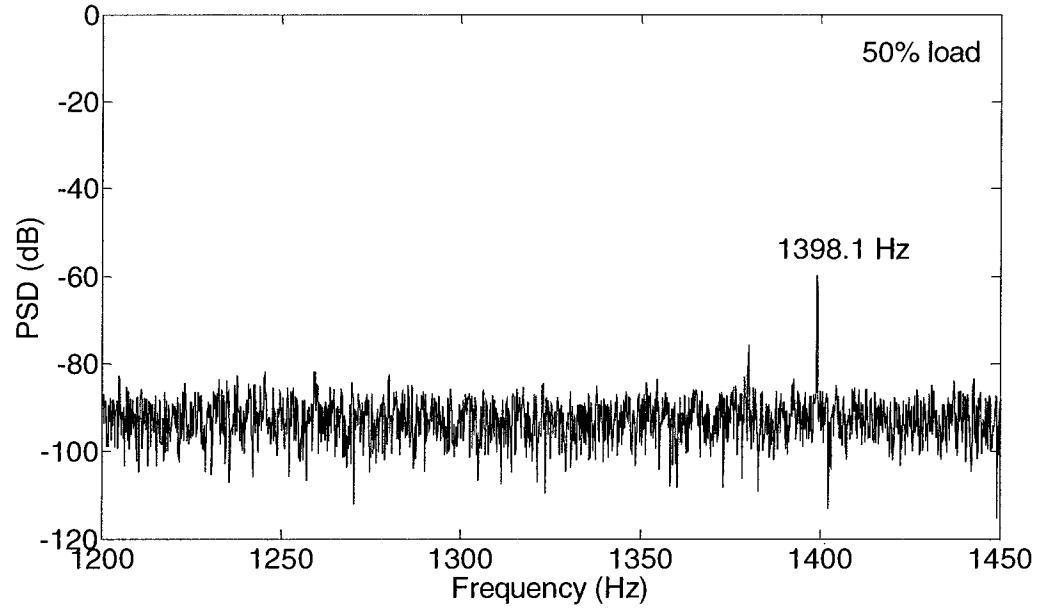

(c)

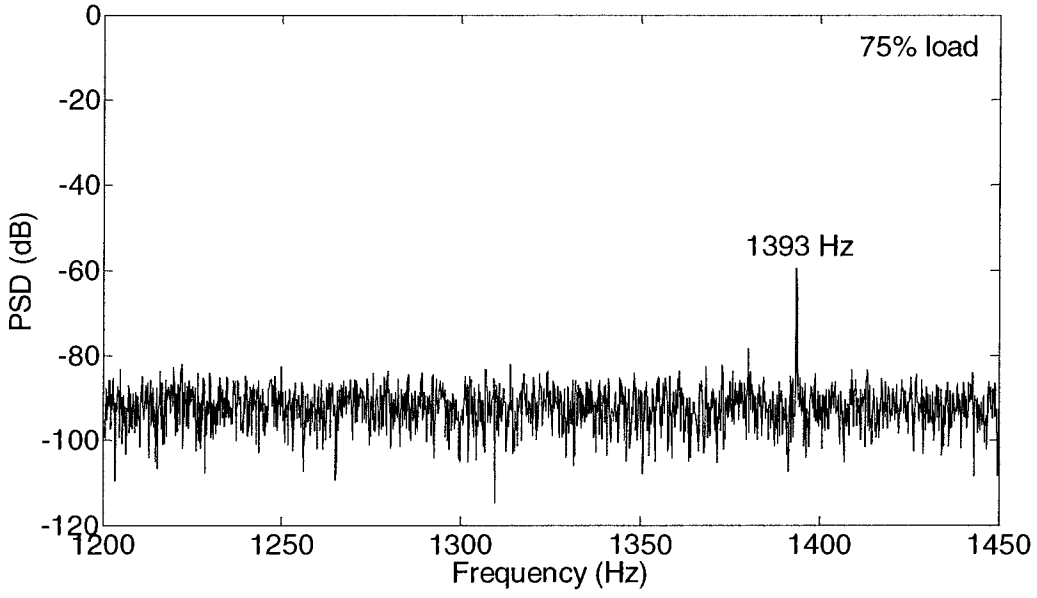

(d)

Figure C2 Simulated, normalized stator current spectra with uniform 25% SE under (a) no load; (b) 25% load; (c) 50% load; (d) 75% load

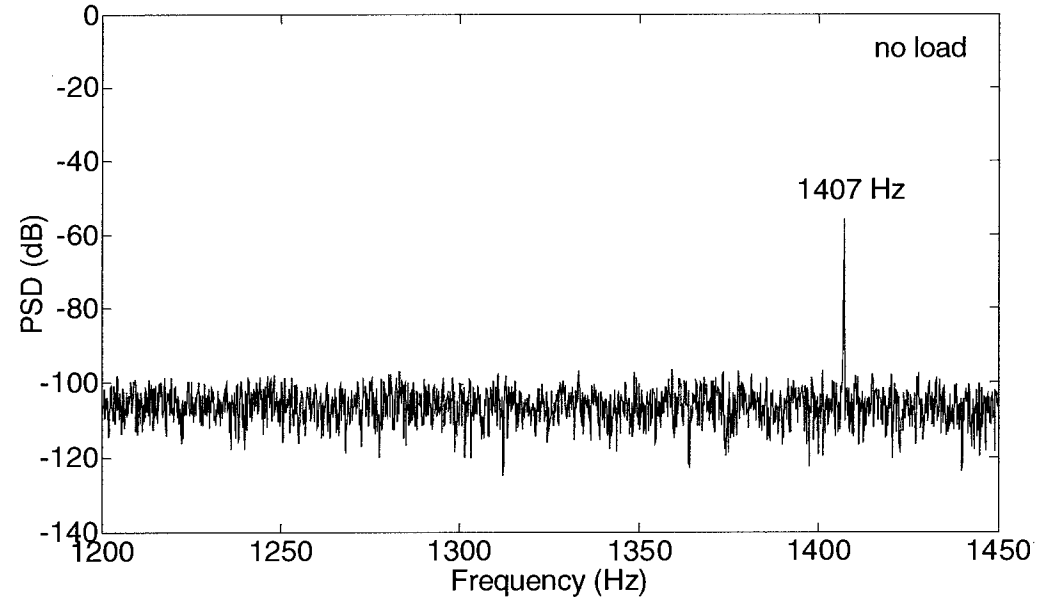
no load
1407 Hz
PSD (dB)
0
-20
-40
-60
-80
-100
-120
-140
1200
1250
1300
1350
1400
1450
Frequency (Hz)

(a)

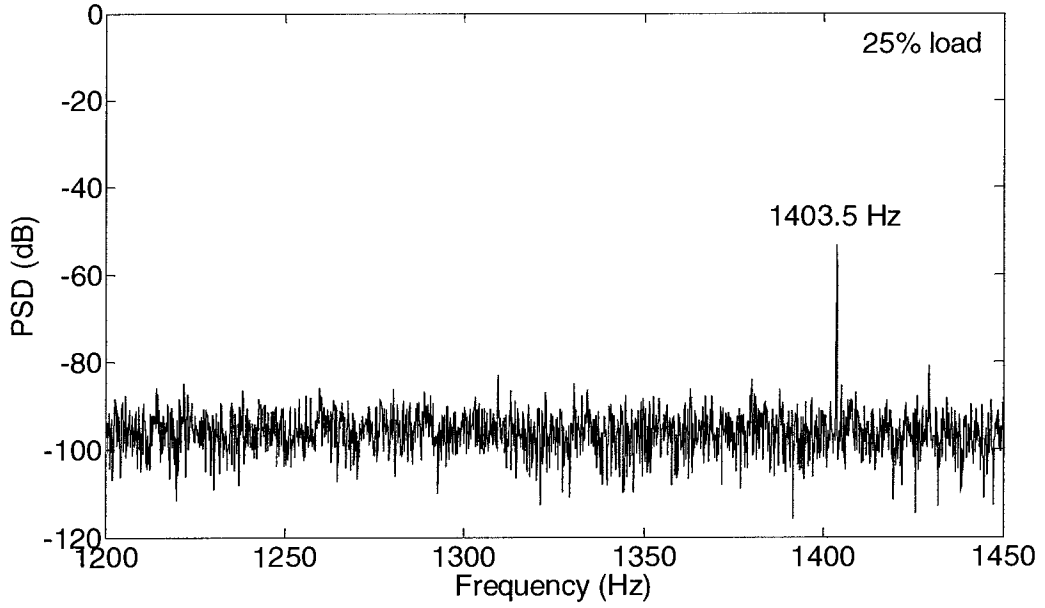
25% load
1403.5 Hz
PSD (dB)
0
-20
-40
-60
-80
-100
-120
1200
1250
1300
1350
1400
1450
Frequency (Hz)

(b)

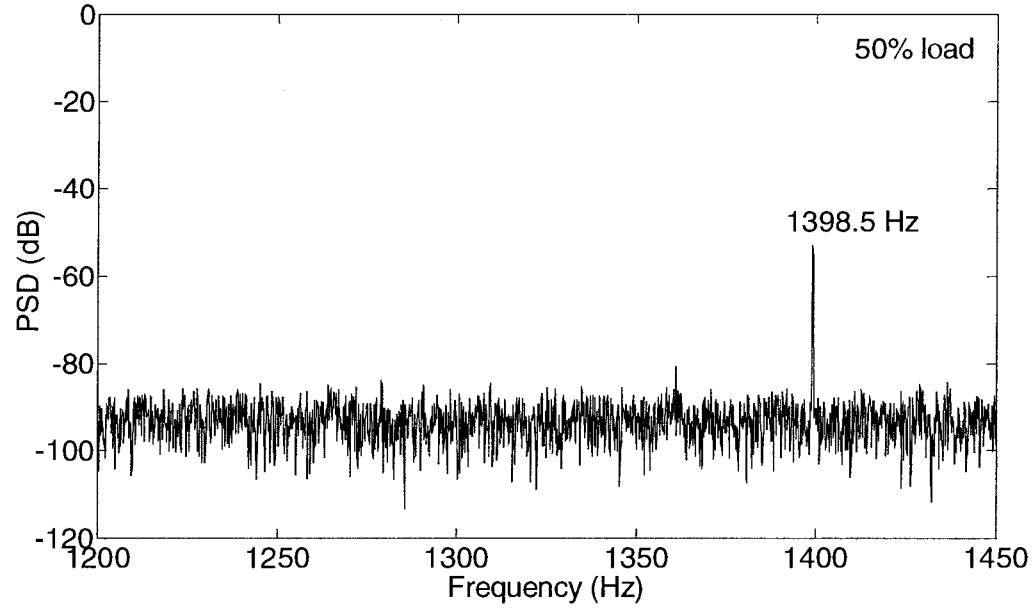

(c)

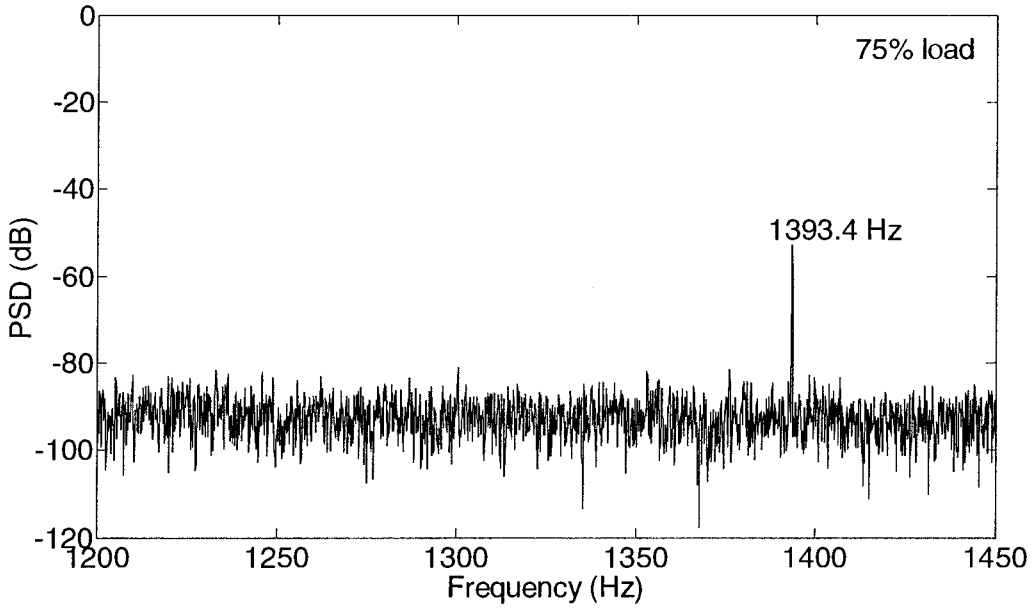

(d)

Figure C3 Simulated, normalized stator current spectra with uniform 50% SE under (a) no load; (b) 25% load; (c) 50% load; (d) 75% load

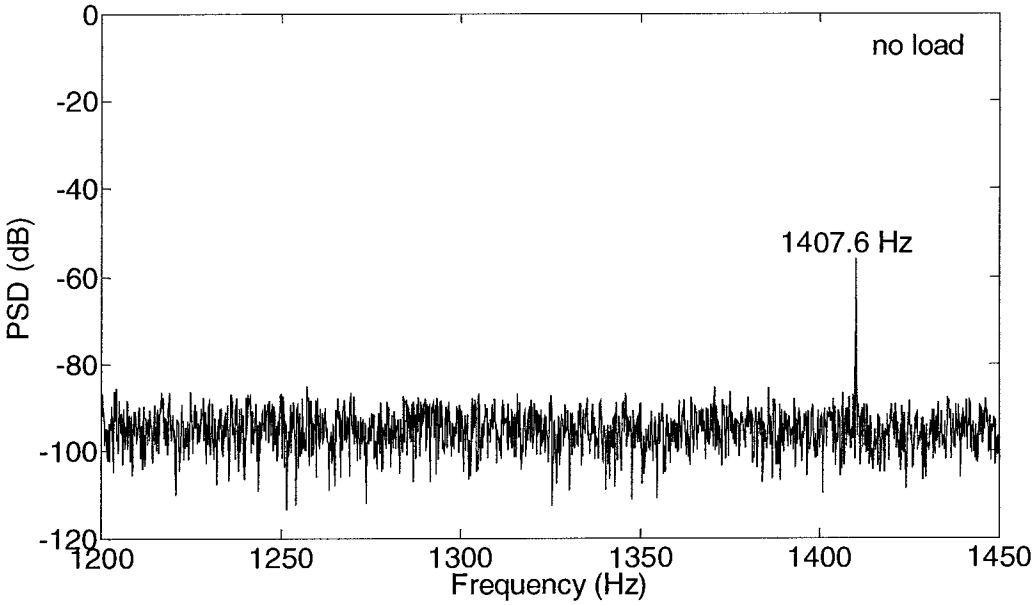
no load
1407.6 Hz
PSD (dB)
0
-20
-40
-60
-80
-100
-120
1200
1250
1300
1350
1400
1450
Frequency (Hz)

(a)

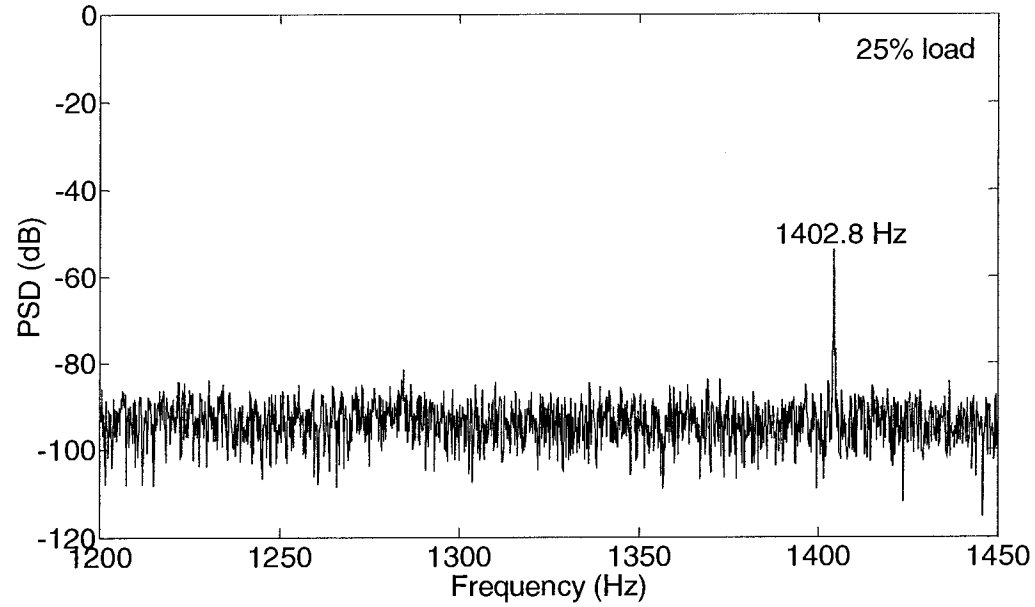
25% load
1402.8 Hz
PSD (dB)
0
-20
-40
-60
-80
-100
-120
1200
1250
1300
1350
1400
1450
Frequency (Hz)

(b)

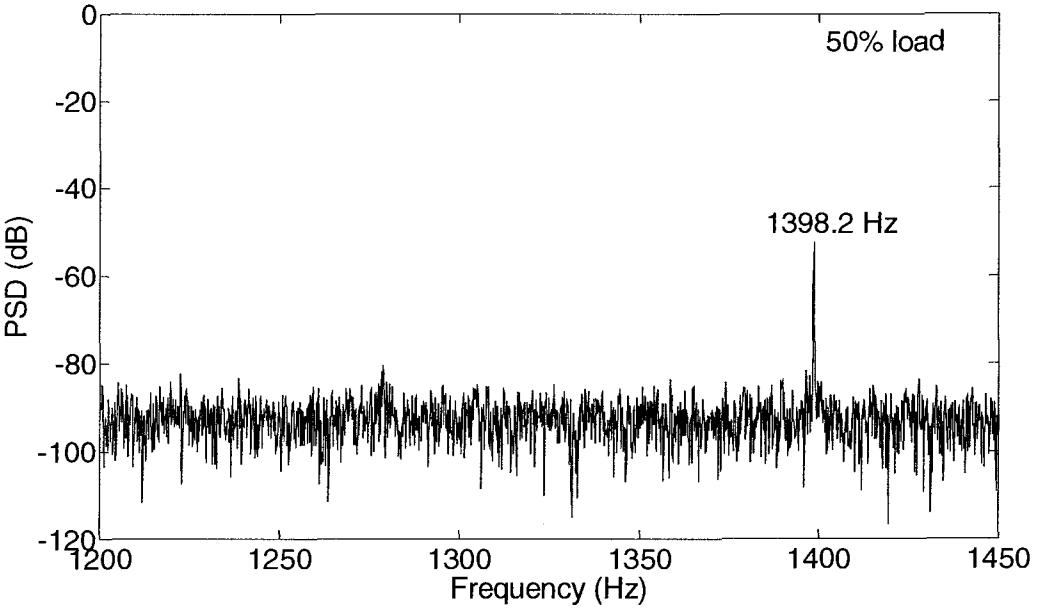

(c)

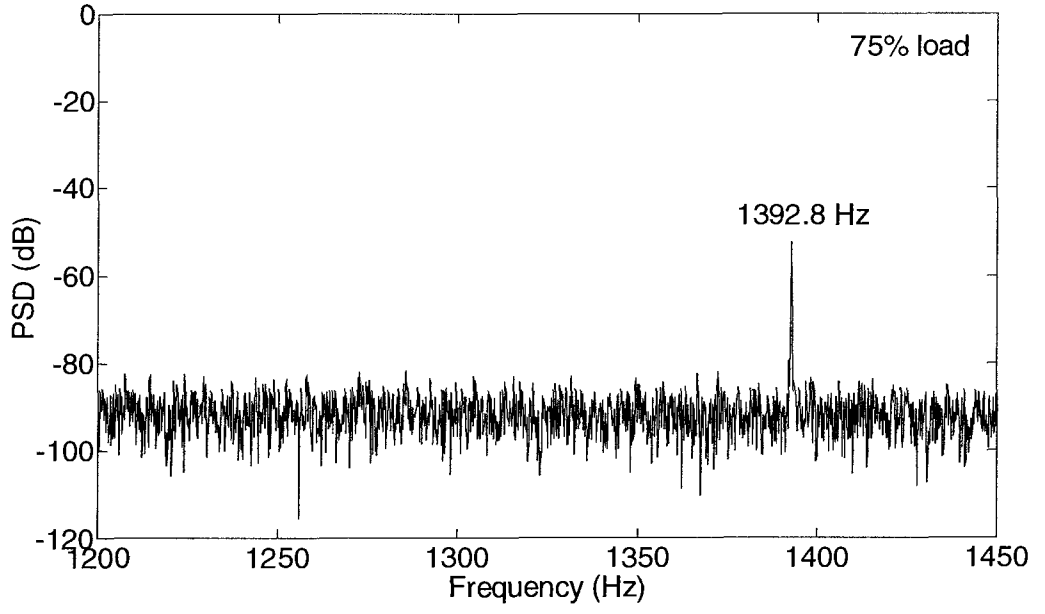

(d)

Figure C4 Simulated, normalized stator current spectra with inclined rotor (one end 40% SE, the other end 60% SE) under (a) no load; (b) 25% load; (c) 50% load; (d) 75% load

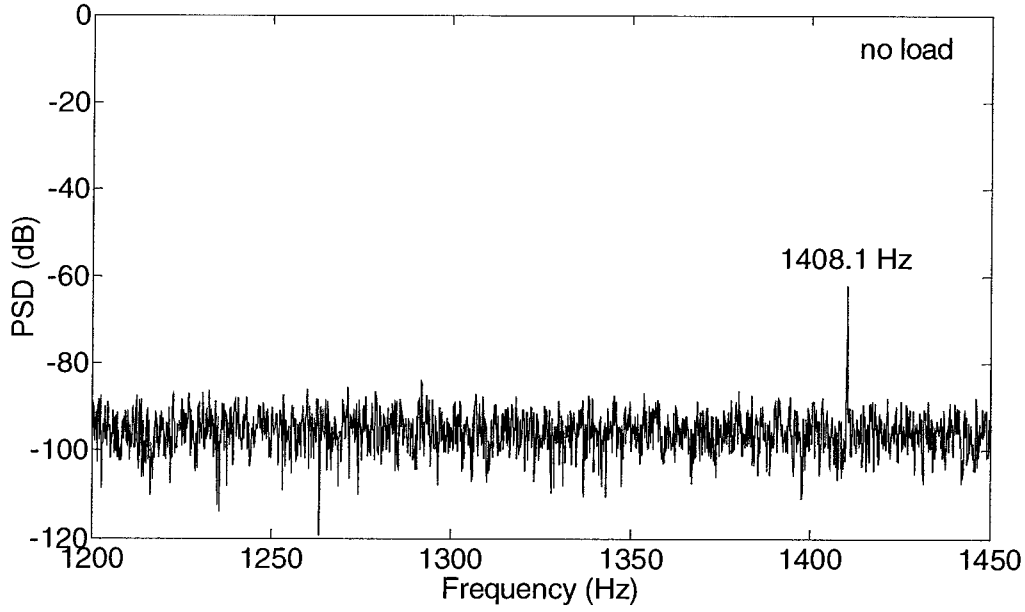
no load
1408.1 Hz
PSD (dB)
0
-20
-40
-60
-80
-100
-120
1200
1250
1300
1350
1400
1450
Frequency (Hz)

(a)

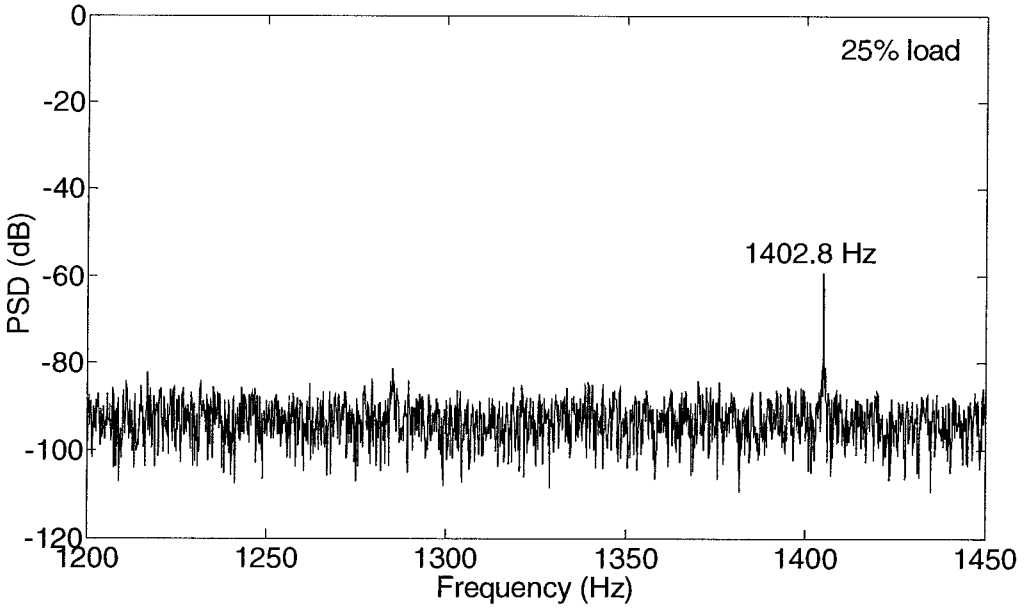
25% load
1402.8 Hz
PSD (dB)
0
-20
-40
-60
-80
-100
-120
1200
1250
1300
1350
1400
1450
Frequency (Hz)

(b)

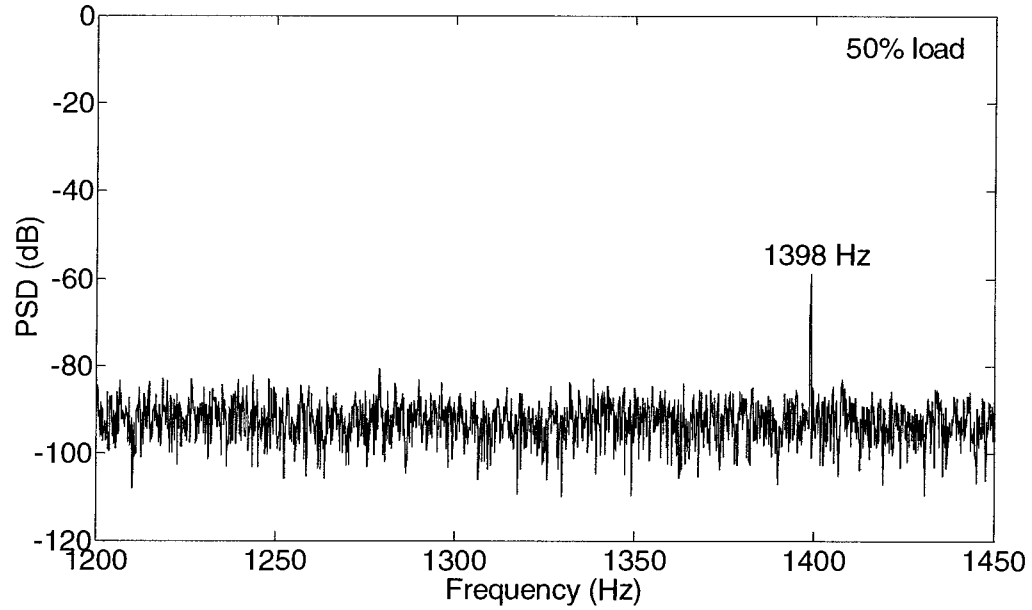

(c)

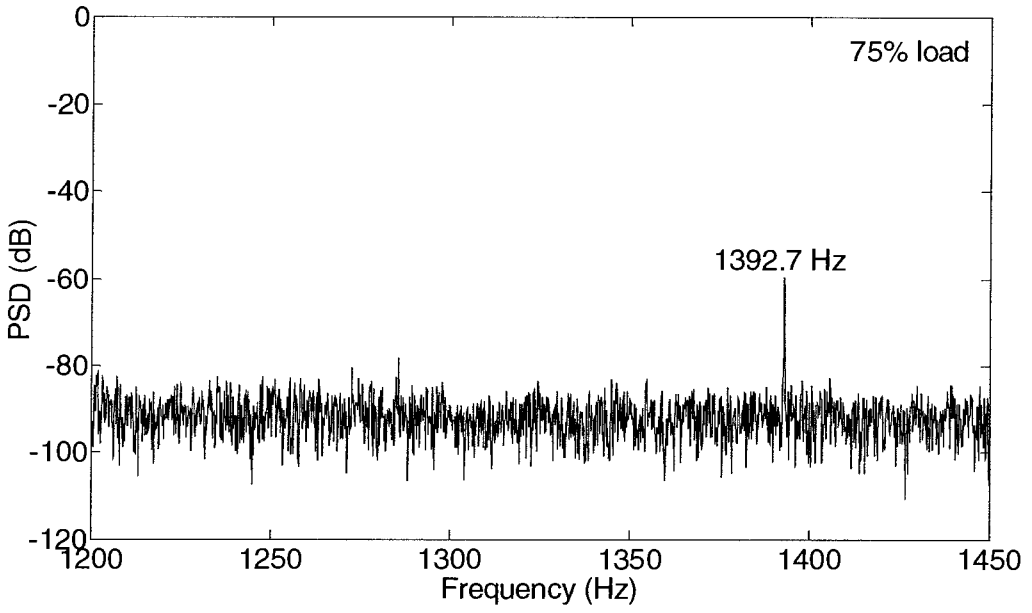

(d)

Figure C5 Simulated, normalized stator current spectra with inclined rotor (one end 0% SE, the other end 50% SE) under (a) no load; (b) 25% load; (c) 50% load; (d) 75% load

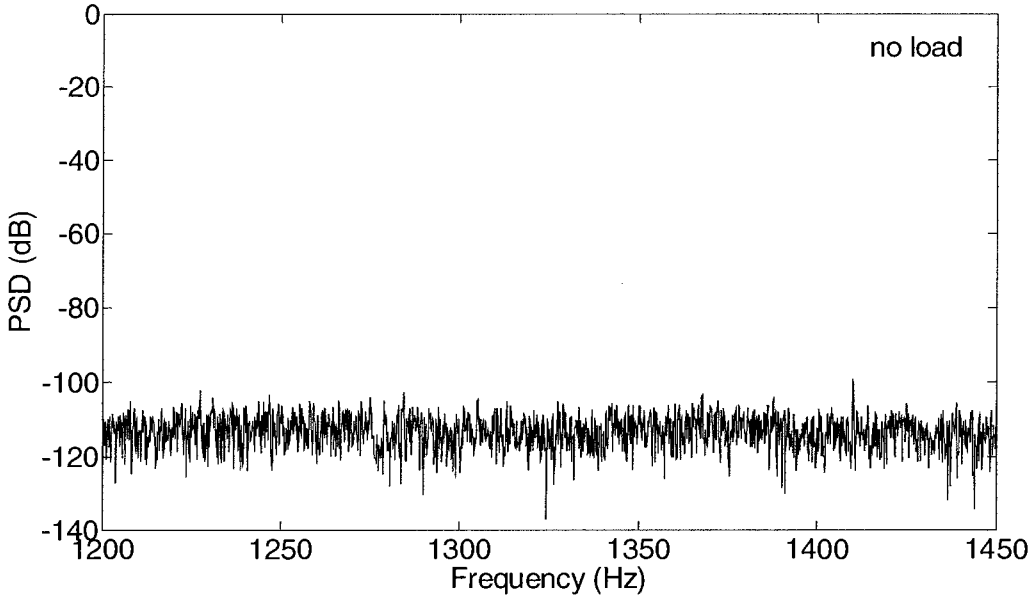
no load
PSD (dB)
0
-20
-40
-60
-80
-100
-120
-140
1200
1250
1300
1350
1400
1450
Frequency (Hz)

(a)

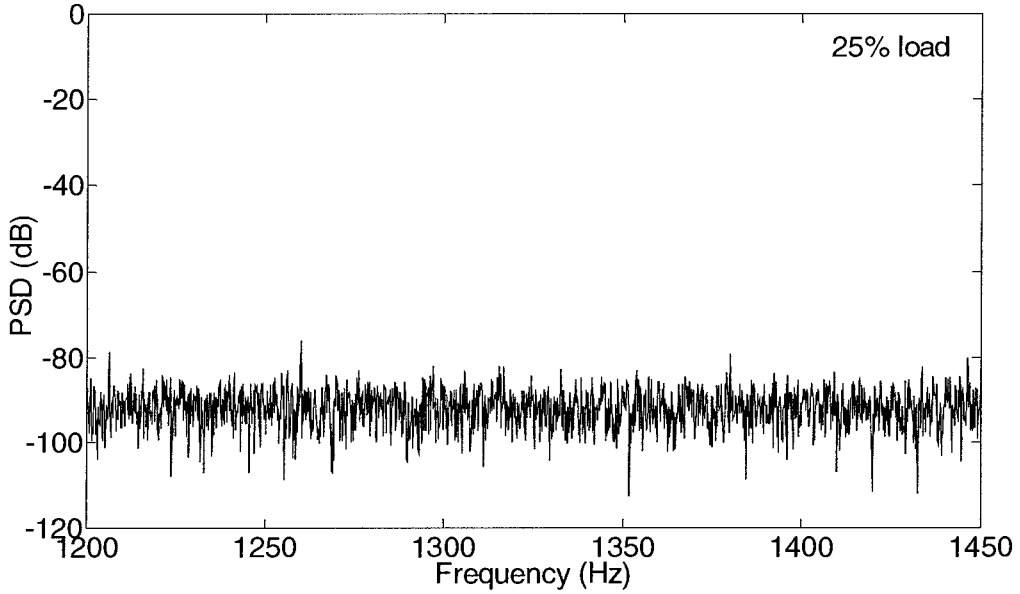
25% load
PSD (dB)
0
-20
-40
-60
-80
-100
-120
1200
1250
1300
1350
1400
1450
Frequency (Hz)

(b)

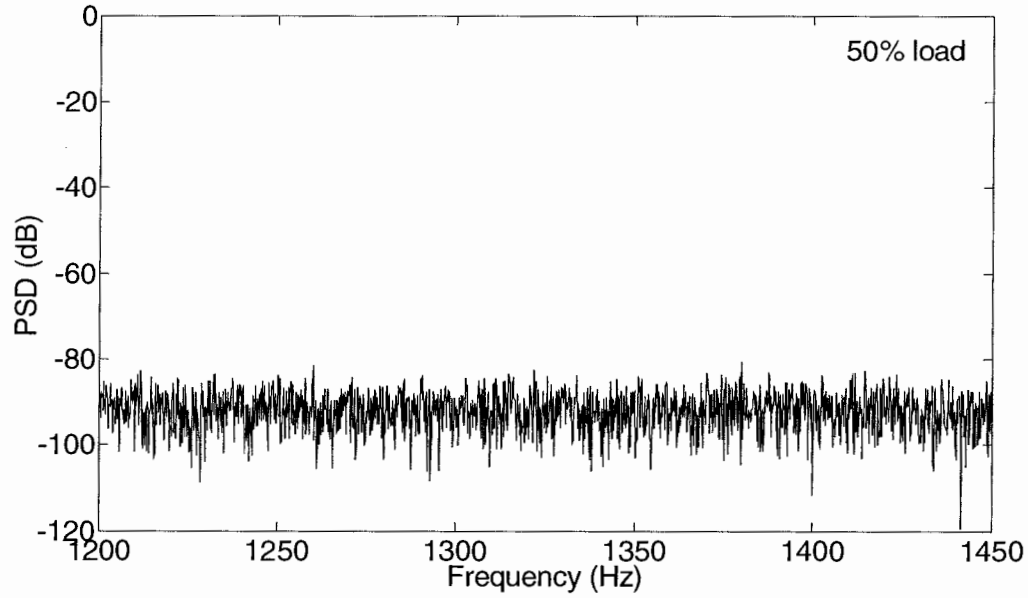

(c)

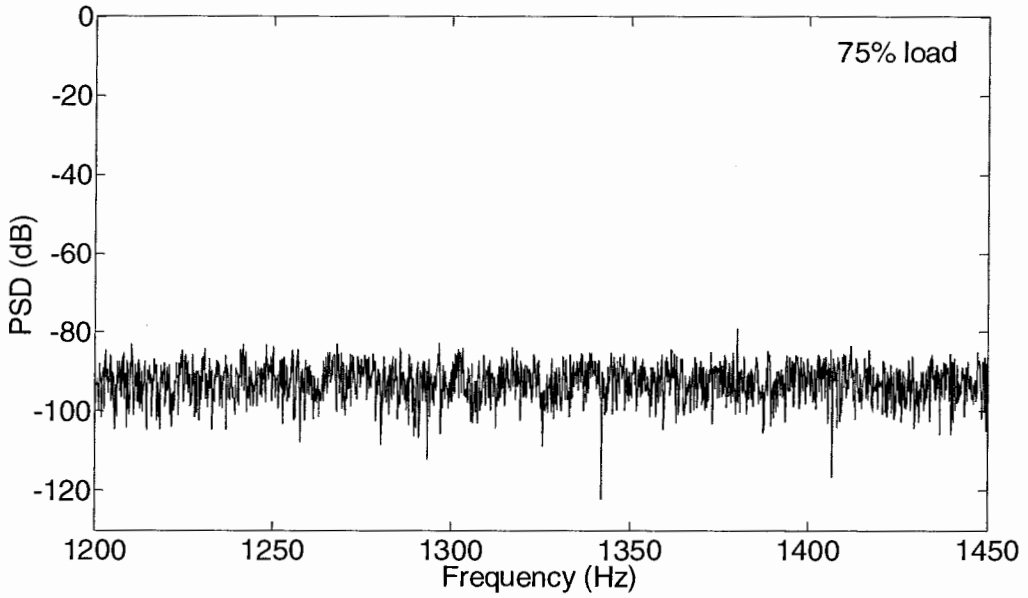

(d)

Figure C6 Simulated, normalized stator current spectra with inclined rotor (one end 50% SE, the other end -50% SE) under (a) no load; (b) 25% load; (c) 50% load; (d) 75% load

Appendix D

Additional Experimental Results of Detection of Inclined Static Eccentricity

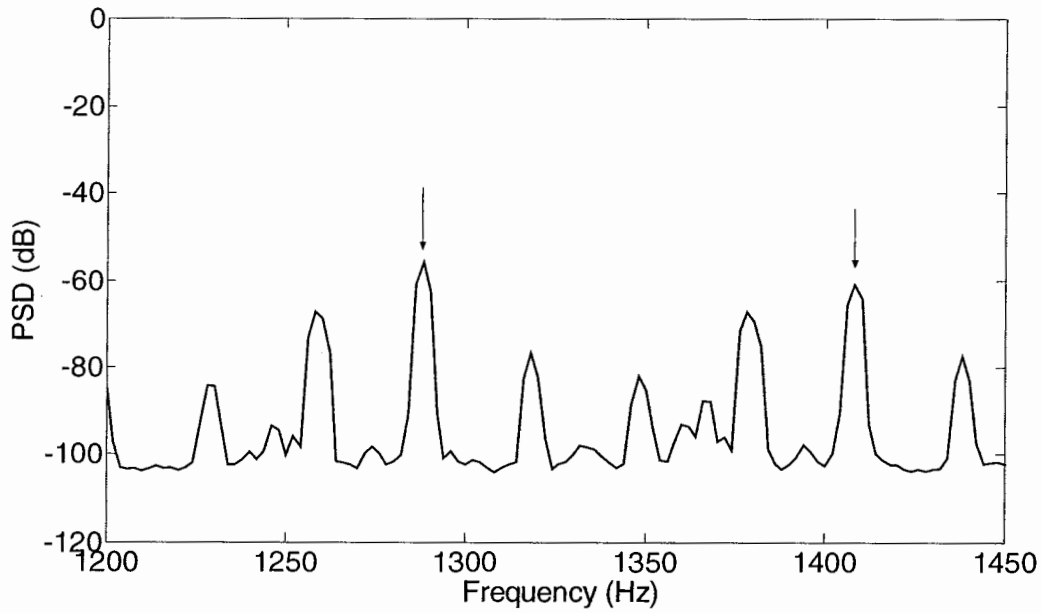

(a)

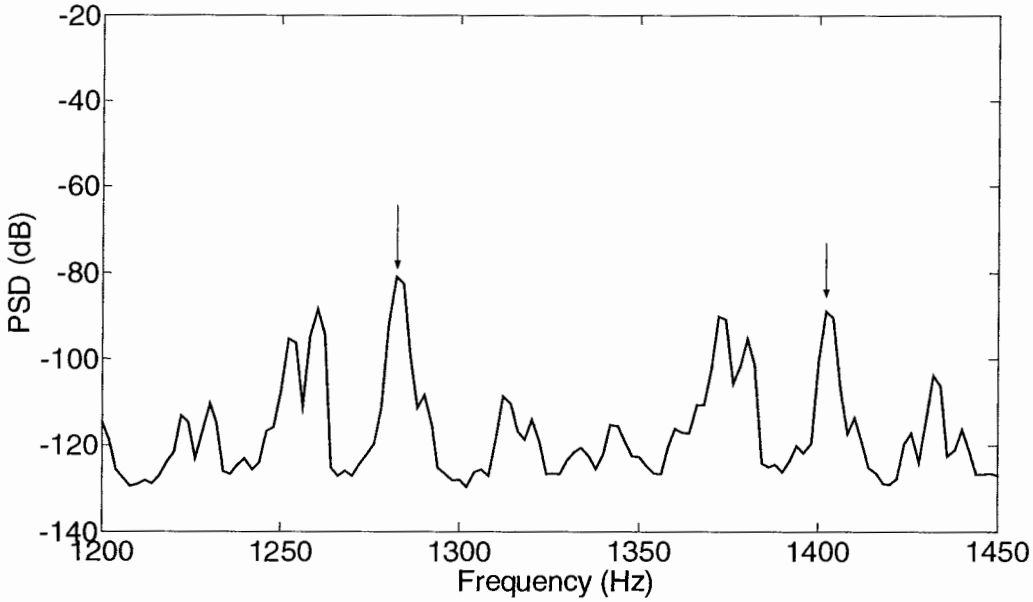

(b)

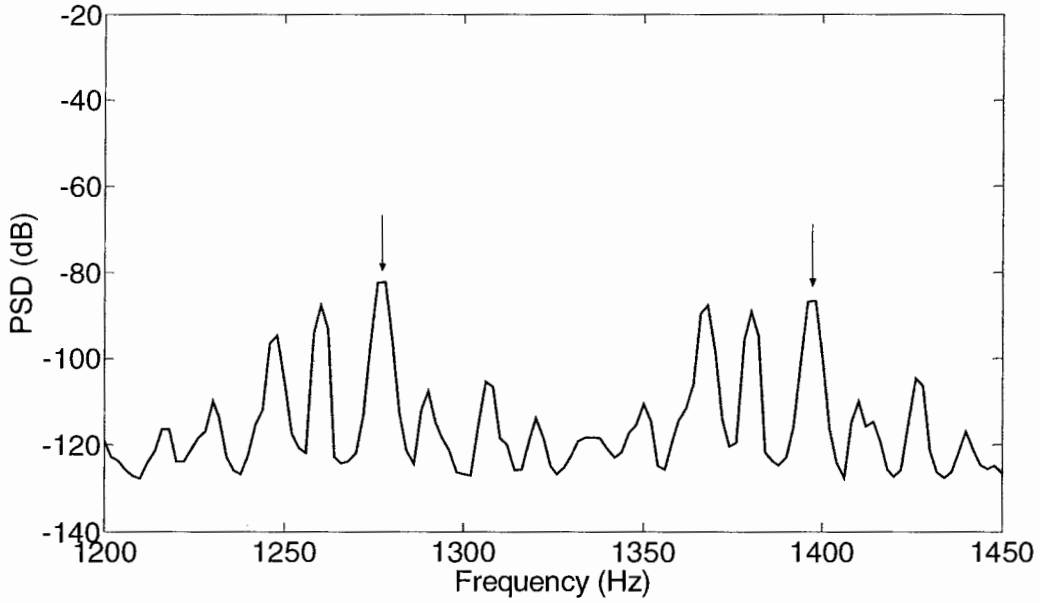

(c)

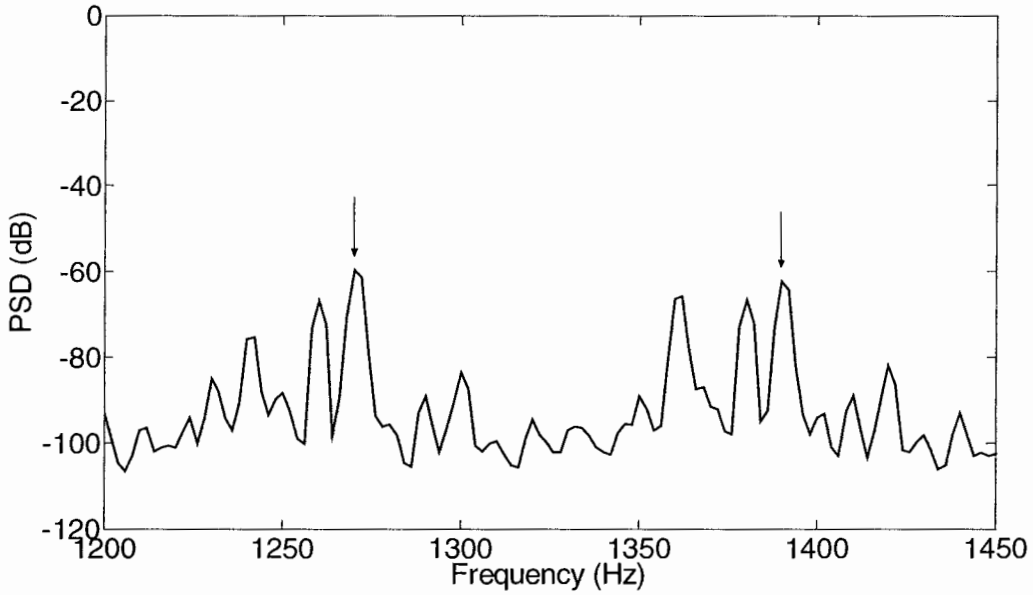

(d)

Figure D1 Experimental, normalized spectra of line current for healthy case under (a) no load, (b) 25% load, (c) 50% load, (d) 75% load

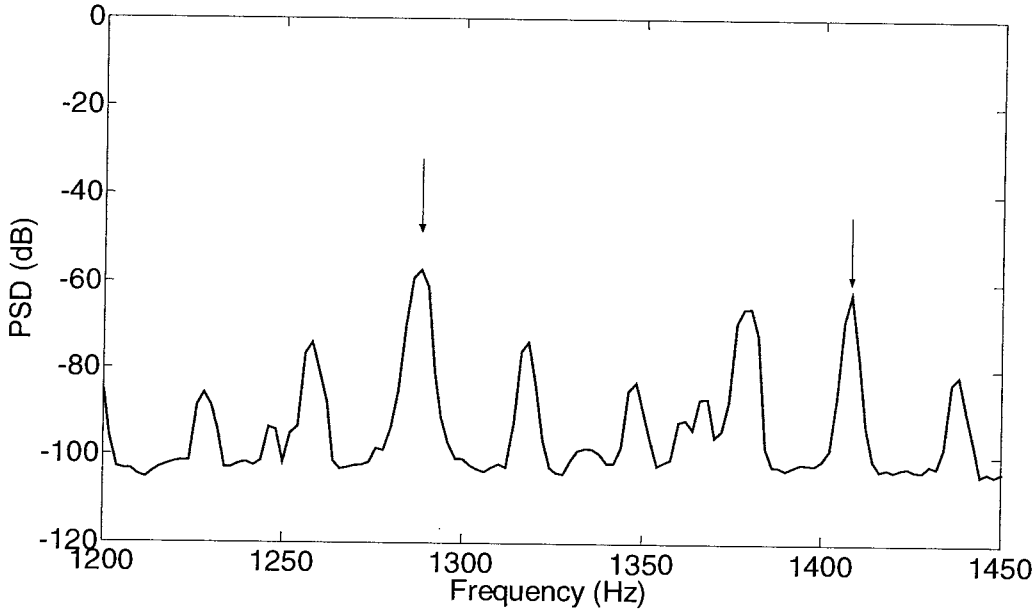
0
-20
-40
-60
-80
-100
-120
PSD (dB)
1200
1250
1300
1350
1400
1450
Frequency (Hz)

(a)

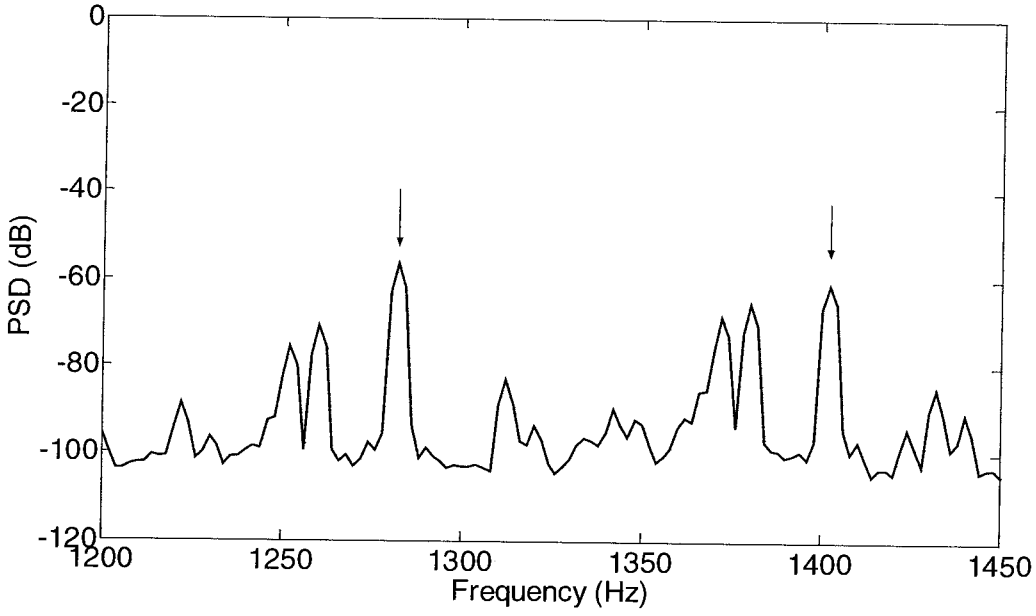
0
-20
-40
-60
-80
-100
-120
PSD (dB)
1200
1250
1300
1350
1400
1450
Frequency (Hz)

(b)

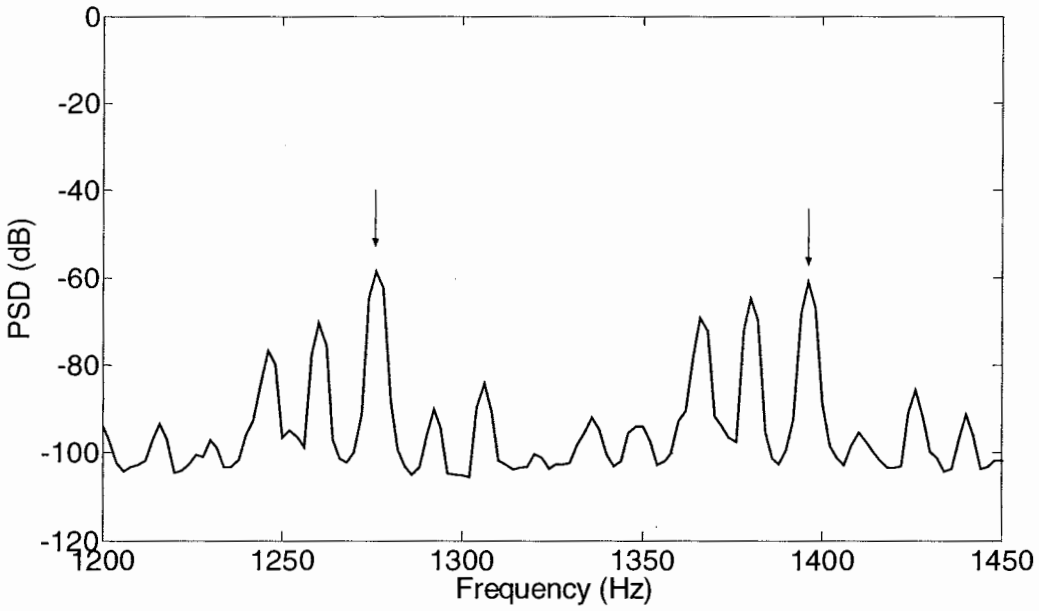

(c)

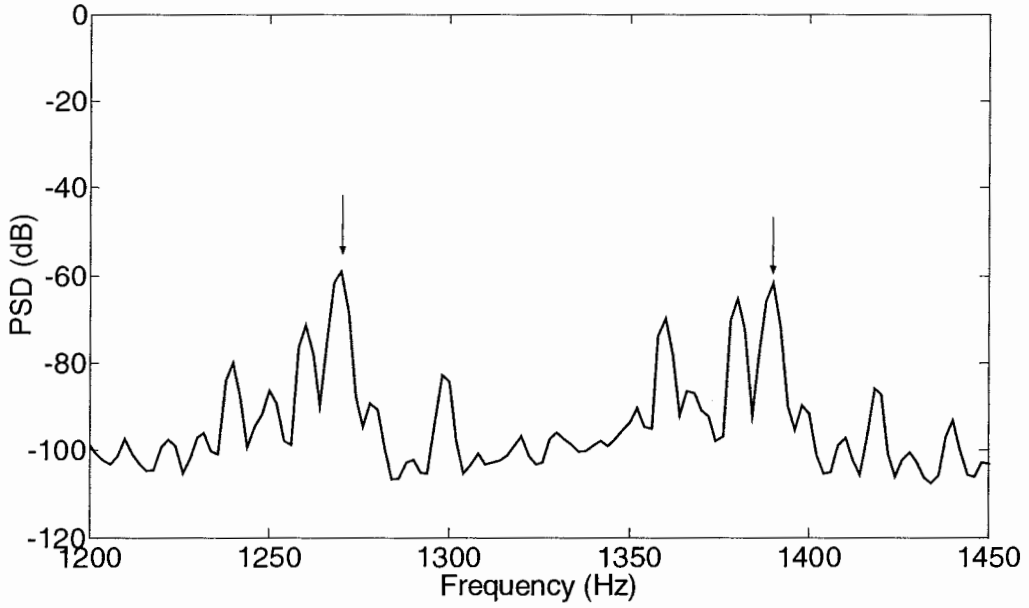

(d)

Figure D2 Experimental, normalized spectra of line current with inclined rotor (one end 50% SE, the other end –50% SE) under (a) no load, (b) 25% load, (c) 50% load, (d) 75% load

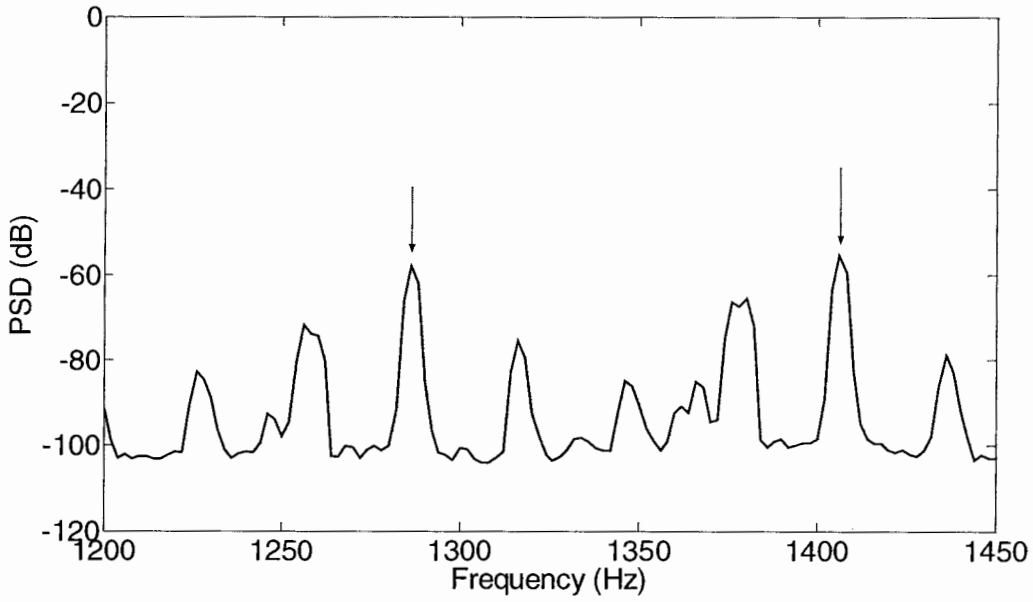
0
-20
-40
-60
-80
-100
-120
PSD (dB)
1200
1250
1300
1350
1400
1450
Frequency (Hz)

(a)

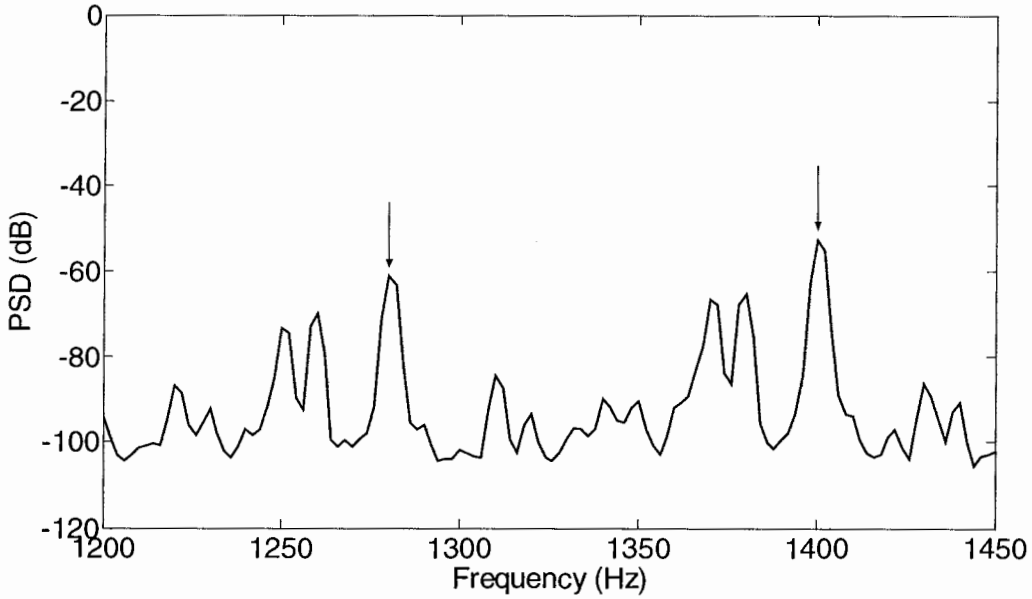
0
-20
-40
-60
-80
-100
-120
PSD (dB)
1200
1250
1300
1350
1400
1450
Frequency (Hz)

(b)

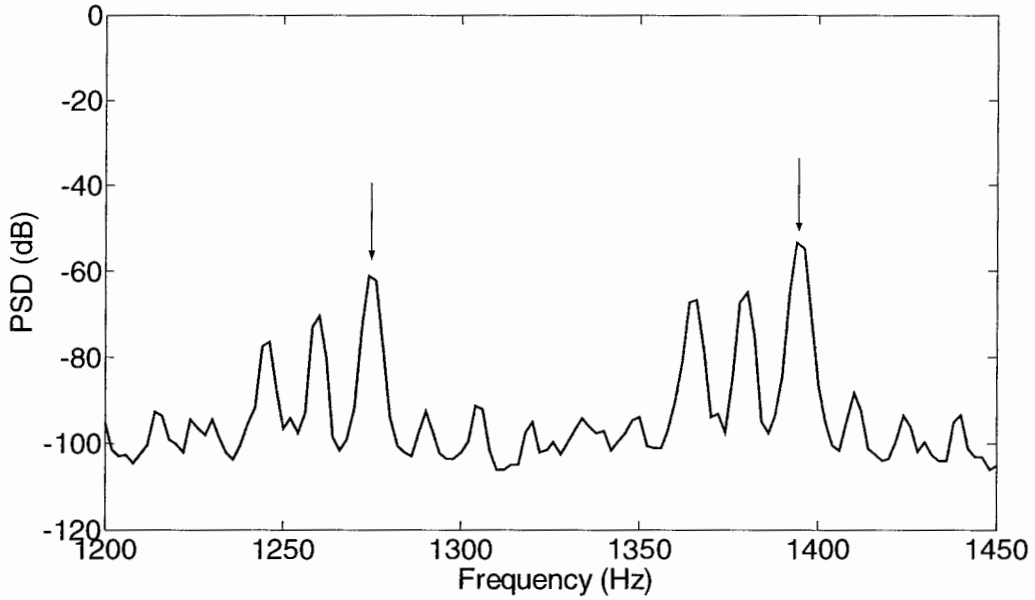

(c)

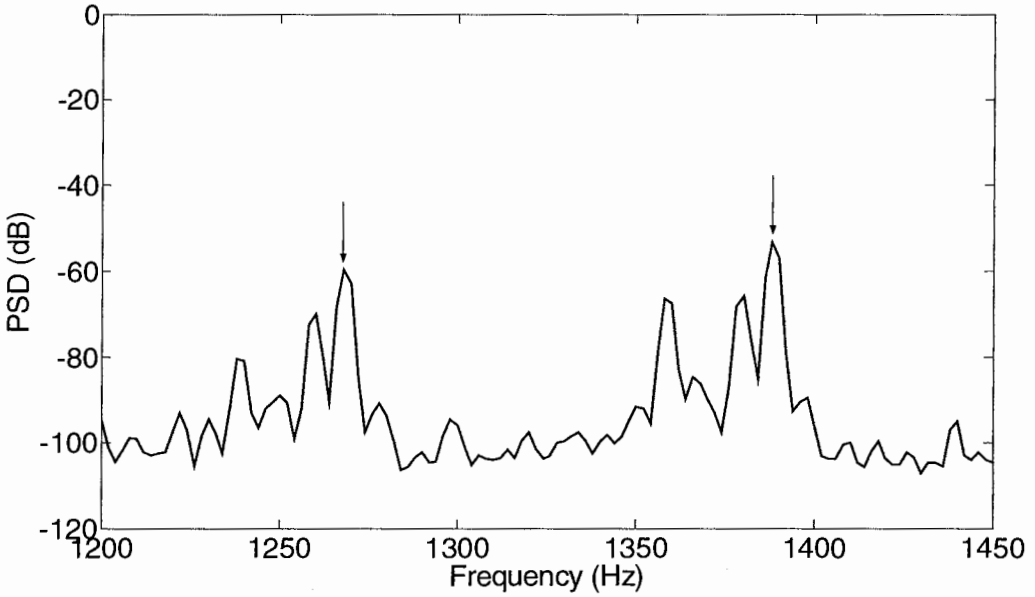

(d)

Figure D3 Experimental, normalized spectra of line current with inclined rotor (one end 22.89% SE, the other end 32.53% SE) under (a) no load, (b) 25% load, (c) 50% load, (d) 75% load

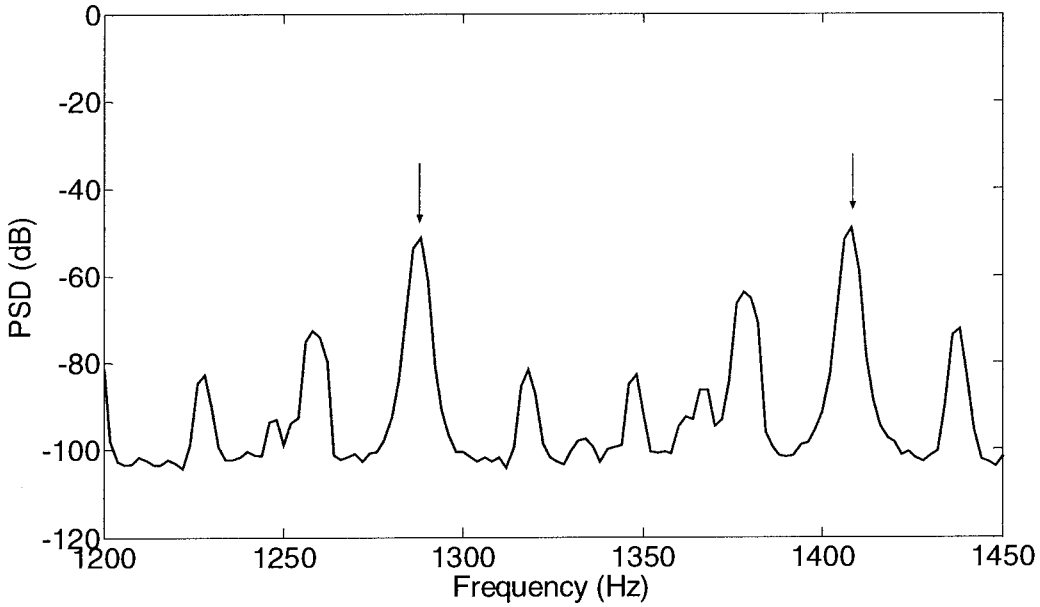
0
-20
-40
-60
-80
-100
-120
PSD (dB)
1200
1250
1300
1350
1400
1450
Frequency (Hz)

(a)

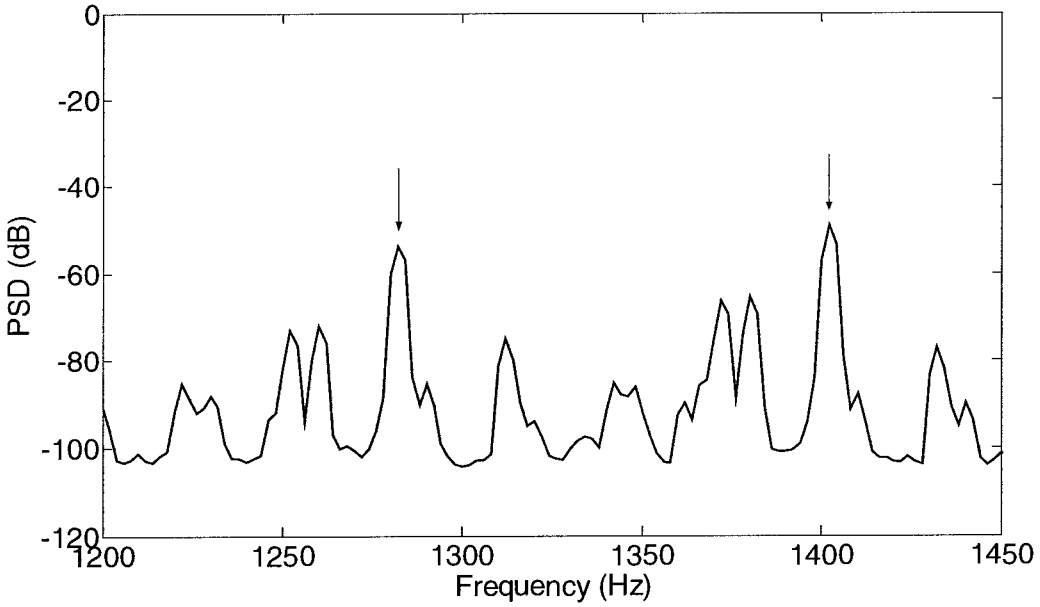
0
-20
-40
-60
-80
-100
-120
PSD (dB)
1200
1250
1300
1350
1400
1450
Frequency (Hz)

(b)

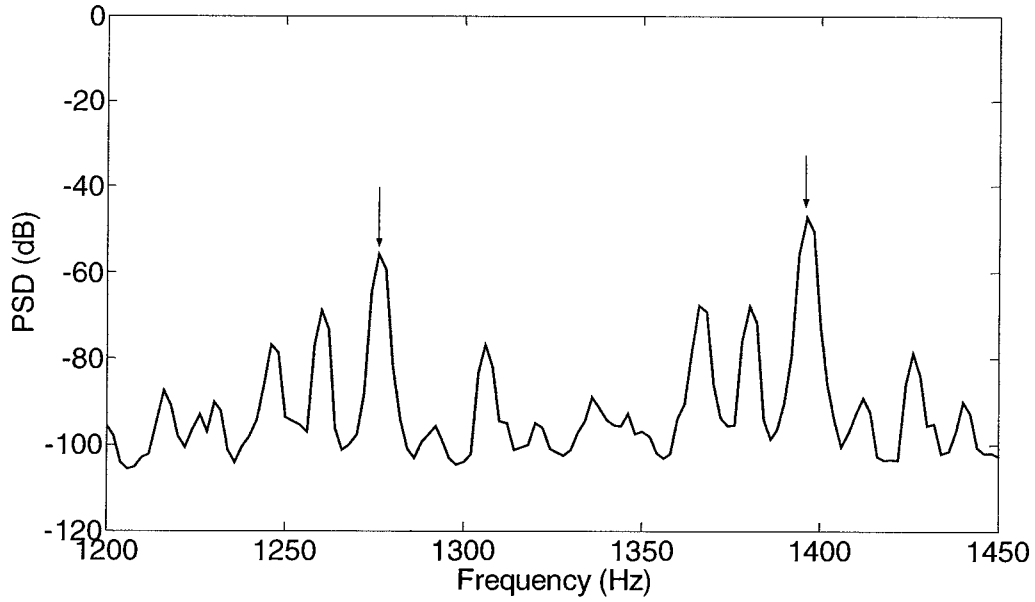

(c)

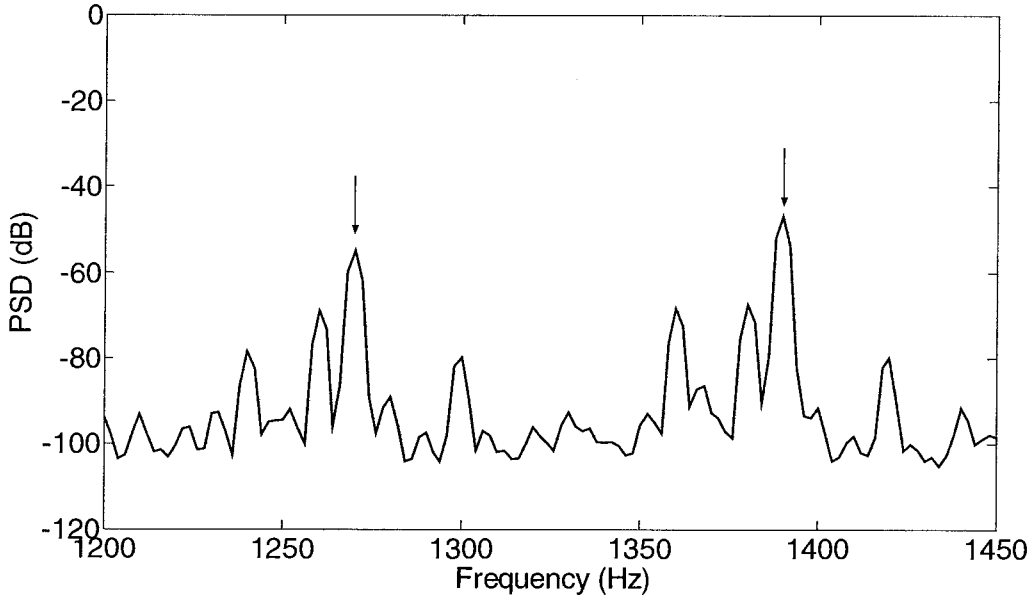

(d)

Figure D4 Experimental, normalized spectra of line current with uniform 50% SE under (a) no load, (b) 25% load, (c) 50% load, (d) 75% load

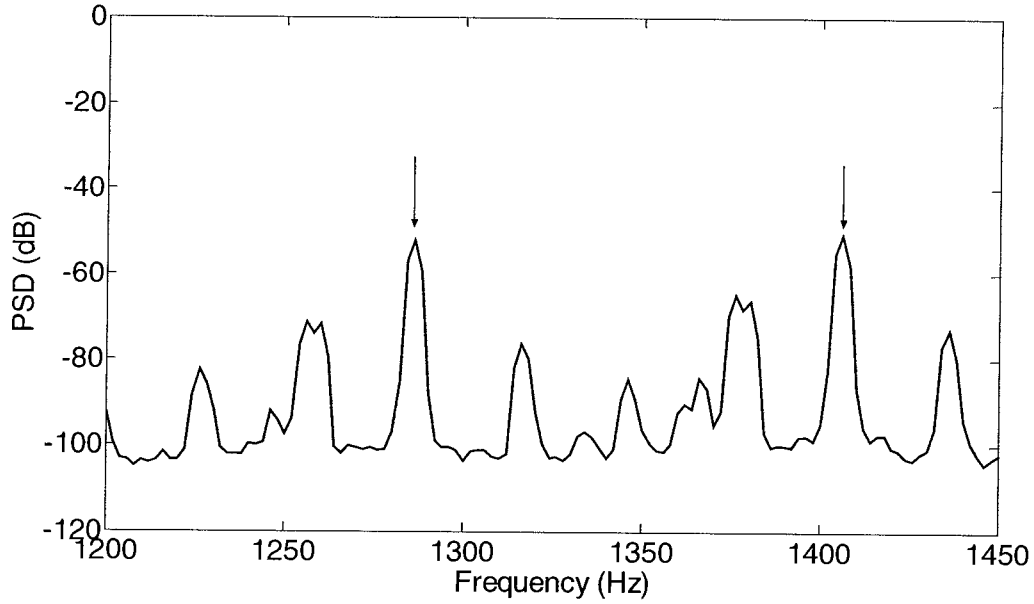
0
-20
-40
-60
-80
-100
-120
PSD (dB)
1200
1250
1300
1350
1400
1450
Frequency (Hz)

(a)

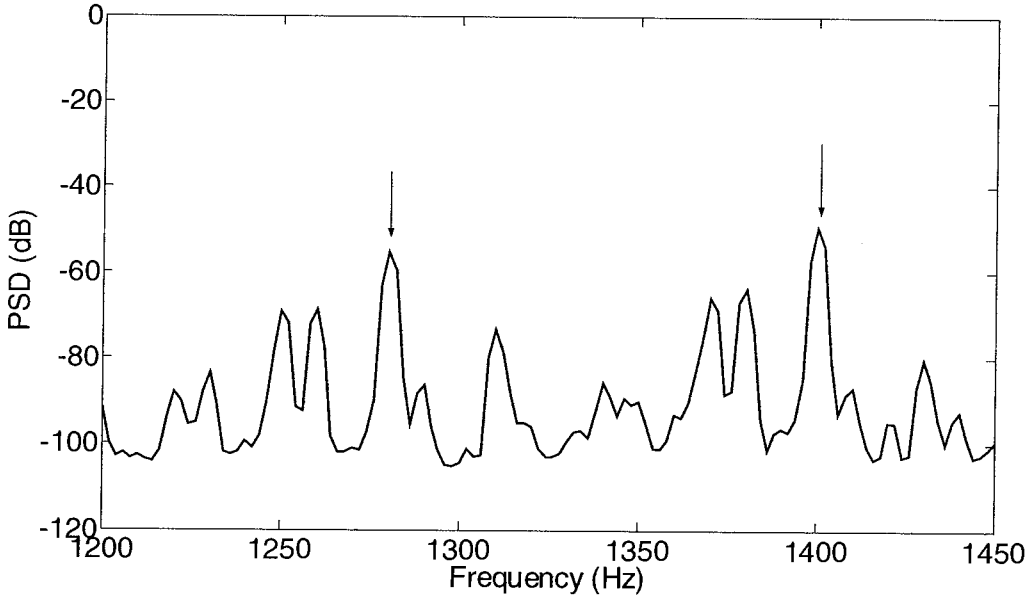
0
-20
-40
-60
-80
-100
-120
PSD (dB)
1200
1250
1300
1350
1400
1450
Frequency (Hz)

(b)

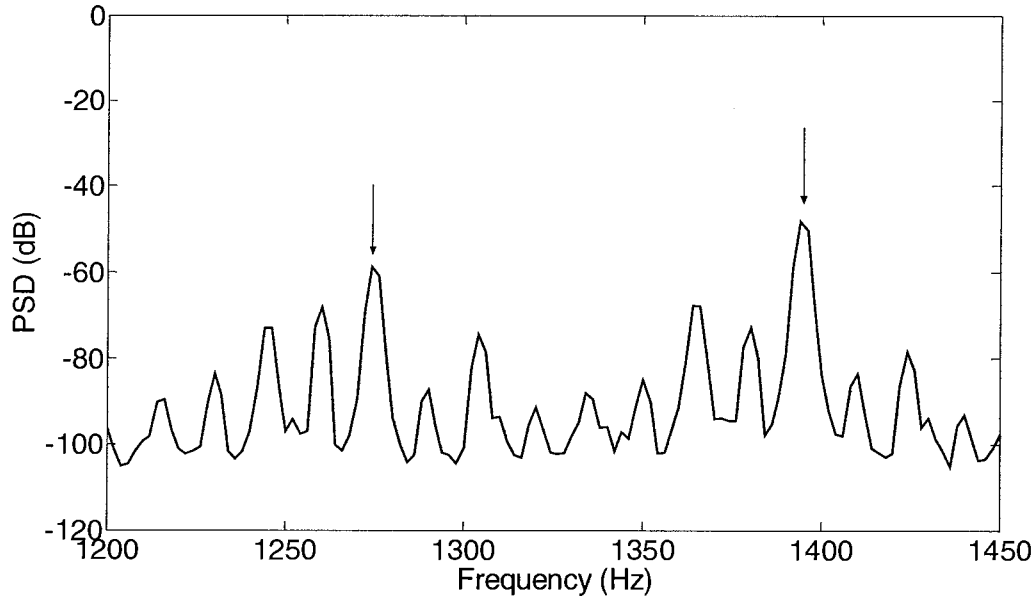

(c)

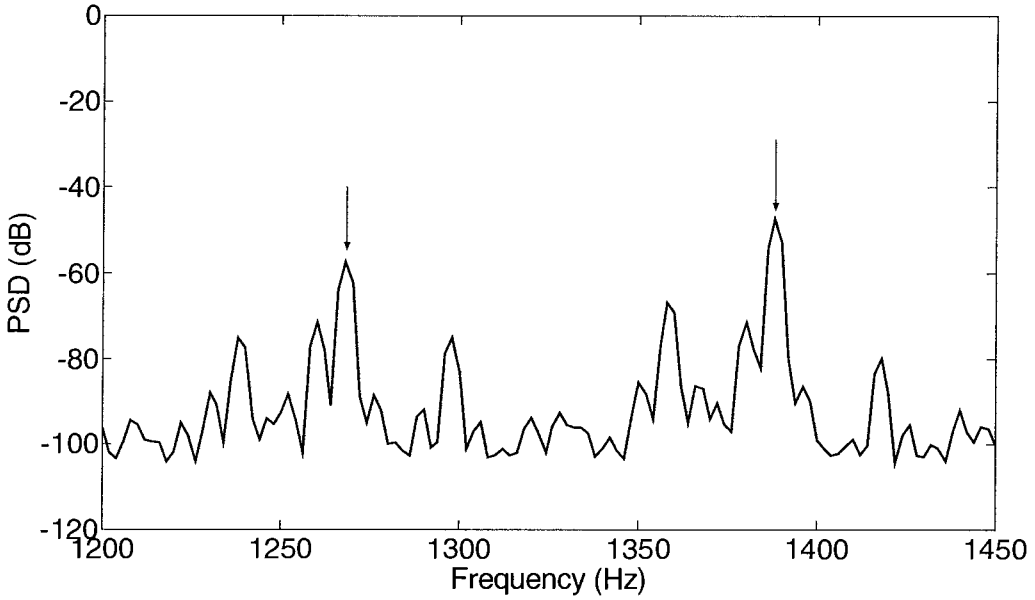

(d)

Figure D5 Experimental, normalized spectra of line current with inclined rotor (one end 45.78% SE, the other end 65.06% SE) under (a) no load, (b) 25% load, (c) 50% load, (d) 75% load